INVESTIGATIONS OF LASER-BASED REPULSIVE AXONAL GUIDANCE AND OTHER NOVEL BIOPHYSICAL APPLICATIONS OF LASER MICROBEAMS

by

BRYAN JAMES BLACK

Presented to the Faculty of the Graduate School of

The University of Texas at Arlington in Partial Fulfillment

of the Requirements

for the Degree of

DOCTOR OF PHILOSOPHY

THE UNIVERSITY OF TEXAS AT ARLINGTON

May 2014

Acknowledgements

First, I need to thank my research advisor, Dr. Samarendra Mohanty, for the scientific ideals and confidence he has instilled in me, as well as the opportunities he has afforded me. When I joined the biophysics and physiology lab at UTA, I had absolutely no prior research experience and zero expertise. In spite of that, he showed interest in my development and ultimately entrusted me with projects and responsibilities that I have not deserved. His passion and optimism for our group's research constantly astound me, and his example will always serve as my standard.

I would like to thank Dr. Ling Gu and Christopher Cote for their assistance in cell culture, as well as their advice and insight concerning all things 'biology.' I owe additional thanks to Chris Cote for dragging me to the gym occasionally and being that excited about a 'Dumb and Dumber' sequel.

I would like to thank Kamal Dhakal for his philosophical support, his MATLAB prowess, his patience, his good humor, and his friendship. In order to retain your sanity, it's necessary that someone else knows exactly what you are going through.

Many thanks to the other members of the biophysics and physiology lab at UTA for their ongoing encouragement, support and

input. Specifically, I need to thank Simon Ordonez for his assistance in cell culture and goldfish retinal explant extraction.

I would like to thank Dr. Alex Weiss, Dr. Young-Tae Kim, Dr. Mario Romero, and Dr. Ali Koymen for agreeing to serve on my thesis defense committee, and for their invaluable input.

Thanks to all our collaborators (there are too many to mention), with special thanks to Dr. Subhra Mandal, Dr. Young-Tae Kim, Samik, Dr. Ankur Jain, Vivek, Dr. Allen Bowling, and Mahdi. Without your expertise and dedication, this research would not have been possible.

My family has been instrumental in my education (and my life, general). They have encouraged me, in word and example, to never stop learning. They have lived their lives with a dignity, intelligence, and fortitude that I will always aspire to. Thank you.

Finally, I would like to thank my wife, Erica Hutchins Black, who has sacrificed more for the sake of my education than anyone else. She has tolerated more than I would ever consciously ask of her. She has given more than I could ever return. So this thesis belongs to her, as well as any subsequent degrees, diplomas, awards, certifications, commendations, pay, and/or atta-boys that I should receive between now and the time that I leave this earth. My written and verbal thanks will always seem grossly

insufficient, so I thank her by writing this thesis; by finishing what I set out to do, and by doing it as well as I know how. Again and again, thank you.

April 21, 2014

Abstract

INVESTIGATIONS OF LASER-BASED REPULSIVE AXONAL GUIDANCE AND OTHER NOVEL BIOPHYSICAL APPLICATIONS OF LASER MICROBEAMS

Bryan James Black, PhD

The University of Texas at Arlington, 2014

Supervising Professor: Samarendra Mohanty

Over the past 30 years, the properties of light have been increasingly exploited to probe and manipulate biological samples. The subsequent techniques and technologies, combined with the broadening optical characterization of biological samples (from cells to single molecules), have had a revolutionary impact on the fields of biophysics, bioengineering, chemistry, and molecular biology. Light is now known to be capable of manipulating biological samples with high spatial and temporal precision, and minimal invasiveness. Herein, we offer the findings of several novel, light-based studies as well as novel applications which exploit a laser microbeam as either a potential gradient, a cutting tool, or a temperature gradient.

Chapter 1 is divided into two main sections. One will describe the fiber-optic spanner, a novel optical tool which enables the rotation of whole cells as well as micromotors using light emitting from two counter-propagating single-mode optical fibers with a transverse offset between them. Detailed simulations of the optimal fiber orientation (separation, transverse offset, etc.) as well as stability analysis are provided. The second section will offer experimental confirmation of a newly-developed multi-scale analysis model for dynamical motion of a microsphere entering an optical trap.

Chapter 2 will describe two applications of light as a cutting tool. By creating a transient hole on the surface of a cellular membrane, we have successfully introduced rhodamine phalloidin into primary rat cortical neurons. Second, we demonstrate femtosecond laser-mediated axotomy in order to study the extent of degeneration and regeneration pathfinding ability of goldfish retinal ganglion cell axons in the presence and absence of estrogen. A subsequent study reveals that various degrees of initial injury caused by laser axotomy may heavily influence the regeneration pathfinding ability.

Chapter 3 will demonstrate the novel application of a weakly focused laser micro-beam as a repulsive guidance cue for primary central nervous system axons (both retinal ganglion cell as well as rat cortical

axons). Since this method does not require that the light impinge directly upon the axon (or growth cone), we hypothesize that the powerful, at-a-distance effect is due the temperature field (or gradient) produced by absorption of light by the environment. A detailed investigation of the temperature field hypothesis is carried out and our findings heavily implicate temperature effects as the primary repulsive guidance mechanism.

This text and figures included in this thesis draw heavily from published works (1-5) as well as my Master's thesis (*Applications of Laser Microbeam in the Study of Degeneration, Regeneration, and Guidance of Primary CNS Axons*, not currently published), which I (Bryan Black) am primary or secondary author, and principle experimental contributor. Special care is taken to reference the contributions of other authors. As the publication of our theses is required as a matter of school policy, I make it now known that no perceived duplicate or redundant claim to my contributions in any field is intended.

Table of Contents

List of Illustrations

Chapter 1

Light as a Potential Gradient

Optical Tweezers

Over the past 25 years, laser microbeams have been employed to optically trap, stretch, analyze, and surgically dissect microscopic biological samples, ranging from whole cells to intracellular structures. In order to probe the biological sample without damage, the laser irradiation wavelength should be different from the sample's maximum absorption (6). While biological macromolecules are known to strongly absorb wavelengths in the ultraviolet (200-400nm) regime, severely limiting the possible usage of UV wavelengths in deep tissue studies, they are (semi-) transparent to near-infrared (NIR) wavelengths (~800nm). This has given rise to a generally accepted wavelength band (~700 – 100 nm) in the near infrared (NIR) for the safe probing and manipulation of biological samples. However, if the laser microbeam is of a sufficient intensity (high power and/or tightly focused), biological material may be laser-pulse ablated (a process that will be discussed in detail later on in Chapter 0) using NIR light.

When an optical beam is incident on an interface, the beam is deflected from its original path either due to reflection or refraction (or both). In this context, an interface is any environmental refractive index

change. This deflection represents changes in the momenta of single photons travelling along the path of the beam, and these momentum changes give rise to optical forces, acting on the deflecting object. These optical forces can be generally classified into two types, the scattering force and the gradient force (7) (illustrated below).

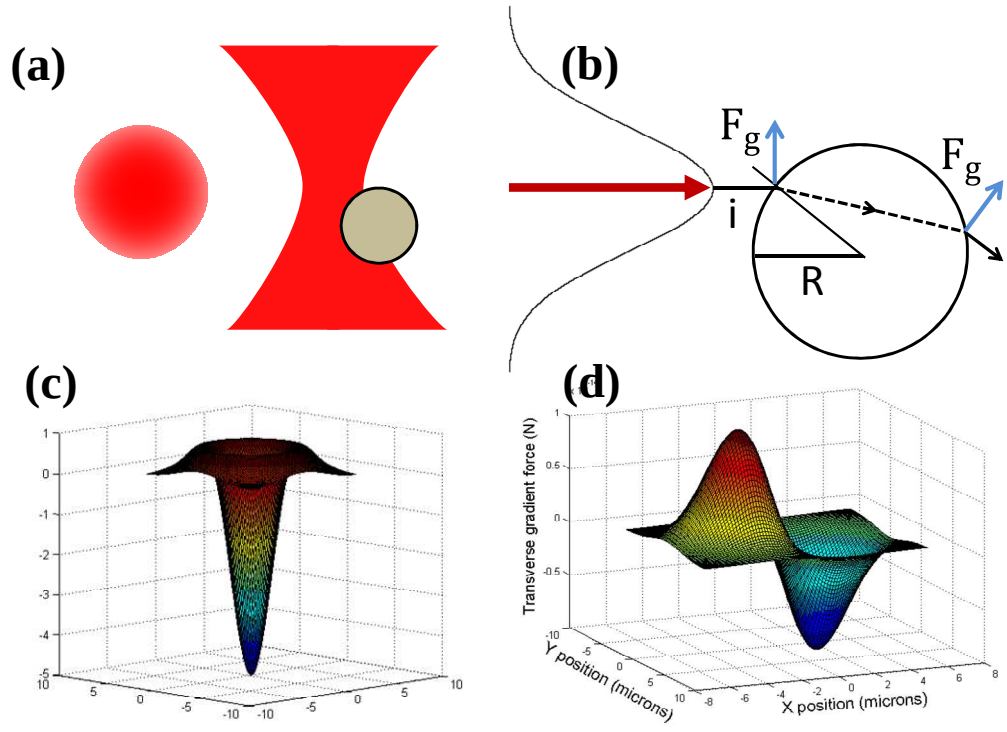

Figure 1:2 (a) Illustration of a Gaussian beam intensity cross section and (b) side view of dielectric sphere being drawn towards a focused Gaussian laser beam waist. Characteristic (not to scale) simulation of (c) axial and (d) transverse gradient force magnitudes in the Rayleigh regime.

The scattering force is mostly a result of primary reflection at the interface, but is also due to higher-order scattering and absorption of incident photons. The scattering force (on the object) is always acting along the direction of the propagating beam. In the case of a focused beam, gradient forces act along both the transverse and axial directions of the laser beam, and it constantly pulls the object towards the position of highest intensity, which is tantamount to an optical equilibrium position. Therefore, any displacement from this position will result in a restoring force, just like a spring, but in three dimensions. There is a general size limitation to the types of objects which can be effectively ‘trapped’ in this optical equilibrium position since the optical gradient force is typically on the order of piconewtons. It is important to note that, even without the conditions met in the case of stable three-dimensional optical trapping (i.e. tightly focused laser spot), similarly-scaled optical forces can be applied by any (less focused or divergent) laser microbeam.

A particle which is much smaller in size than the incident laser wavelength can be addressed in the Rayleigh regime. This size of particle can be treated as a point electric dipole, which is induced by the external optical (electric) field (8, 9). As with larger particles which classically reflect and refract incident photons, the electric dipole approximation gives rise to both a scattering and a gradient force. The scattering force is due to the

absorption and re-radiation of the optical field by the dipole. The gradient forces are due to the inhomogeneous electric field, and are directed along the field gradient. These gradient forces are also proportional the polarizability of the dielectric object, which will be exploited later in Chapter 3 for discussing one possible mechanism of laser-induced axonal guidance. It is also important to note that, while the dipole momentum is in fact oscillating in magnitude and direction, the induced dipole momentum remains harmonic with respect to the external optical field. Therefore, the time-averaged gradient force is a non-zero value (10).

The Fiber Optic Spanner

Introduction to Optical Spanners

Light-induced rotational actuation and manipulation has offered a new degree of noncontact control for actuating microscopic objects and has important applications ranging from nanobiotechnology to light-driven micromachines (11, 12), tomographic analysis, and microfluidics (13, 14). It is especially useful due to its non-contact and re-configurable nature. For more than two decades, torque on microscopic objects has been generated by transfer of linear and angular momentum from incident light focused by high numerical aperture microscope objectives (MOs). During application of torque, different variants of optical tweezers (15) can successfully lock the center of the object being rotated. While specially

fabricated (16) and asymmetric biological structures (17) have been shown to rotate in conventional optical tweezers, rotation of arbitrarily shaped objects is being achieved either by the active (mechanical) rotation of an astigmatic beam profile (18) or by passive rotation, induced by the transfer of spin or orbital angular momentum from an elliptically polarized or LG beam (19-21). Although these microscope objective-based laser tweezers systems have been used to rotate microscopic samples, they are mostly limited to rotation about the sample's optical axis, with the exception of multiple dynamically modulated optical tweezers (22). Furthermore, the relatively long working distances of the high-NA MOs required for achieving single beam trapping and rotation has severely limited in-depth manipulation and integration of these technologies onto lab-on-a-chip devices.

For overcoming the challenges of depth limitation, methods have been developed utilizing two counterpropagating beams from pre-aligned optical fibers (23). Such methods achieve transverse trapping by refraction-induced gradient forces and axial trapping by balanced, oppositely oriented scattering forces. Furthermore, the use of microfabricated fiber tips has enabled single-beam fiber-optic tweezers for trapping (24). However, to date, successful rotation of fiber-optically trapped particles has been very limited. One existing fiber-optic method

utilizes active mechanical rotation (25) of one fiber arm about the optic axis in order to rotate the trapped microscopic object. This method is limited to specific axes of rotation and has serious drawbacks, such as the requirement of precise mechanical actuation. Another existing fiber-optic rotation technique (26) requires the trapped object to be intrinsically birefringent (optically anisotropic). Fiber-optical manipulation beams have also been simultaneously used for fluorescence excitation (29) and Raman (30) spectroscopy of objects in suspension.

The Principles Behind the Fiber-optic Spanner

We have introduced a general tool, hereafter referred to as the "fiber-optic spanner," for the controlled rotation of microscopic objects.

The fiber-optic spanner is realized by introducing a transverse offset between two counter-propagating divergent beams, emitted from single-mode optical fibers. Figure 1-1 depicts the principle of the fiber-optic spanner comprised of transversely offset fibers as explained in the ray-optics regime. Primary reflection from the object results in scattering forces, which are balanced from either side at equal optical powers. However, when the scattering forces are applied at different positions in the transverse plane, the scattering forces also generate torque about the object's optically-locked center, actuating rotation of the object and also micro-fluidic flow in the vicinity of the object. The gradient forces

necessary to lock the center of the object in the transverse plane are due to the light refraction at the object-medium interface. The application of torque is dependent on (in magnitude), but not limited by, the sample's structural and optical properties. The magnitude of the applied torque also depends on the transverse offset between the two fibers and the axial separation between the two fiber arms. The object can ideally be held stationary if there is zero offset between the fiber arms. The axis of rotation can be selected with appropriate direction of offset, meaning that mechanical modulation of the transverse offset could lead to reversal in rotational direction. Furthermore, by applying unbalanced laser powers in each arm, it is possible to simultaneously translate and rotate the object. The fiber optic spanner does not rely on active mechanical movement and thus overcomes previous restrictions of methods relying on orientations of the fiber's optical axis. The fiber-optic spanner has a large working depth (imaging is limited by the viewing MO) as compared to MO-based rotation techniques, and can more-easily be integrated into lab-on-a-chip devices.

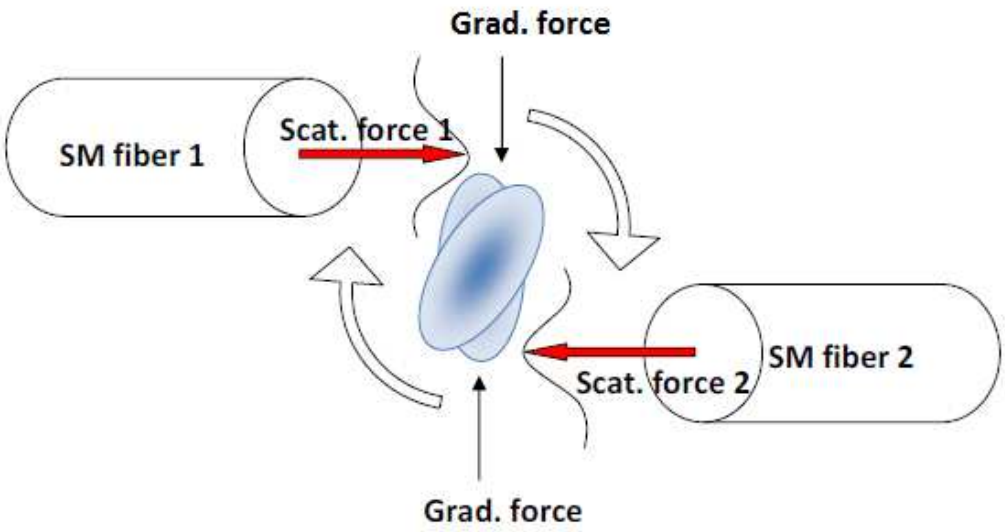

Figure 1-1 (a) Principle of fiber-optic spanner comprised of transversely-offset single-mode fibers. [Figure adapted from (2)]

Fiber-optic Spanner: Rotation and Translation of Smooth Muscle Cell

Materials and Methods:

Polydimethylsiloxane (PDMS) cross channels were constructed as follows: Sylgard 184 silicone elastomer base and Sylgard 184 silicone elastomer curing agent (Dow Corning) were mixed in a 10:1 ratio. A single glass microtube (inner core diameter 50 μm, outer diameter 200 μm) was affixed to a microscope cover slide. Two single mode optical fibers, stripped of their jackets and outer cladding were carefully laid on microscope cover slides while viewed at 3x magnification. The fibers were oriented perpendicularly to the microtube, with the fibers sharing a

longitudinal axis, but with a small (measured to be 12μm) transverse offset between them. The fibers were affixed to the microscope covers slide with tape and then checked under microscope for realignment. PDMS was carefully poured over the pre-aligned optical fibers and microtube with aluminum foil curved from the bottom of the cover slide to act as a PDMS barrier (prevent runoff). The PDMS device was then cured at ~50 ℃ for 30 minutes (or until stiff). Upon removal, optical fibers and microtubing were removed with tweezers and the device was razor-cut in such a way to reveal openings to the newly-created fiber and tubing channels channels for laser-coupled fiber and microfluidic tubing insertion. A small window at the cross section of the two perpendicular channels was also punched out with a 200 μL pipette tip for optimal viewing and removal of extraneous PDMS at the fiber-tube interface.

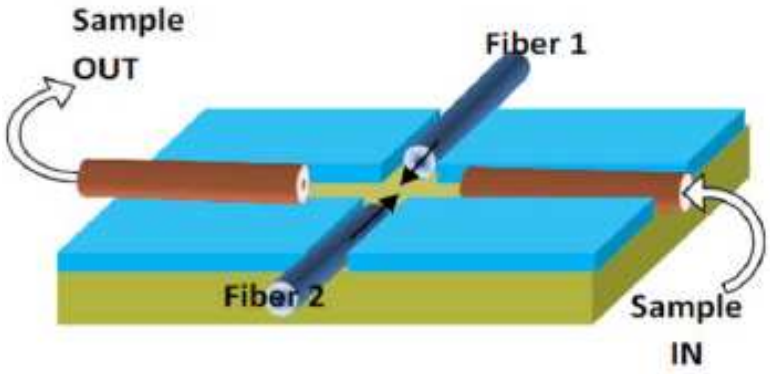

Figure 1-2 Schematic of the sample delivery and optical fiber geometry. [Figure adapted from (2)]

Two independent, laser-coupled single-mode optical fibers (core diameter = 8 μm; NA, 0.14) were used to create the fiber-optic spanner. Both fibers were cleaved on each end to ensure maximum coupling efficiency and symmetric beam emission. Fiber-1 (left) was coupled to a tunable Ti: Sapphire laser (980 nm, MaiTai HP, Newport- SpectraPhysics), which was operated in modelock-off condition to ensure a continuous wave (cw) beam. Fiber-2 (right) was coupled to a butterfly laser diode (975 nm, Thorlabs). The deliberate use of the two different laser sources enabled the control of individual fiber-arm's laser output powers and to avoid the creation of interference/standing waves in the region between the fibers. The outputs of the two coupled optical fibers were inserted into opposite ends of a 125 μm wide PDMS channel and held at a fixed separation of approximately 80 μm. A transverse offset of approximately 12 μm was introduced between the two fiber cores. The other, perpendicular PDMS indention channel (diam: 200 μm) served as the sample delivery input and output. A microfluidic pump (Harvard Apparatus) delivered the samples (smooth muscle cell or micromotor) to the central PDMS viewing window. A 40x microscope objective was used for imaging the fiber-optically manipulated objects in different orientations. Image sequences were captured by a CCD camera (Thorlabs) and processed by ImageJ software (NIH). Rotational and translational

distances were determined in a ‘hand-measured’ fashion, using ImageJ’s angle and freehand line tools.

Rotational and rotational/translational experiments were performed on live smooth muscle cells (human) (hSMC). hSMCs were chemically dissociated from culture flasks by trypsinization (0.05 %), then centrifuged. Fresh medium was replaced to quench the trypsinization reaction. Cells were mixed gently but thoroughly and collected through the microtubing via syringe. The microfluidic pump delivered the sample through the inserted microtube channel in fetal-bovine serum (FBS)-supplemented Dulbecco's Modified Eagle Medium at a flow rate of 200 µl/hr. Since the procedure was terminal, no special care was taken to decontaminate the surface of the glass, the syringe, or the microtubing. The sample-in fluid flow was not observed to disturb the fiber orientation, as the fibers only extended into the channel cross-section area by approximately 100 microns.

Once a cell was observed to be optically trapped, the external microfluidic flow was stopped. Figure 1-3 shows a fiber-optically trapped hSMC in the center of two transversely offset fibers delivering laser beam power of 20 mW in each arm. The arrows indicate the optical axes of the two fibers.

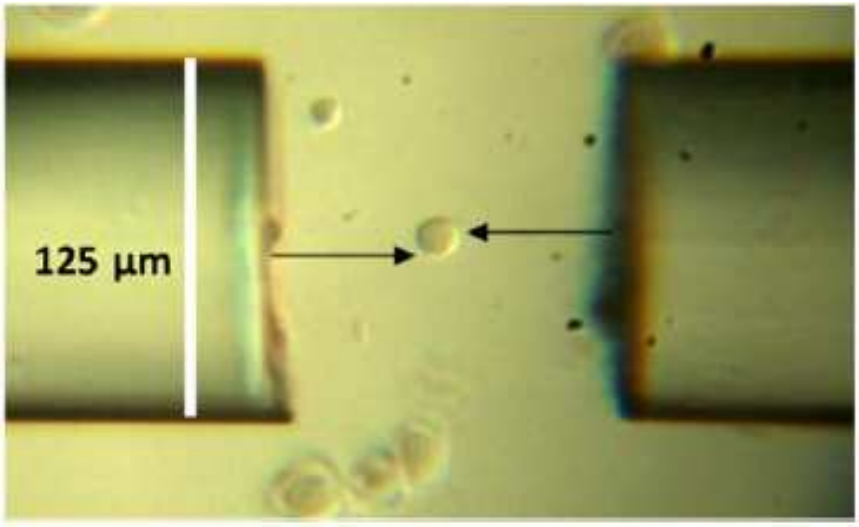

Figure 1-3 Live, dissociated hSMC, optically trapped by the fiber-optic spanner. White line indicates the width of the optical fiber (125 µm). Black arrows indicate the optical axes of the counter-propagating beams. Left fiber arm: 980 nm Ti:Sapphire laser, 20 mW. Right fiber arm: 975 nm butterfly laser diode, 20 mW. [Figure adapted from (2)]

Results

In order to demonstrate the ability of the fiber-optic spanner to rotate live biological cells for tomographic imaging applications, we fiber-optically trapped an hSMC, with transverse offset of ~12 µm between the fiber arms. Figure 1-4 (a) shows the rotation of the trapped cell at a balanced measured laser power of 12.5 mW. Figure 1-4 (a) shows the angular displacement of the cell as a function of time. The average

angular velocity of the cell, rotated using laser power of 12.5 mW, was estimated to be 0.12 ± 0.1 rad/s.

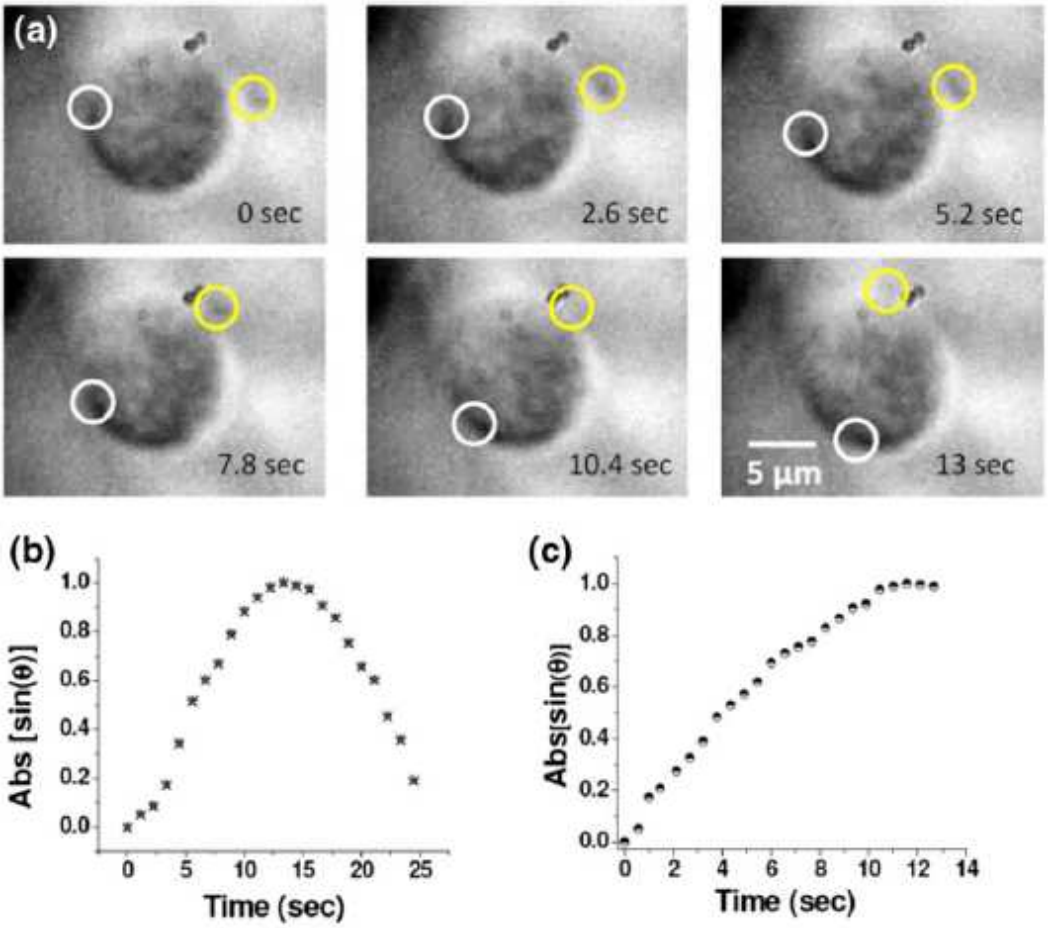

Figure 1-4 Fiber-optic rotation of hSMC. (a) Time-lapse images of fiber-optic trapping and rotation of the hSMC. (b) Angular displacement of the rotating cell as a function of time at a balanced laser power of 12.5 mW from each beam. (c) Angular displacement of the tracer particle (yellow circle) in the flow generated by the fiber-optically rotated cell as a function of time. [Figure 2 from (2)]

A tracer particle, introduced near the surface of the cell, was observed to rotate about the cell with an average angular velocity of 0.18 ± 0.1 rad⁄s due to the microfluidic flow generated by the rotating cell. In Figure 2(c), we show the angular displacement of the tracer particle as a function of time at balanced laser power of 12.5 mW.

By varying the laser power in one of the fiber-optic arms (left; 980 nm), we demonstrate that the trapped object (cell) can be translated while simultaneously rotating. Figure 1-5 (a) shows time-lapse images of simultaneous translation and rotation of fiber-optically trapped hSMC. The linear displacement of the rotating cell as a function of time is shown in Figure 1-5 (b) while the left fiber arm's laser power (980 nm) was decreased from 20 mW (0 s) to 10 mW (22 s). Figure 1-5 (c) shows angular displacement of a marked region of the cell as a function of time while the cell was being translated. In the case of simultaneous translation, the rotational speed is non-uniform (Figure 1-5 (c)) as compared to axially static rotation Figure 1-4. Figure 1-5 (e) shows a correlation histogram of linear and angular displacement of the cell during simultaneous rotation and translation. No clear correlation was observed.

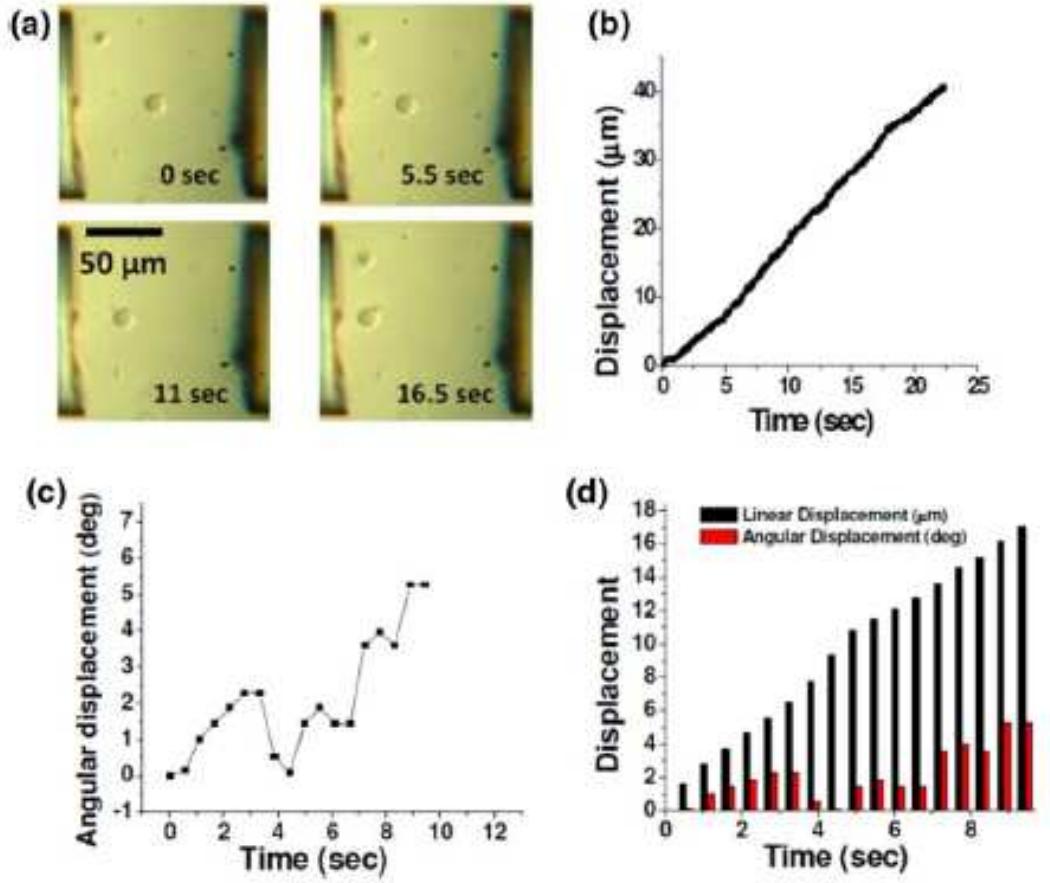

Figure 1-5 (a) Time-lapse images of simultaneous translation and rotation of fiber-optically trapped hSMC by varying the laser power of the left beam (Media 2). (b) Displacement of the rotating cell as a function of time achieved by decreasing the left arm laser power from 20 mW (0 s) to 10 mW (22 s). (c) Angular displacement of a marked region of the cell as a function of time. (d) Correlation histogram of linear and angular displacement of the cell as a function of time during simultaneous rotation and translation. [Figure 3 from (2)]

Discussion

We have successfully demonstrated a single-mode fiber-optic spanner as a powerful tool for the rotation of living human smooth muscle cells. This method of rotation does not require the cell to possess special structural or optical properties in order to actuate rotation. By varying the laser power of the two counterpropagating beams, rotational velocity of fiber-optically rotated hSMC could be controlled. We have also observed that such rotation can actuate microfluidic flow. It is important to note here that torque can be applied along any sample axis by creating the desired offset between the two fiber-optic arms of the spanner, thus allowing rotation in any direction. This technique can be extended to the biochemical analysis of cells while being tomographically imaged (27) during rotation. Since the time of our publication, this technology has been utilized by Kolb et al.(28), whose research team combined the principles of the fiber-optic spanner with pneumatically controlled fiber arms to enact rotational actuation of the sample for detailed imaging.

Fiber-optic Spanner: Rotation of Polystyrene Sphere Assembly

Materials and Methods

Methods and materials detailing the fabrication and operation of the fiber-optic spanner are found in Section Chapter 0.

Additional rotation experiments were performed on a symmetric microstructure comprised from seven adhering polystyrene microspheres (each with a radius of 3 μm), which was delivered in distilled water at a flow rate of 200 μl/h by the same mechanical fluid pump. A 20x microscope objective was used for imaging the rotating microspheres-assembly. Image sequences were captured by a CCD camera (Thorlabs) and were subsequently processed by ImageJ software (NIH). Angular and translational displacements were ‘hand-measured’ using the ImageJ angle and freehand line tools. The initial balanced laser output power was measured to be approximately 7.3 mW prior to fiber insertion, with the Ti: Sappire laser beam tuned to 980 nm. Once the microsphere assembly became optically trapped, the external microfluidic flow was stopped.

Results

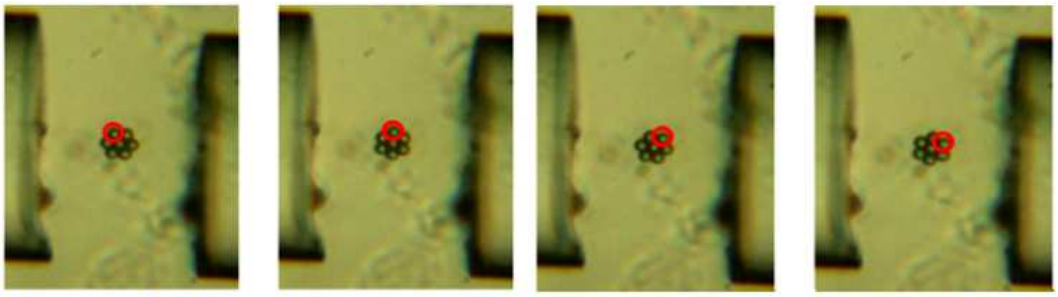

Figure 1-6 Time-lapse of microsphere assembly rotation. Red circle highlights a single microsphere in each subsequent frame.

Figure 1-6 shows time-lapse images of spanner-induced rotation of the microsphere assembly. Throughout the duration of the experiments (~20 minutes), the microsphere assembly remained trapped parallel to the cover glass surface with stability. The observed stability of the planar, disk-like structure is attributed to the transverse offset between the two beams in horizontal plane. In this geometry, the disk-like object maximizes its interaction with the two laser beams by orienting in a horizontal plane, which leads to a minimal potential energy configuration.

The microstructure could be rotated with an average velocity of 1.4 ± 0.03 rad/s at a balanced sample-site laser power of 7.3 mW. As expected, with an increase in balanced laser power, the rotational velocity could be increased. Subsequent measurements at balanced sample-site powers of 14 and 19.9 mW yielded average angular velocities of 2.7 ± 0.1 and 4.1 ± 0.13 rad/s respectively. Figure 1-7 (a) shows angular displacement of the fiber-optically rotated microstructure as a function of time at three different balanced laser powers. The fit of average angular velocities vs laser power (Figure 1-7 (b)) shows a linear-dependence. The implied threshold laser power required to initiate rotation (by overcoming viscous drag) was found to be 1.1 mW for this structure.

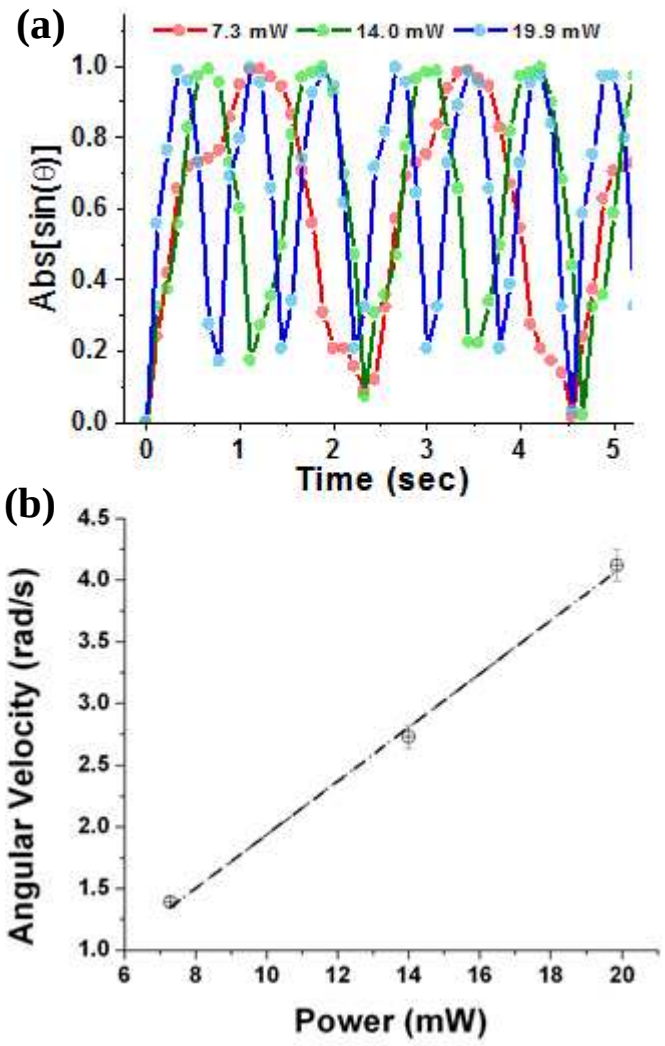

Figure 1-7 Angle variance with time and angular velocity power dependence

During the assembly's rotation, a periodic angular velocity 'lag' was observed Figure 1-7. Such lags were observed six times per rotation, regardless of laser intensity. This is attributed to the specific geometry of the seven microsphere assembly. Although the principle underlying the

fiber- optic laser spanner does not rely on the spatial properties of the sample in order to generate torque and subsequent rotation, the specific geometry of the microsphere assembly did disrupt the sample's uniform rotation. At certain orientations, the two fibers' optical axes both fall between two adjacent microspheres on either side of the assembly. At that instant, the scattering forces from the two incident beams were approximately equal and opposite. Since the resultant scattering forces would cancel one another at that instant, only the gradient forces produced a net torque, and the resultant angular velocity would naturally be reduced.

For monitoring the microfluidic flow associated with the fiber-optically driven micromotor, tracer particles were introduced in the flow, which were observed to rotate with angular velocities of 1.75 ± 0.08 and 2.17 ± 0.1 rad/s respectively, near the rotating micromotor, at sample-site laser power of 19.9 mW. Figure 1-8 (a-b) shows time-lapse images of the movement of these tracer particles (encircled). The angular displacement of two tracer particles as a function of time during micromotor rotation is shown in Figure 1-8.

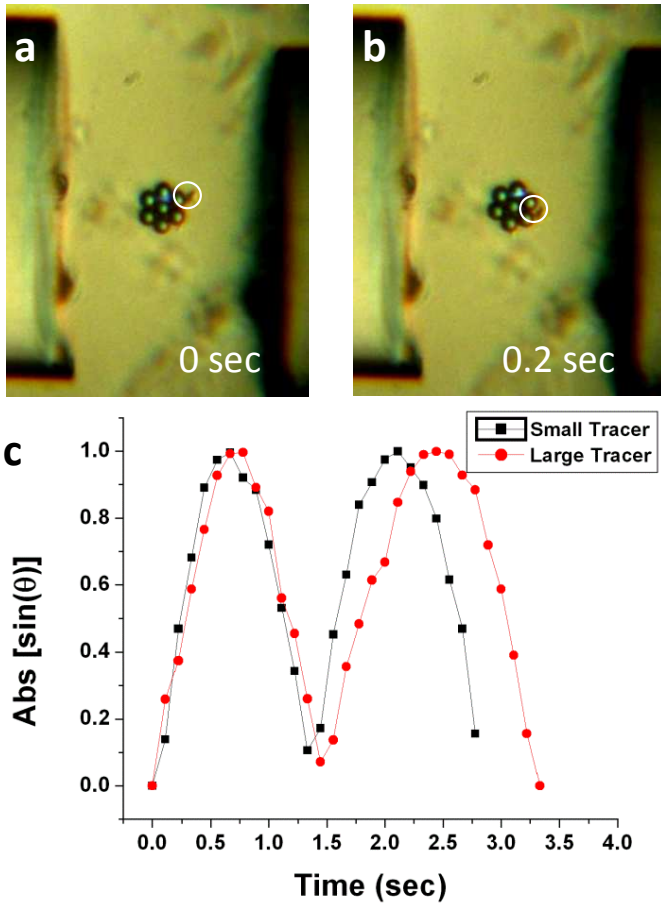

Figure 1-8 Microfluidic actuation by fiber-optic spanner. (a) and (b) Time lapse images of movement of tracer particle (due to microfluidic flow) actuated by fiber-optically rotated microsphere assembly. (c) Angular displacement of the tracer particles as a function of time during assembly rotation. [Figure 2 from (3)]

Assuming laminar, steady flow in the direction tangent to the surface of the cylinder, and neglecting gravity and other external forces, we note that the velocity (V_θ) at any point on the outside of such a cylinder

is a function of r only. V_θ can be found by solving both the associated continuity equation,

$$\frac{\partial p}{\partial t}+\frac{1}{r}\frac{\partial\left(\rho r V_r\right)}{\partial r}+\frac{1}{r}\frac{\partial\left(\rho V_\theta\right)}{\partial \theta}+\frac{\partial\left(\rho V_z\right)}{\partial z}=0 \qquad (1)$$

and Navier-Stokes equation,

$$\frac{\partial V}{\partial t}+\left(V\cdot\nabla\right)V=-\frac{1}{\rho}\nabla p-\nabla g+v\nabla^2 V \qquad (2)$$

The Navier-Stokes equation relates the summed inertial terms (left hand side) with the viscous drag terms (right hand side). The inertial term's magnitude can be generally characterized by the Reynolds number (29), Re=vL/v, where L is the primary dimension of the body, v is the mean velocity of the object relative to the media, and v is the media's kinematic viscosity. For the microfluidic flow in our experiment, L is approximately 6 µm, and v is ~µm/sec. Therefore, the Reynolds number for our flow will be much less than one and the inertial effects can be neglected. With no fluid flow in the radial direction, and since our sample delivery flow has been stopped, the pressure gradient, at any point perpendicular to rotational axis, will also be zero. The Navier-Stokes equation now reduces to Laplace's equation, which can be solved easily with appropriate boundary conditions.

Approximating our micro-motor as a thin circular cylinder, we find

$$V_\theta = \frac{1}{r}\omega_0 a^2 \quad (3)$$

Where a is the radius of the cylinder (9μm) and ω_0 is the angular velocity (4.13 ± 0.13 rad/s) of the cylinder at the fluid interface. Calculation of the large tracer particle's angular velocity yielded 2.32 rad/s. Besides the approximations made above, this difference can be attributed to several other factors, including the scattering force on the tracer particle. The speed of tracer particle(s) can increase (or decrease) depending on whether the trace particle is moving along (or against) the beam propagation direction.

The microspheres used in rotational experiments were fluorescent (green). This was not a choice of experimental design, but simply the type of microspheres available at the time. When the balanced laser powers were increased to 20 mW, the Ti:Sapphire laser began pulsing even with modelocking in the off position. The pulsing laser evoked bright blue-green flashes from certain spheres at certain time points during their rotation (Figure 1-9 (a)). Since the Ti:Sapphire laser was operating at 980 nm, this could not be direct single-photon stimulation of the microsphere fluorescence. Additionally, not all spheres were fluorescing. Only those along the central axis of the Ti:Sapphire laser arm.

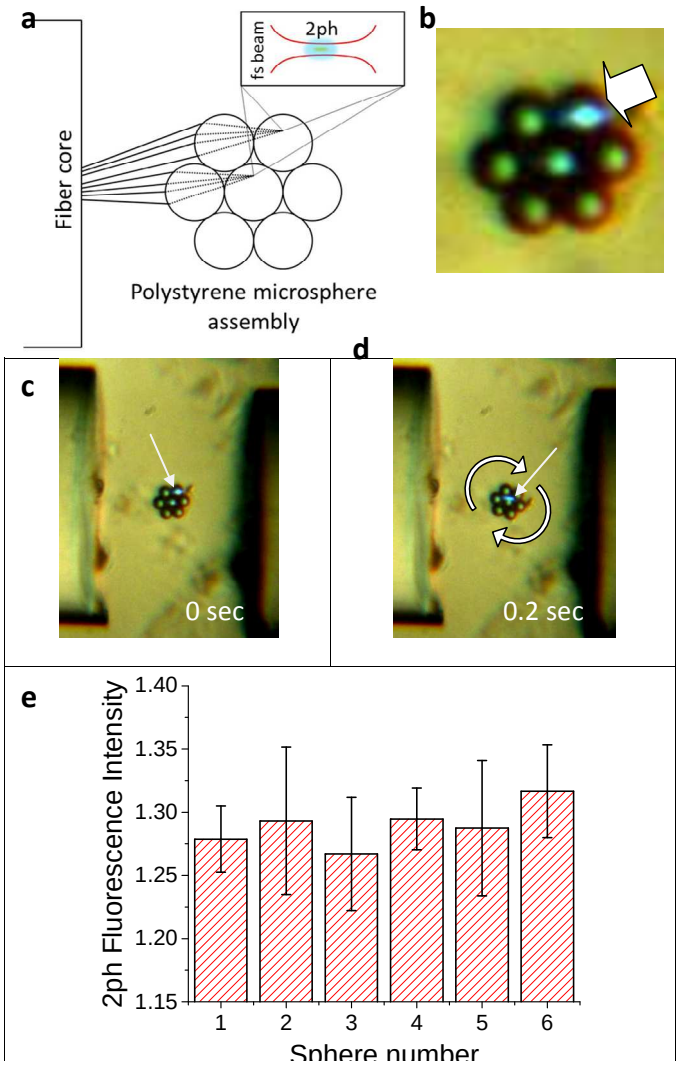

Figure 1-9 Two-photon scanning by fiber-optic spanner. (a) Schematic explaining sphere-focused 2ph excitation. (b) Arrow indicates two-photon excited fluorescence of one sphere. (c) and (d) Time-lapse images of two-photon scanning of microsphere-assembly, actuated by fiber-optical spanner. (e) Mean fluorescence intensity of individual peripheral spheres. Error bars indicate standard deviation. [Figure adapted from (3)]

The fiber arm was enabling two-photon scanning of the microsphere assembly. This was surprising, since the light source was an optical fiber (0.14 NA). However, as can be seen in Figure 1-9, two-photon fluorescence can only be seen when on sphere is directly in line with another on its left. This must mean that the polystyrene spheres are acting as lenses, focusing the incident light onto the adjacent sphere. Two-photon excitation requires a high photon density. Figure 1-9 shows the average two-photon intensity of each sphere through five rotations.

If one of the counter propagating beams was removed, the microsphere assembly would simply be pushed along the optical axis with no sustained rotation due to the unbalanced scattering forces. So in order to test the plausibility and stability of sustained rotation during translation, we tuned the power of one beam arm from 19.9 to 7.3 mW, thereby applying unbalanced scattering forces. This resulted in coupled rotational and translational motion (4.78 ± 0.18 μm/s), with no observable decrease in the uniformity or stability of the object's rotation (angular velocity of 1.66 ± 0.04 rad/s). Though this is a significantly lower angular velocity than that observed at balanced laser power, one can see that the angular velocity remains relatively constant during this translational period. This is due to the decreasing separation between the microsphere assembly and the laser arm with decreased power.

The rotational stability of the disk-like structure, while trapped by the fiber-optic spanner, was such that we could simultaneously translate and rotate the microsphere assembly while the orientation plane remained horizontal. The observed stability of the rotating microsphere-assembly, while being translated in the fiber-optic spanner-translator system, can be attributed to a maximization of interaction between the horizontally-oriented microsphere assembly and the beams emanating from the two fiber arms. The time-lapse images of the rotating assembly during translation are shown in Figure 1-10 (a). In Figure 1-10 (b), we show the helical path of one of the outer-microsphere of the assembly during simultaneous rotation and translation. Figure 1-10 (c) shows the angular displacement of the simultaneously rotating and translating microsphere-assembly as a function of time for the aforementioned case. Further reduction in power from 7.3 mW to 1.2 mW led to slower rotation (Figure 1-10 (d)). Figure 1-10 (e) shows the translational displacement of the rotating microsphere assembly as a function of difference in power between the two laser beams. The correlation of angular displacement and translational displacement in each frame is shown in Figure 1-10 (f). It is important to note here that torque can be applied along different axes (other than the optical axis) by creating the desired offset between the two

fiber optic arms of the spanner, thus allowing three-dimensional non-contact manipulation of objects.

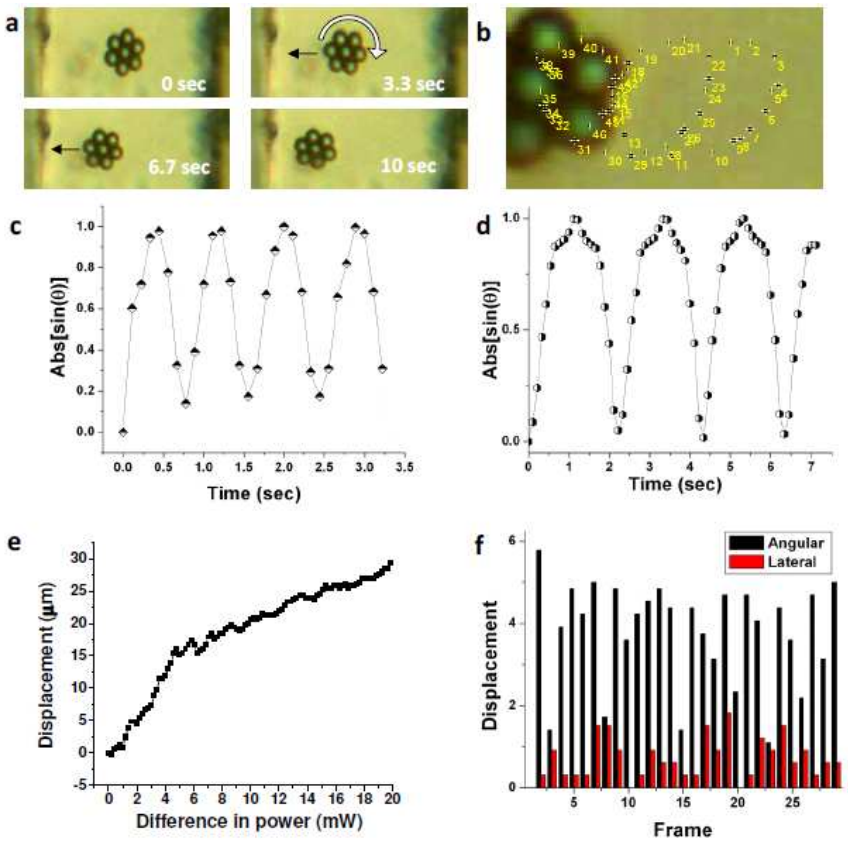

Figure 1-10 Simultaneous rotation and translation of microsphere-assembly. (a) Time-lapse images of rotational/translational motion. (b) Helical track of single microspheres. Angular displacement as a function of time for (c) 19.9 mW to 7.3 mW and (d) from 7.3mW to 1.2 mW. (e) Translational displacement as a function of the power-difference between the two laser beams powers. (f) Correlation of angular and translational displacement

Discussion

It is important to note that the technique presented here can be applied to rotate objects of different sizes. However, stabilization of the object in longitudinal direction will require different range of transverse offsets. For optimal torque generation, suitable transverse offset needs to be chosen from this range. Altering the transverse offset distance affects the efficiency of the transverse gradient trap as well as the distance at which the scattering force is applied from the center of the object, effectively changing the torque. The divergence of the beam may need to be controlled to avoid significant overlap of the two counter-propagating beams. By replacing the bare fiber tips with axicon-tipped fiber (30), the technique can be further refined.

To conclude, we have demonstrated fiber-optic rotation of a micromotor using counter-propagating beams having transverse offset. Rotational velocity of fiber-optically rotated micromotor could be predictably controlled by changing the laser power of the two counter-propagating beams. Actuation of a micro-motor by the fiber-optic spanner led to microfluidic flow proportional to its rotational velocity. Numerical simulations of the torque generated for different fiber configurations (transverse offset, and laser power) will be shown to be in good agreement with experimental values. Notably, two-photon scanning of the

microscopic object could be achieved by rotating the object using the two-photon excitation beam itself. In addition to tomographic imaging and spectroscopic applications, the fiber optic offset method can be used for complex microfluidic actuation (31, 32), which can be employed for cellular mechanotransduction (33, 34) and axonal guidance (35). Apart from miniaturization capability, optical fiber based manipulation can be used in multi-functional mode such as diagnosis and sensing of samples in a flow.

Fiber-optic Spanner: Simulations of Torque and Rotational Stability

All authors contributed to the mathematical considerations involved in the development of the following model (3). Special thanks to Dijun Luo for Matlab programming.

By considering only Newtonian motion, and the interactions between light and matter in the ray optics regime, we have developed a simple model for calculating the torque exerted by an individual fiber-optic laser beam on a single microsphere (radius: R) located at an arbitrary position with respect to the fiber end. The ray-optics diagram of interactions considered in the development of this model is shown in Figure 1-11 (a). Other, higher order reflections and refractions were neglected, along with effects of temperature increase due to medium and microsphere absorption at 980 nm.

Consider a beam centered at h, and a sphere of radius R, located at an offset H from the assembly's rotational axis. An incident ray coming from the Gaussian beam ray i, with intensity I_i in small area dA, impinges upon the surface of the sphere. Within a small time duration, dt, we assume the total number of photons travelling along ray i, is N_i.

From Newton's equations, we have

$$F \cdot dt = N_i p = N_i \left(\frac{E}{c} \right) \tag{4}$$

where E and c are the energy and speed of the photon. Let (l_i, m_i, n_i), (l_r, m_r, n_r), (l_t, m_t, n_t) be the directional cosines of the incident, reflection, and refraction rays. Then the total force in the x-direction, generated by a single ray is

$$F_i = \frac{E}{c} \frac{N_i}{dt} \left(l_i - \alpha l_r - (1-\alpha) l_t \right) \tag{5}$$

where α is the average reflection coefficient, computed using Fresnel's equations. According to the power of the laser beam,

$$\frac{E N_i}{dt} = I_i dA \tag{6}$$

Therefore,

$$F_i = \frac{I_i dA}{c} \left(l_i - \alpha l_r - (1-\alpha) l_t \right) \tag{7}$$

It is trivial to show that the total force is applied on the center of the sphere. In that case, the total torque generated by all the rays is,

$$\tau = \sum_i F_i H \quad (8)$$

By considering the symmetric orientation of the seven spheres, the forces generated by the rays in the y- and z-directions cancel. Figure 1-11 (c) shows numerical simulations of angular velocity of the microsphere-assembly as a function of laser power for different transverse offsets (h). For these simulations, the sphere radius (R), refractive index (n2/ n1) and axial offset (D) was fixed at 3 µm, 1.59/1.33 and 45 µm respectively. The simulated angular velocity Figure 1-12 was found to increase linearly as a function of laser power. Simulations of torque as a function of transverse offset (h) reveal an optimum transverse offset for differently sized microsphere assemblies (Figure 2b) at fixed laser power (20 mW) and axial offset (D = 45 µm). shows numerical simulations of torque on the microsphere-assembly as a function of transverse offset (h) for different sphere radii (R). As can be clearly seen, there exists an optimum transverse offset between the two fibers for maximal torque (at a fixed laser power). Thus, for the microstructure (Figure 1-11 (b)) having 3 µm radii spheres, maximum torque would correspond to a transverse offset of 5µm. As expected, the simulated torque is found to increase linearly as a function of laser power for a fixed sphere radius (3 µm).

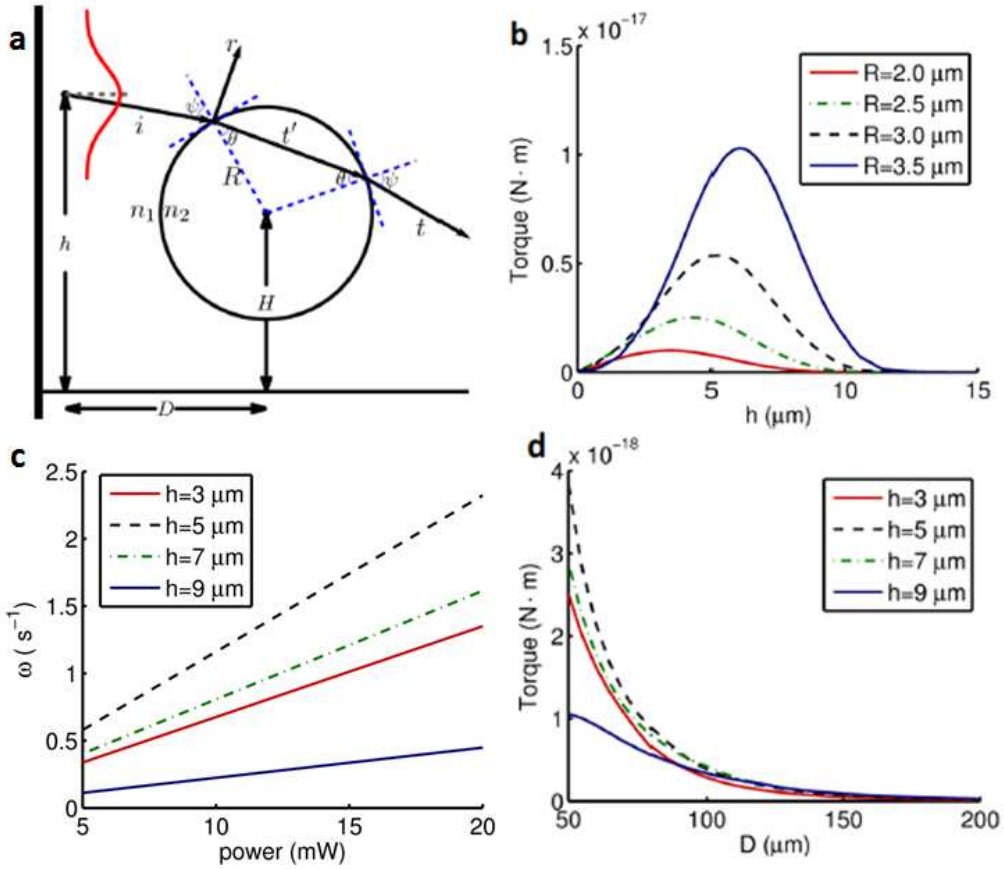

Figure 1-11 Numerical simulation of torque generated by fiber-optic spanner. (a) Ray-optics diagram showing interactions considered in simulating torque generated by individual fiber-optic laser beam on a microsphere (radius: *R*) located at (*D*, *H*). *D* is half the axial separation between the two fibers. The transverse offset of each beam is *h* (and that of each microsphere is *H*) from the center axis. Numerical simulation of torque as a function of: (b) transverse offset (*h*) for different sphere radii, (c) laser power and (d) axial offset (*D*), for different transverse offsets. [Figure adapted from (3)]

For different transverse offset (h), the increase slope in torque (with increasing laser power) varies, and the slope attains highest value when h=5 μm (Figure 1-11 (c)), which was also ascertained by our experiments. In all these simulations, axial offset (D) was kept 45 μm. In Figure 1-11 (d), we show numerical simulations of torque on the microsphere-assembly as a function of axial offset (D). With increasing axial offset (with fixed laser power, 20 mW and transverse offset being fixed), the torque was found to decrease in all settings of transverse offset (h) from 3 to 9 μm. This can be attributed to the fact that due to divergence of laser beam from the fiber, the intensity decreases away from the fiber end-face, which leads to decreased scattering force and, therefore, decreased torque (responsible for generating torque).

For determining the laser power to be used to achieve the required scanning (or rotation) speed (ω), we used stable torque simulated using equation (8) on a rotating thin disk16.

$$\tau = \frac{32}{3}\omega\eta\tilde{R}^3 \Rightarrow \omega = \frac{3\tau}{32\eta\tilde{R}^3} \qquad (10)$$

Where R□□ =3R is the total radius of the disk. This corresponds to a rotation speed of ~2.5 rad/s for a laser power of 20 mW and sphere radius of 3 μm, as compared to experimentally attained value of 4.1 rad/s. This may be attributed to the disk-like assumption of the microstructure in

viscous torque calculation (equation 6). As discussed earlier, the torque and hence rotation speed increases with increasing laser power and the rate of increase is highest for transverse offset of 5 µm for our microstructure. Therefore, this transverse offset value was chosen for further experiments.

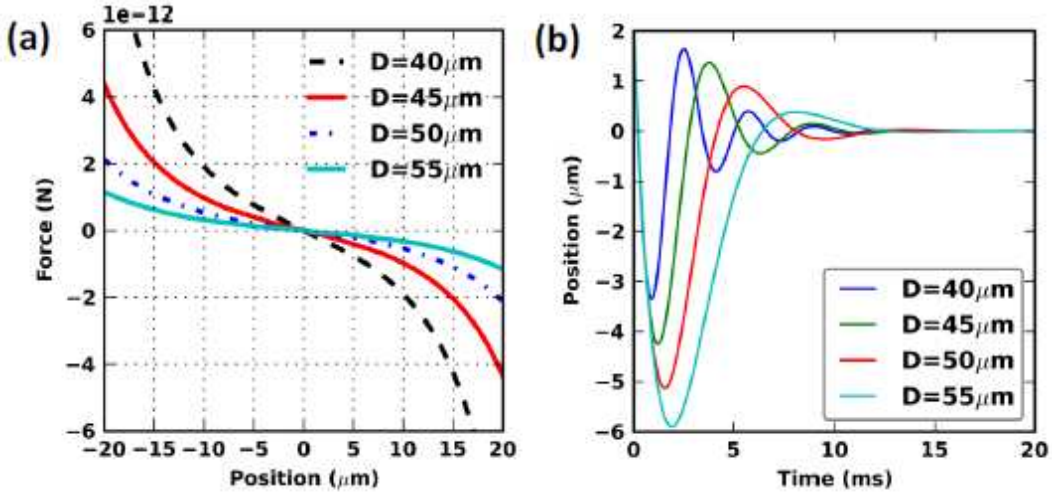

Figure 1-12 Numerical simulation of (a) the net force acting on and (b) the dynamics of stabilization for the disk-like microsphere assembly for different axial offset (D).

Controlled rotation is predicated on the stability of the system. The stability of the object in the fiber-optic spanner is critical to controlled rotation. Though, experimentally, the system was found observed to be stable, we carried out simulations for spatial as well as temporal stability analysis in the longitudinal direction. Due to the divergence of the two counter-propagating beams having transverse offset, the effective force

points to the centroid of the system. Figure 1-12 (a) shows the net force on the object as a function of position (displacement of the object from the centroid) for D (axial offset, as defined in Figure 1-11 (a)) values varying from 40 µm to 55 µm while keeping the other parameters as default. One can observe that the force is restoring in nature, i.e. the net force is positive when the object has negative displacement from the centroid of the system. For the geometry investigated here, the trapping stiffness was found to be increase with decreased in axial offset (D). For evaluating temporal stability of the object, drag friction of the medium (here, water) was taken into consideration. In our simulation, the drag force is computed as f_D=-12πηRv, where η,R, and v are the viscosity of water, the radius of the sphere, and the velocity of the spheres, respectively. By applying the Newton's second law of motion,

$$m\ddot{x} = f_B + f_D = f_B - 12\pi\eta R\dot{x} \quad (11)$$

where f_B is the net force of the beams (shown in Figure 1-12) and m is the mass of the objects computed using the density of white blood cell (1.05 x 10^3 kg m^{-3}). We set the initial velocity x□□ □= -3 mm/s, and position deviation x = 2 µm and the simulation results are shown in Figure 1-12, where position denotes the deviation of the objects from the centroid of the system. These results indicate that the objects will converge to the centroid due to the damped vibration.

Chapter 2

Focused Light as a Cutting Tool

An Introduction to Biological Tissue Ablation

Ablation is the process of removing material by evaporation, sublimation, or plasma formation. Using a pulsed laser with sufficient intensity, light is capable of efficient plasma formation in biological tissues and highly localized ablation. When a laser microbeam is incident upon a biological sample, the sample material absorbs the irradiation either through single photon absorption or nonlinear (multi-photon) absorption, depending on the irradiation frequency, the intensity (laser power per area) and the pulse duration (36, 37). While both single photon and nonlinear irradiation can lead to material ablation, single photon absorption can lead to varied deposition of laser energy, causing more extensive damage throughout the cell/sample (37). It is the peak power of the laser source that dictates the efficiency of the desired nonlinear processes. The peak power, which is defined as (pulse energy)/(pulse duration), is insufficient to elicit nonlinear absorption in the case of nanosecond pulse durations (36). It is therefore necessary to shorten the pulse duration from nanoseconds to femtoseconds (while maintaining constant laser-pulse energy) or increase the laser pulse energy. However, increasing the pulse energy can lead to heating, shockwave production,

and cavitation bubble formation, which all lead to spatially extended damage (38, 39). Therefore, nonlinear absorption (and therefore shorter pulse duration) is preferred since it is this multiphoton absorption process that initiates the localized chemical decomposition of the sample (37).

The simultaneous absorption of multiple photons excites a valence electron to a quasi-ionized electron state in the conduction band (37, 40). This excited electron is the initial ‘seed electron’ for plasma mediated ablation process. Once the first seed electron has been promoted to the conduction band, it begins to absorb single photons within the pulse duration of the laser, reaching higher energy states within the conduction band (37, 40). It does this until the kinetic energy of the electron is sufficient to impact ionize a new seed electron from the valence band. Once this happens, these two electrons now repeat the process; reaching the threshold energy necessary to impact-ionize more electrons. Energy is gained through impact ionization and new seed electrons are promoted to the conduction band until a critical number of these ionized electrons is reached, where decomposition of the material occurs. For an excitation wavelength of 800nm, N = 1021 cm-3. A value at which the plasma becomes reflective (37, 40), and is referred to as the plasma at optical breakdown.

The combination of the mulitphoton absorption process, the lower threshold energy required for optical breakdown, the lower temperature rise in comparison to longer pulse durations and the strong confinement of energy in the focal volume are the main factors that make the femtosecond laser an attractive tool for tissue ablation. In addition to the well-defined ablation thresholds associated with femtosecond laser pulses, using NIR wavelengths increases the plasma formation efficiency, since both the plasma absorption coefficient and cascade ionization rate are proportional to the square of the excitation wavelength. Therefore, a shift in the excitation wavelength from the visible to NIR increases the production rate of ionized electrons. However, at the expense of shifting the wavelengths to the NIR, a higher pulse energy is required to induce multiphoton absorption. It has been theoretically demonstrated that cascade ionization is the more dominant process when it comes to creating ionized electrons (opposed to multiphoton absorption alone).

Optical Poration of Rat Cortical Neurons

The selective insertion of foreign molecules, including many fluorescent markers, into living cells has been a challenging problem in cell biology due to the cell membrane's selective permeability. However, it is often necessary that researchers insert such molecules and markers into cells for various dynamical and drug delivery studies. This problem

becomes even more challenging if the study is to be limited to specific cells within a larger population, since other transfection methods such as viral transfection and lipofection are not realizable with a high degree of spatial selectivity. Here, we have used a focused femtosecond laser beam to create a small transient hole in the cellular membrane (optoporation) in order to inject nanomolar concentrations of rhodamine phalloidin (an impermeable filamentous actin dye molecule) into single viable mammalian cells (both HEK and primary cortical neurons). Following optoporation, the dye bound to the intracellular actin network and a clear and correlated clear rise in fluorescence intensity was observed. Theoretical dynamics of such a dye's diffusion are discussed, and numerical simulations of diffusion time constants are found to match well with experimental values.

It is important in many biological and medical studies to introduce exogenous dye molecules into cells to facilitate visualization of filamentous actin, tubulin, and to observe genetic modification/stimulation and functional alteration (41) of cellular processes. Several mechanical methods have been developed to accomplish this, with the two most widely employed methods being electroporation (42) and microinjection (43). These methods are either highly invasive, increase the possibility of contamination, or lack spatial and temporal specificity. For example,

microinjection frequently causes unintended cell damage, whereas electroporation has been reported to achieve relatively low efficiencies (44). Chemical methods have also been employed for the introduction of exogenous factors, such as lipofection, dextrant, and viral transfection (45, 46). These methods may have adverse chemical effects (47), do not allow for single cell specificity, and are currently only relevant to large populations of cells. With the advent of laser technology, light has been utilized for numerous applications, such as micro-surgery and cell healing (48, 49). Optical poration (or photoporation, optoporation) is a purely optical method of creating a transient hole in a cell membrane or organelle by briefly (on the scale of milliseconds) exposing it to a focused pulsed laser of sufficient intensity (50). In the case of in vitro studies, this method allows for single cells to be targeted, and may be interfaced with microfluidic devices or additional, fast-scanning optics for relatively high-throughput studies. Furthermore, since the entire system is can be enclosed and since optical poration is a non-contact method, this method is both highly spatially and temporally selective and it is absolutely sterile.

The primary mechanism by which the membrane is porated is still uncertain, though many hypotheses have been proposed, such as plasma break down, cavity formation, local heating, shock wave formation, and photo-acoustic effects (51, 52). Due to our use of a femtosecond pulsing

laser, we have assumed that direct plasma breakdown is the primary cause of the optoporation effect. However, there is also evidence to support the shock wave hypothesis (53, 54). When the ionized electron density exceeds some critical value at the focal plane, it leads to chemical dissociation of the cell membrane and the formation of a membrane pore (or hole). The size of the hole which is formed during laser irradiance is dependent upon the pulse-energy, pulse-width, and wavelength of the light being used. Since the diffraction-limited spot size is directly proportional to the wavelength of light, various wavelengths have been used for optoporation, ranging from ultra-violet (UV) to near-infrared (NIR) regimes. UV light carries a high risk of damage to the cells since it is highly absorbed by the cell's nucleus. Therefore, the use of UV light may not be suitable (55, 56). CW argon lasers operating at 488 nm, or Nd:YAG lasers which operate at 532 nm, have also been employed for optoporation. However, many cell organelles have high absorption at these wavelengths, so the possibility of detrimental effects at these, and others wavelengths in the visible range, cannot be ruled out. It is now well known that the absorption of light by intracellular components is low in the near infrared (NIR, 700 to 1000 nm) range. This range of wavelengths is, in fact, often referred to as the 'therapeutic window' for their ability to probe biological samples with low deleterious effects. We have chosen to

use wavelengths of 800-850 nm, as that is where our laser is most stable and has the lowest pulse width (100 fs) (57).

Cell Culture

All experimental procedures were conducted according to Institutional Animal Care and Use Committee approved protocol. HEK 293 cells were routinely cultured in Dulbecco's modified eagle's medium (DMEM, Sigma Aldrich), supplemented with 10% fetal bovine serum (FBS, Sigma Aldrich) and 1% Penicillin/streptomycin antibiotics. For laser-assisted insertion of rhodamine phalloidin (RP) (Cytoskeleton, Inc), cells were trypsinized and plated on poly-D-lysine coated glass-bottom 35 mm Petri dishes (MatTek Corporation). The cortical neurons were isolated from embryonic 18 day rat embryos. The cortical tissues were dissected, cleaned (meningeal layer), enzymatically dissociated (0.125% trypsin in L-15 medium) for 20 minutes at 37 oC. The dissociated cortical neurons (100,000/device) were seeded on Poly-D-lysine (PDL, 0.01%, Sigma) pre-coated coverglass with Polydimethylsiloxane barrier (Sylgard 184, Dow corning), and the serum-free culture medium (Neurobasal medium supplemented B-27 with BDNF and NT-3, 10 ng/ml) was changed every 3 days. The cell cultures were maintained at 37℃ in a 5% CO2, humidified atmosphere prior to experiments. No special environmental conditions were maintained during optoporation experiments (room temperature,

etc.) in the case of HEK cells. In the case of experiments performed on RCNs, temperature, humidity, and CO2 levels were maintained at all times.

Dye Selection

Propidium iodide and calcein have been widely used for demonstrating optical transfection, as they are impermeable and easily stain the nucleus and intracellular calcium, respectively (58, 59). Here, we have selected RP, a dye marker which is routinely used in visualizing filamentous actin, and is impermeable as well as toxic at higher concentrations. This toxicity has limited RP studies to cells which are fixed, and therefore no longer viable for dynamical study. Among Our challenges was to determine an optimal concentration of RP which would allow for filamentous actin imaging, as well as ensure the cell's survival following poration. The determination and implementation of these parameters will allow for the dynamical study of filamentous actin polymerization and cytoskeletal reorganization in viable cells. The cell medium (DMEM) was removed and new medium with RP dye was added and incubated for 15 minutes prior to optoporation. Calcian-AM (4 µM) was used to stain the cells following optoporation to determine the viability of the cells.

Optical Set Up

A schematic diagram of the experimental setup is shown in Figure 2-4. A tunable (690 - 1040 nm) Ti:Sapphire laser (Newport Spectra-Physics, Inc.) beam (rep rate: 80 MHz, pulse width: ~100 fs) was directed toward the sample by a dichroic mirror (DM1) through an inverted optical microscope (Nikon eclipse Ti). A 100x (NA = 1.4) objective was used to focus the laser beam to a diffraction limited spot at the top surface of the cell as shown in fig 1(a). Special steps were taken to ensure that the laser focal plane was equal to the imaging focal plane. A second dichroic mirror (DM2) was used to reflect the fluorescence excitation light from the mercury lamp (Nikon) along the same path as the fs laser. In the same filter cube as DM2, the excitation (Ex) and emission filters (Em) were used to transmit andcollect the appropriate bands of visible light to and from our sample, as well as block any remaining backscattered laser light. All images were acquired by cooled EMCCD (Cascade, Photometrics) and processed with imageJ (NIH) software. The number of fs laser pulses irradiating each sample was controlled by an external mechanical shutter (S, Uniblitz Inc.). The sample-site laser beam power was controlled by the fs laser software (Mai Tai), with fine adjustments made by altering the orientation of the polarizer (P). The sample-site beam power (after the objective) was calculated by multiplying the transmission factor of the

microscope objective with the power measured at the back aperture of the objective. Fluorescence and bright field images were taken before and after optoporation experiments, with sequences of fluorescence images taken in order to monitor the rise in fluorescence intensity with time.

Optimization of Concentration and Laser Parameters

It is known that the Rhodamine family of dyes is toxic to living cells, and can cause or contribute to cell death (60). Therefore, a majority of experiments in which the cytoskeletal filamentous actin network is stained are performed on fixed cells. Here, we have determined a window of optimized RP dye concentration by monitoring the cell viability and fluorescence due to poration (injection). All other optical parameters were kept constant while the molarity was increased from 126 to 168 to 188 nM. At 168 nM concentration, porated cells were observed to die (noticeable changes in morphology) and a sharp increase in fluorescence was observed immediately following poration.

Further optimization of the laser parameters was undertaken by modifying the laser power and exposure time (macro-pulse duration, 20 – 50 ms), while keeping the wavelength constant (800 nm). At higher average powers (above 130mW), HEK cells were observed to die (quick rise in fluorescence and significant change in morphology).

Femtosecond Laser-assisted Dye Injection

We used the optimized power, exposure time, and concentration to insert the RP, a dye which is well known to bind to actin filaments. First, we porated and injected RP into normal HEK cells. There was a clear, observable increase in the cell's fluorescence over a time period of approximately 10 minutes. We observed that the fluorescence signal increased slowly and ultimately reached a saturation level (independent of quenching) as predicted by Fick's law of diffusion. As can be clearly seen in, the most intense fluorescence is observed along the periphery of the cell's membrane, where the filamentous actin network is most dense. Next, we demonstrated the introduction of RP by optoporation into viable primary embryonic rat cortical neurons (RCNs). Figure 2-1 shows the significant increase in fluorescence which we observed in the soma as well as dendrites of the RCN. Furthermore, we have also shown the fluorescence during polymerization of action in the growth cone in the neuron. Hence, with optimized laser parameters and dye concentration, RP, which is cell impermeable, was successfully injected to the individually targeted cells.

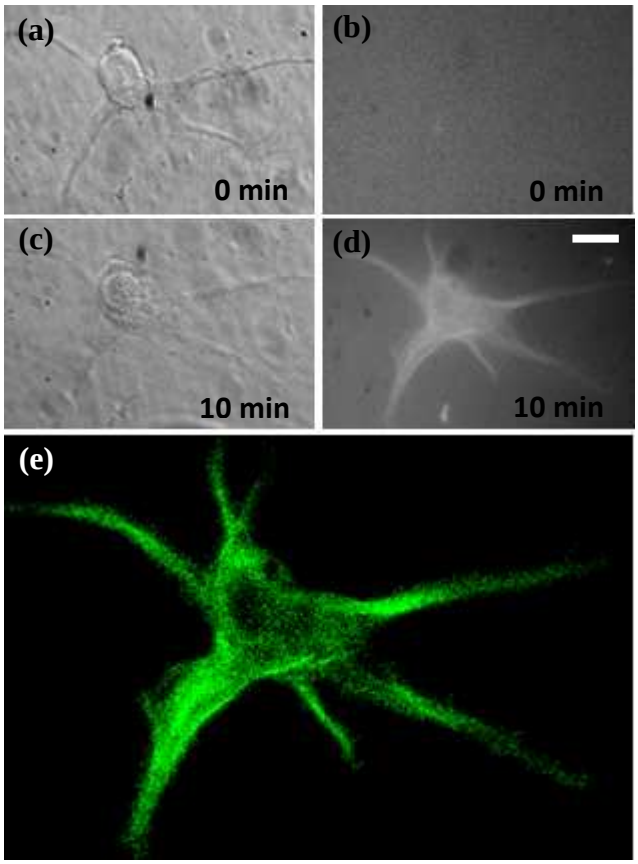

Figure 2-1 Optical poration of E18 rat cortical neuron in presence of 140 nM concentration rhodamine phalloidin. Bright field images prior to (a) and 10 minutes following (d) optical poration. Epifluorescence images prior to (b) and 10 minutes following (d) optical poration. (e) Pseudo-color image of fluorescent filamentous actin network following optical poration.

Many laser parameters, such as laser intensity, pulse width, repetition rate, and the focal volume (interaction volume) play important roles in laser-assisted optoporation. Optoporation is only possible when the intensity distribution reaches the threshold-value, producing a

sufficient free electron density at the focal volume. We are assuming that the mechanism of biological membrane ablation by femtoseond laser is primarily due to low density plasma formation at the focal volume. The low density plasma is formed by a multiphoton ionization process, often referred to as cascade or avalanche ionization. The energy of a single photon with wavelength of 800 nm is 1.56 eV. In order to cross the band gap, which we can take as 6.5 eV (that of water) for cell culture medium, we need at least five photons to cause electron transitions to the excitation band.

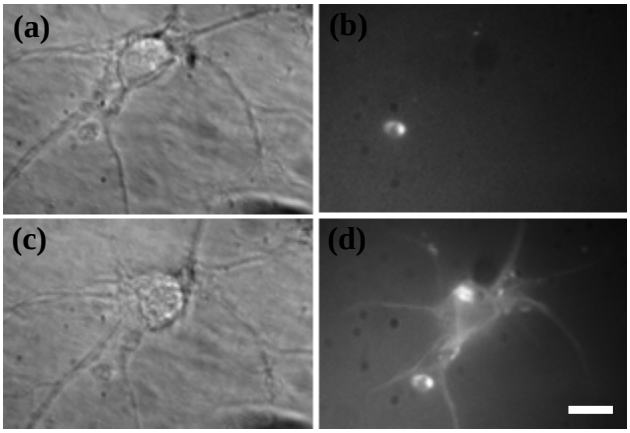

Figure 2-2 Femtosecond laser-mediated optical poration of E18 rat cortical neuron in the presence of 140 nM concentration rhodamine phalloidin. Bright field images prior to (a) and 10 minutes following (c) optical poration. Epifluorescent images prior to (b) and 10 minutes following (d) optical poration. Scale bar represents 10 μm.

The critical free electron density (plasma) at the laser's focus, above which laser ablation starts, is defined by

$$Q_{cr} = \frac{\omega^2 \varepsilon_0 m_c}{e^2} \tag{15}$$

where Qcr is the critical plasma density, ω is plasma frequency, ε0 is the dielectric constant in vacuum, and mc is the mass of the plasma. At 800 nm wavelength, this corresponds to a Qcr =1.8x1021 cm-3 and other investigators (61, 62) have correlated this to a necessary power density of 1.3-2.6x10^{13} W/cm^2. It is on this basis that we have chosen an experimental power density of 2.24 1013 W/cm2 during optoporation, which lies within the theoretically predicted limit.

The laser focal cross-section has been demonstrated to be an ellipsoid (63). The short (d) and long axes (l) of the ellipsoid focal spot are given by the following relations24, assuming a large solid angle.

$$d = \frac{1.22\lambda}{NA} \tag{16}$$

$$\frac{l}{d} = \frac{1 - \cos\alpha}{\sqrt{3 - 2\cos\alpha - \cos\alpha}} \tag{17}$$

which results in a short (d) and long (l) axis value of 750 and 1800 nm, respectively.

We have used the Gaussian distribution of laser irradiance at the focal volume with the above-mentioned major and minor axes to determine the ellipsoid distribution of irradiance.

$$I(r,z) = I(0,0)\exp\left(-2\left(\frac{r^2}{a^2}+\frac{z^2}{b^2}\right)\right) \tag{18}$$

where r and z are the coordinate in radial and axial distribution (a=d/2 and b=L/2).

The free electron density produced during the laser irradiation is proportional to the intensity Ik 25, where k is the number of photons required to ionize the medium (k = 5, in our case).

$$Q(r,z) = \left[I(0,0)\exp\left(-2\left(\frac{r^2}{a^2}+\frac{z^2}{b^2}\right)\right)\right]^K \tag{19}$$

$$Q(r,z) = Q(0,0)\exp\left(-2K\left(\frac{r^2}{a^2}+\frac{z^2}{b^2}\right)\right) \tag{20}$$

where Q(0,0) = I(0,0)k represents the free electron density at the center of the focal plane. Plots of equations 4 and 6 are shown in figure 3 (a and b). Experimentally, we have determined the pore's diameter to be approximately 1.6 µm, but theoretical calculations show that the ideal membrane pore might be significantly smaller than measured. Fig 3 (b and c) show the pore as observed at the instance of pulsed laser irradiation during bright-field imaging.

We have demonstrated the introduction of exogenous factors such as rhodamine phalloidin into living rat cortical neurons via optical poration. This method allows for the study of intracellular actin dynamics as well as the intracellular transport of components such as mitochondrial vesicles, which may be non-selectively stained by rhodamine phalloidin (Figure 2-3). This method has also been previously used for optical transfection of viral plasmids into living cells and offers the additional benefit of allowing large plasmids that may not enter the cell through some conventional transfection techniques.

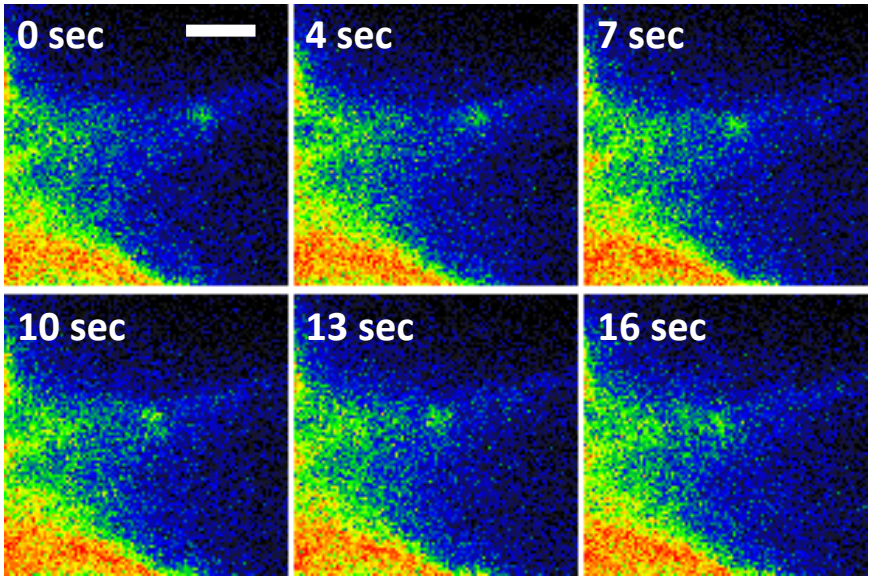

Figure 2-3 Pseudo-colored intensity image of intracellular transport of possible mitochondrial vesicle following optical poration and rhodamine phalloidin dye diffusion. 0 second time-stamp begins 10 minutes following optical poration. Scale bar represents 2 μm.

Degeneration and Regeneration In the Presence of Estrogen

An Introduction to Estrogen as a Neuroprotective

Estrogen is an important pleiotropic steroid hormone which is found in humans and regulates multiple functions in the body. Classically, estrogen is considered a “reproductive” hormone, due to its well-known role in feedback signaling in the hypothalamic-pituitary-ovarian axis as well as its known involvement in development, reproduction and sex differences in humans as well as other animals. The consideration of estrogen’s neuroprotective benefits was, in part, sparked by the observation of statistical bias between men and women in occurrence and severity of various neurodegenerative diseases and disorders (i.e. Alzheimer’s, schizophrenia (64), etc.), as well as maintenance of verbal, long and short term memory (65). Indirect scientific evidence that estrogen may be neuroprotective first arose from studies of such sex differences following brain injuries in animals (66). There is now considerable significant evidence to support that estrogen directly and indirectly protects central nervous system (CNS) neurons subsequent to acute (67) as well as diffuse (68, 69). For example, female rats have been reported to have greater survival rates as compared to males following diffuse traumatic brain injury (68). A number of studies have documented that women are “protected” against stroke relative to men – at least until the

years of menopause, when estrogen levels decline (70, 71). In addition to a potential direct protective action on neurons, there is evidence that estrogen may also have indirect effects on other cell types such as astrocytes and microglia that may facilitate its neuroprotective action in neurodegenerative disorders (72-74). After neuronal injury and in many neurodegenerative disorders, activated microglia are known to secrete proinflammatory factors that can contribute to the progressive neural damage. Studies have also suggested that estrogen may suppress microglial activation (75). In addition to ameliorating neurological dysfunction, estrogen's neurotrophic and neuroprotective effects may extend to optic nerve pathways. In fact, it has been shown in rat/mouse models that 17-β estradiol may have neuroprotective effects against axotomized RGC cell death (76) as well as inherited glaucoma, the second leading cause of blindness in the world. What began as observational evidence has now blossomed into an entire field of research, and along those same lines, we were interested to see whether or not the presence of exogenous 17-β estradiol could mitigate, or reverse, the traumatic effects of optic neuropathy in single primary retinal ganglion cells (RGC) axons (in vitro) caused by femtosecond (fs) laser microsurgery.

Optic nerve damage can be the result of infection, trauma, glaucoma, or malignancy. This damage can result in pain, vision distortion, and even blindness and therefore necessitates treatment options which mitigate the spatial scope and severity of optic nerve damage. It may be possible that a treatment option is already being produced within our bodies.

Laser microbeam irradiation provides a unique opportunity to induce highly localized and controlled levels of damage to various parts of a single axon, thus allowing analysis of the relative contribution of localized damage to overall neuron functionality and its subsequent repair processes. Using a laser microbeam, whole cells (77) as well as intracellular organelles (78, 79) can be altered with high spatial (sub-µm) and temporal resolution without significantly damaging more proximal regions. Such microbeams have allowed nanosurgery of individual neuronal axons growing in culture (80) as well as in organisms such as Caenorhabditis elegans (81). Due to this precision of focused laser beam, combined with non-invasive nature of the near-IR laser microbeam as compared to invasive needles, several measurements on axonal regeneration in PNS have been quantified. Most of these studies are focused on PNS regeneration and complete transection of the axon.

Here, we evaluate the effects of 17-β-estradiol on single retinal ganglion cell axons subsequent to femtosecond-laser-induced axotomy in vitro. We demonstrate that 17-β estradiol reduces the period of degeneration and incubation (before regeneration), and increases the successful regenerative frequency and rate for single RGC axons subsequent to fs pulsed-laser-induced axotomy, and effectively serves as a neuroprotective agent. Furthermore, by varying the concentrations of estradiol, we have found that this mitigating effect is dose-dependent, and can be further optimized for effect. In this way, estradiol may be an excellent candidate for clinical attenuation of optic nerve damage if administered in a timely manner.

Materials and Methods

Primary Retina Explants Culture

Common goldfish (Carassius auratus) retinal ganglion explants were chosen for all degenerative/regenerative studies due to their established ability to regenerate following axotomy16, as well as their widely accepted use as a human optical pathway model. Adult goldfish, 5-7 cm in total body length, were housed in standard glass aquaria at 19°-21℃. In order to facilitate axonal outgrowth in cu lture, fish received a priming lesion of the optic nerve at least one week prior to removing the retina17-18. Following anesthesia with tricaine methanesulfonate (Argent),

the optic nerve was visualized through an incision in the dorsal-posterior conjunctiva and crushed with Dumont #5 forceps in the distal region, where the nerve exits the ocular orbit. Special care was taken to avoid damaging the large blood vessel which runs alongside the optic nerve. One to two weeks after receiving the priming lesion, both eyes were removed from the anesthetized goldfish after following one hour of dark adaptation to facilitate removal of the pigment epithelium, washed in 20% ethanol, and then washed in medium. The retinas were carefully removed, washed twice in medium, and cut into 400 μm square explants on a McIlwain tissue chopper. The explants were then placed into sterile 35 mm Petri dishes with a 14 mm central hole backed with a glass coverslip (MatTek). The coverslip had been previously coated with 0.75 mg/dish poly-D-lysine (Sigma, >300,000 MW in borate buffer, pH 8.3) and 5 μg/dish of laminin (BD Biosciences, in phosphate-buffered saline, pH 7.4). The explants were then oriented by hand so that the ganglion cell side faced towards the laminin, and incubated at room air-mixture and temperature in Leibovitz's L15 medium (Sigma). This medium was supplemented with 10% fetal bovine serum (Fisher Scientific) and 50 μg/ml gentamicin. Since goldfish are poikilothermic, the retina cells could be imaged in vitro at room temperature.

Fs Laser Axotomy and Imaging Platform

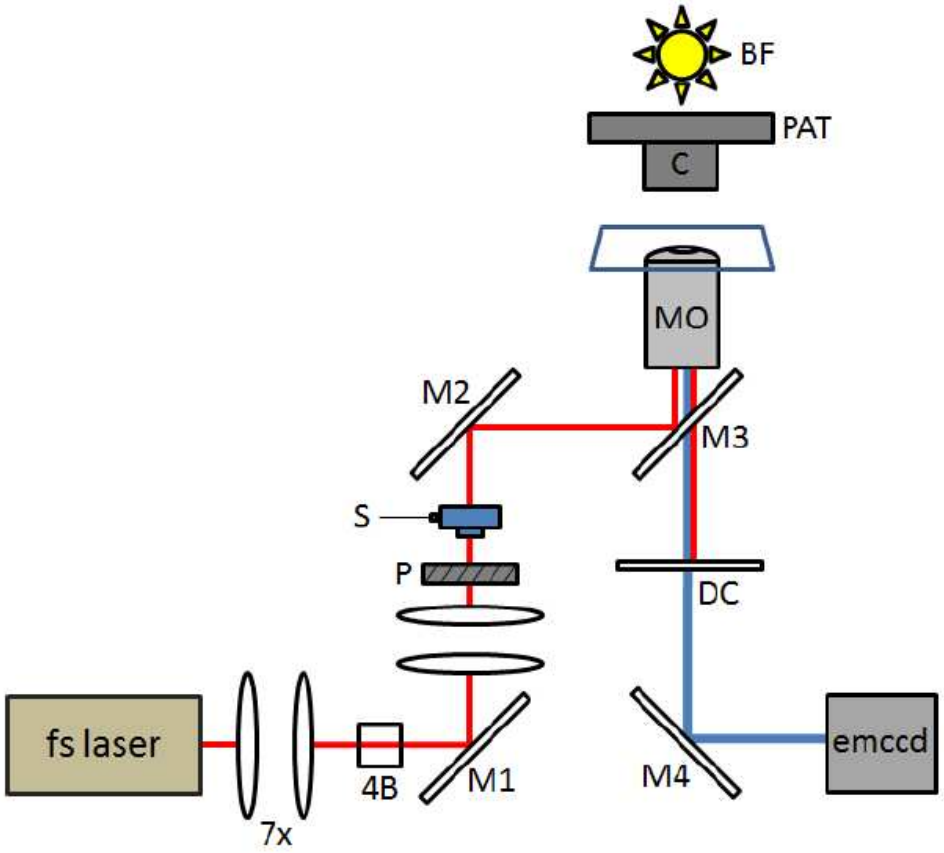

Figure 2-4 Schematic of phase-contrast imaging and laser manipulation platform. fs laser: Femtosecond, tunable TI: sapphire laser. 7x: 7x beam expander and collimator. 4B: Four-way beam splitter. M1, M2: Adjustable mirrors >93% reflectivity. P: Polarizer. S: External controlled shutter (Uniblitz). MO: 100X, Phase 3, N.A.: 1.3, oil immersion microscope objective. C: condenser. PAT: Phase annulus turret. BF: Bright field. DC: dichroic mirror mount. EMCCD: EMCCD camera (Phtotometrics).

Figure 2-4 shows the schematic of the microscopic imaging and laser-microbeam manipulation platform. Fs laser axotomy of healthy advancing goldfish RGC axons was achieved with a tunable Ti: Sapphire laser (MaiTai HP, Newport-SpectraPhysics). Operational pulse width and repetition rate were ~200 fs and 80 MHz (at 785nm) respectively. The beam was operated in mode-lock-on condition to ensure pulsing-mode usage. The near-infrared laser beam was expanded and collimated by 7X beam expander (1 to 7 mm) and relayed via folding mirrors to the back laser port of a Nikon, Ti-U Eclipse inverted microscope. The dichroic mirror (DC) and filter set couples the laser beam upwards into the microscope objective (100X, Ph 3, oil immersion, N.A.: 1.3) to form a tightly focuses laser beam, and filters out the downward-path laser beam reflected from the surfaces of the objective and coverslip. This prevents the reflected laser coupling into the oculars or the CCD camera, which can dazzle the field of view. An external mechanical shutter (Uniblitz) was placed in the beam path, and used to activate macropulses of the laser beam. The wavelength and source-power of the laser beam was adjusted via Mai Tai software. Fine adjustments to the sample-site power were made using polarizer (P). Sample sitepower was calculated by measuring incident beam power below the back aperture of the microscope objective and multiplying this value by the MO transmission coefficient. Since

neurons are (semi-) transparent, visualization was achieved using phase contrast microscopy. A phase annulus turret (PAT) was fixed above the microscope condenser (C), in the path of the bright field (BF) source, and configured with a phase-3 condenser annulus (to correspond to the microscope objective internal phase plate). Using live image capture, the center of the laser spot was located and marked using ImageJ point tool prior to all experiments. The microscope filter-set was then adjusted to block the reflected laser spot using internal dichroic mirror (DC).

Results

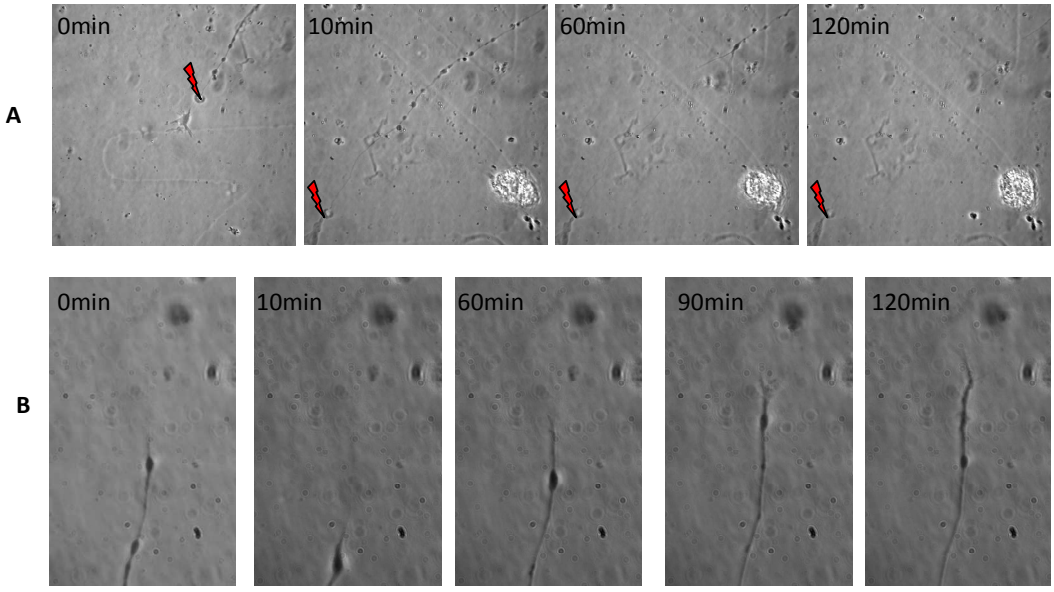

Figure 2-5 Effect of estrogen on repair/regeneration. Time-lapse images of (A) negative control and (B) 100 nM estradiol. Injury site marked as red lightning bolt.

In order to study the role of estrogen in axon repair and regeneration, fs pulsed laser axotomy was performed on RGC axons cultured in the presence of varying concentrations of estrogen (1 nM, 10 nM, 100 nM) as well as control (no estrogen). Axons were injured at the distal end, adjacent to the growth cone, by 20 ms macropulse exposure of tightly focused laser microbeam (785 nm, average power: 90 mW). This injury was applied to randomly selected axons, whose degeneration and regeneration (in cases where it occurred) was monitored by time-lapse phase-contrast imaging.

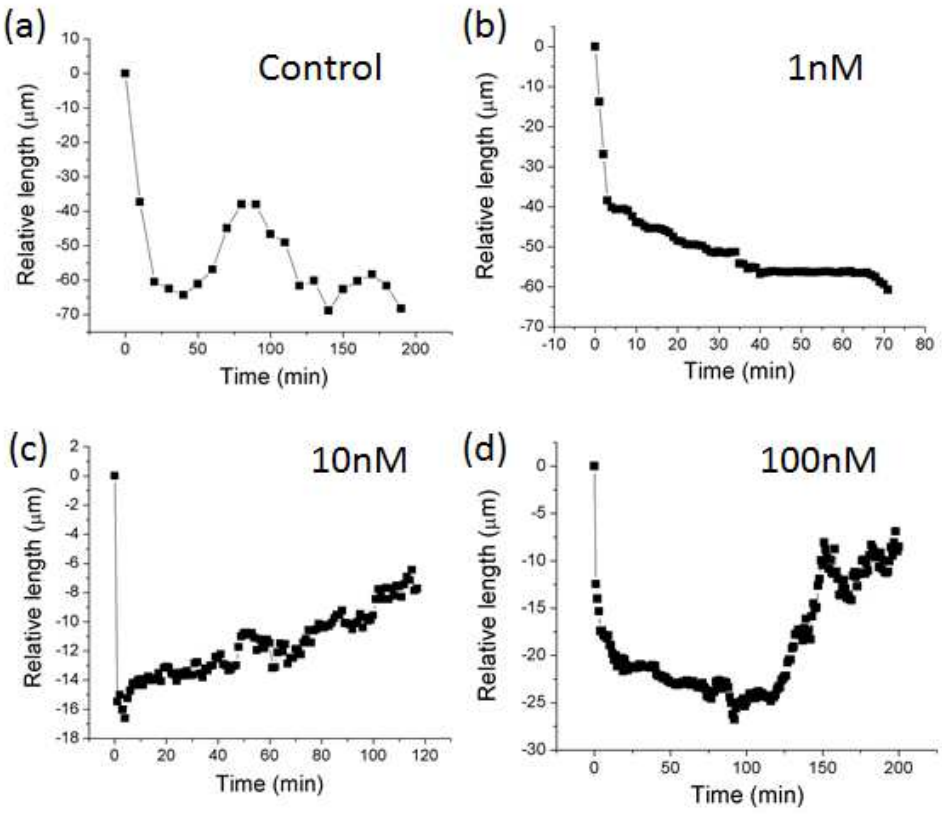

Figure 2-6 Corresponding graph of relative length as a function of time following fs pulsed laser axotomy. Characteristic plots of relative length as function of time for (a) control, (b) 1 nM, (c) 10 nM, and (d) 100 nM concentrations of estrogen.

In the case of negative control (no estrogen), the proximal end of axon retracted immediately after laser axotomy (laser damage spot marked by lightning bolt, Figure 2-5 A) and continued to degenerate. Repair (formation of growth cone) of the injured axon was observed only after ~150 min. In presence of estradiol (10 nM), though the proximal end

of axon retracted immediately after laser axotomy, repair (formation of growth cone) of the injured axon occurred as early as ~60 min. Effect of estrogen on axonal regeneration is shown as time-lapse images in Figure 2-7.

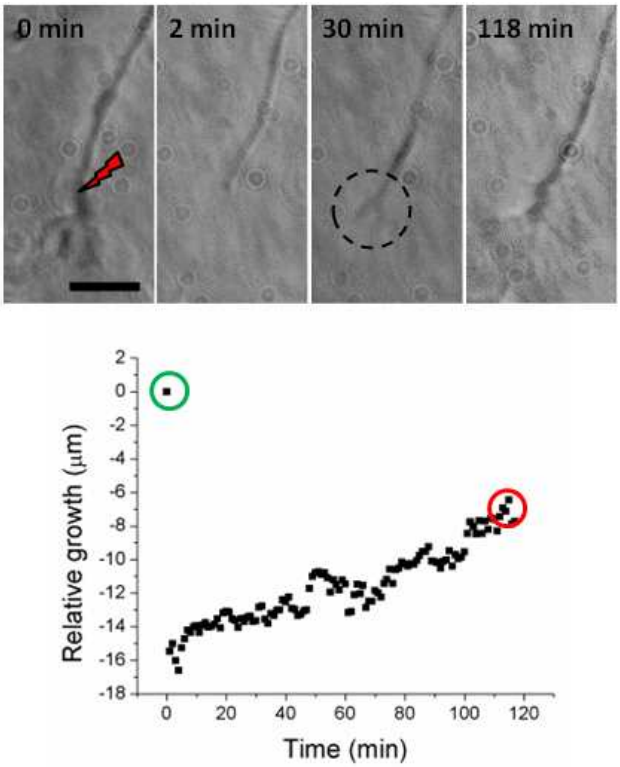

Figure 2-7 Time-lapse images of axon treated with 10 nM estrogen prior and subsequent to fs pulsed laser axotomy. Red lightning bolt indicates damage site. Dashed circle highlights observed re-emergence of growth cone. Scale bar represents 6 μm.

It was observed that estrogen effectively served as a neuroprotective, given the future determination of an optimal concentration

for use on RGC axons. Panel A of Figure 2-7 shows time-lapse images of the degeneration-regeneration process. Randomly-selected axons treated with 10 nM concentration of estrogen were subjected to laser beam axotomy with irradiation parameters similar to earlier case. The proximal end of the axon is seen (Figure 2-7 (a)) to retract immediately following application of fs laser pulse (20 ms). However, regeneration of the injured axon occurred only after 4 min following of axotomy. Further, reformation of the growth cone occurred was observed within 60 min, in cases of 10nM estrogen treatment. It may be noted that no significant growth cone reformation was observed in cases of control axons (imaging up through 270 min of after axotomy). Regeneration occurred in all (100%) experimental instances involving neurons treated with 10 nM estrogen (n = 5), whereas control experiments resulted in regeneration in 67% of experiments. To further quantify the effect of estrogen on degeneration and regeneration, kinetics of axonal retraction or growth was plotted as a function of elapsed time after laser axotomy. Figure 2-6 shows characteristic plots of relative length of axon as function of time for control (no estrogen). Figure 2-6 shows the kinetics of retraction/regeneration for axons treated with concentrations of (b) 1 nM, (c) 10 nM and (d) 100 nM estrogen. The kinetics of axonal regeneration can be seen to be quite different and dependent on estrogen concentration.

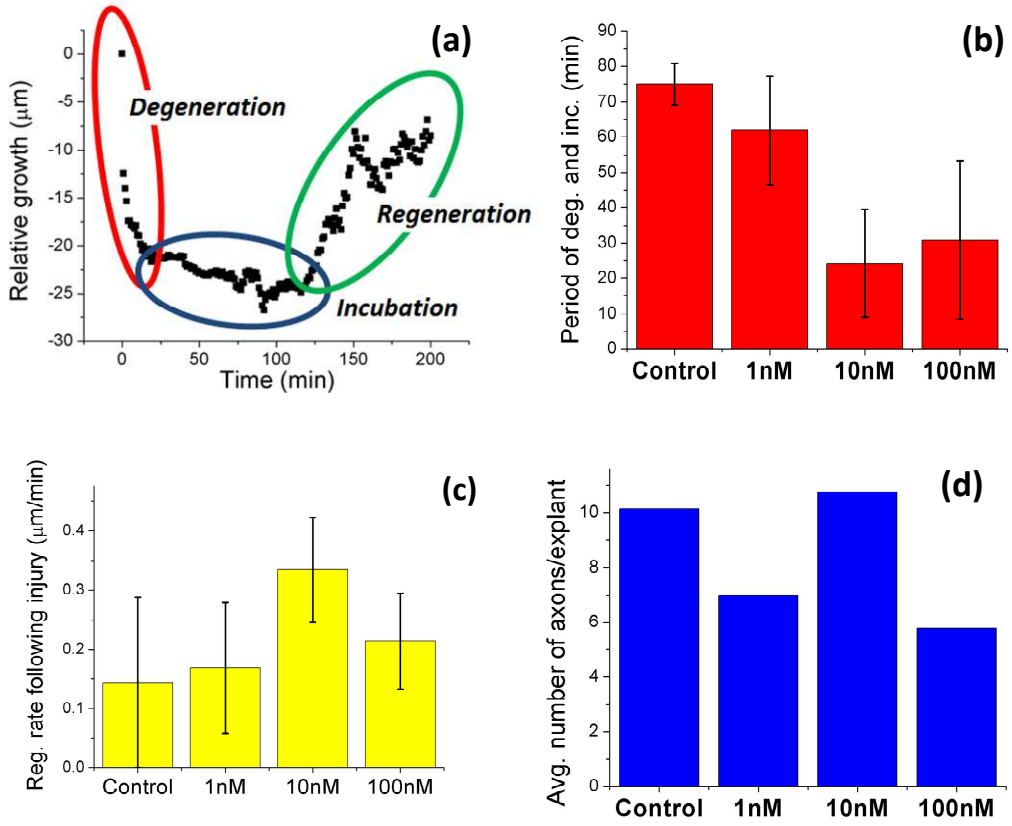

Figure 2-8 (a) What we have defined as degeneration, incubation, and regeneration. (b) Average combined periods of degeneration and incubation following axotomy. (c) Regeneration rates following axotomy. (d) Average number of axons per explant on second day following extraction and culture (9 days following optic nerve crush).

To characterize the protection as well as the regeneration role of estrogen, we defined degeneration period as the time from initiation of injury (by laser microbeam) until the proximal end stops retraction from the injury site (or proximal end). The degeneration period in a typical kinetics-

plot is shown in Figure 2-8 (a). Further, we defined the period of incubation as the duration from no-further-degeneration state to the time point of re-growth of the injured-axon (Figure 2-8 (a)). In the axonal growth kinetics graph, regeneration period is assigned to the phase when the growth cone begins to advance from the point of incubation (static) until the period of observation as marked in Figure 2-8 (a). In order to quantify the effect of estrogen in protecting axonal injury, we combined the periods of degeneration and incubation following axotomy. Figure 2-8 (b) shows the comparative histogram of the mean values of combined periods of degeneration and incubation following axotomy for axons incubated with different concentrations of estrogen. The error bars shows the standard deviation around the average values. The period of degeneration and incubation was found to decrease for the 10 nM incubation (24.25 ± 15.2 min) as compared to that for the control (0.31 ± 0.28 respectively). However, the increase in estrogen concentration from 0 to 1 nM did not lead to significant decrease in the degeneration and incubation period. Further, increase in estrogen concentration to 100 nM lead to reduction of the protective effect of estrogen against degeneration caused by fs laser axotomy. However, the distinctively protective role of estrogen can be seen from the statistically significant decrease in period of degeneration and incubation for axons treated with 10 nM and 100 nM. Hence, we

concluded that incubation of axons with 10 nM Estrogen is optimal for axonal protection against severe injury such as laser axotomy.

Along with likelihood of regeneration, regeneration rates (calculated by the slope of the regeneration region only, Figure 2-8 (a)) were also found to improve for certain concentrations of estrogen. Regeneration rates following fs laser injury were 0.23 ± 0.23 µm/min, 0.34 ± 0.22 µm/min, 0.21 ± 0.18 µm/min, and 0.31 ± 0.28 µm/min for 1 nM, 10 nM, 100 nM and control (0 nM) respectively. Figure 2-8 (c) shows the regeneration rates following axotomy for different estrogen incubation concentrations. The regeneration rate was found to be significantly dependent on estrogen concentration (Figure 2-8 (c)), when the regeneration rate following laser axotomy was calculated as slope of line from end-point of degeneration to the end-point of observation (i.e. including incubation duration with regeneration period). The optimal estrogen concentration for maximal regeneration was found to be 10 nM. Surprisingly, the dependence of regeneration (Figure 2-8 (c)), was found to be similar to the regeneration subsequent to injury caused by mechanical dissection of axons as estimated by average number of axons per explant on second day following extraction (Figure 2-8 (d)). This led us to believe that laser axotomy can simulate conditions similar to mechanical injury and therefore should be well-suited for axonal injury-

repair studies. These results also indicated that protection/regeneration effect of estrogen is ubiquitous, irrespective of the method of injury (laser or mechanical).

Discussion

Estrogen has been implicated in neuroprotection since clinicians first observed significant sex differences in the onset and outcomes of various neurodegenerative diseases, as well as sex differences in the rate of recovery following brain injuries. In general, it is known that steroid hormones play a critical role in neurogenesis, neuroprotection, and in the repair and regeneration of injured neurons (82, 83). We have confirmed estrogen's neuroprotective qualities as applied to single primary RGC axons in vitro. While further studies will need to be conducted in order to find optimal concentrations and complete the hormesis curve, we feel confident that concentrations between 10 and 50 nM will continue to yield positive results as compared to control studies. While the exogenous estradiol concentrations used in our study are non-physiological (Typical serum levels in an adult male are between 0.05 and 0.2 nM), other studies which have reported significant neurodamaging effects due to the addition of exogenous estradiol used concentrations several of orders of magnitude higher (84). The detailed mechanism of estrogen mediated neurogenesis, regeneration and repair still remains elusive and proving

such a neuroprotective role in vivo is not straight forward, as the functions of estrogen are so closely associated with functions and presence other hormones (androgen, progestin, testosterone), that consideration of estrogen as an independent neuroprotective in vivo becomes very difficult.

Furthermore, since estrogen is known to stimulate the release of nitric oxide and reduce cholesterol, as well as alter immune functions, the neuroprotective effects of estrogen may be indirect, first altering the health of other organs. Besides the clinical implications that estrogen has direct protective effects on neurons, it has been documented that estrogen may also indirectly affect other support cells, such as astrocytes and microglia (72, 75, 85). Estrogen also stimulates expression of various neurotrophic factors (e.g. NGF, BDNF) and stimulates axonal regeneration25. Neurotrophins are important regulators of neural development, survival, function, and plasticity. Nerve growth factor (NGF), brain-derived neurotrophic factor (BDNF), neurotrophin-3, and neurotrophin-4, are few well-characterized neurotrophins. Neurotrophin levels are modulated at the sites of injury that affects the neuronal repair and regeneration processes. Therefore, additional biochemical characterizations will be necessary to further elucidate the pathways by which estrogen establishes its neuroprotective and neuro-regenerative effects.

Is Pathfinding Dependent on the Degree of the Initial Injury During Axonal Regeneration?

Fs laser axotomy was performed on 25 healthy, growing RGC axons. Of these axons, 10 (40%) were observed to regenerate within 300 minutes. Axons were injured on the axon shaft, just anterior to the lamellipodium (growth cone) with pulsed sample-site laser power of 150mW (at 785nm). Three distinct and reproducible injuries were performed using varying laser irradiation conditions. For simplicity, I will hereafter refer to these three types of injuries as thin, cut, and burn. Thin injuries (n=4) were achieved by using the external shutter to activate a single 20ms macropulse of fs laser beam (150mW) slightly off-center of the axon's shaft. A cut (n=3) was achieved by activating single 20ms macropule of pulsed laser beam on axial center of the axon's shaft while taking extra care to focus within the transverse diameter of the axon's shaft.

Burn (n=3) injuries were achieved by manually opening (by hand) the external shutter for ~0.25 seconds, with special care taken to center the incident beam on the axial center of the axon, and to focus on the upper plane of the coverslip, where the axon adheres. It is important to note that all reported injuries ultimately resulted is the physical dissociation of the axonal shaft from the lamellipodium (growth cone).

Materials and Methods

Besides the distinctions covered in the introduction, the materials and methods of degree-of-injury experiments are identical to that of section Chapter 0.

Results

In order to study the effects of varying degrees of initial injury on the degeneration, regeneration, and subsequent pathfinding abilities of primary CNS axons, fs pulsed laser microbeam (785nm) was applied at sufficient power (150mW), focus (1.3 N.A. MO) and repetition rate (80MHz) to effectively ablate tissue on the distal end of axon shafts in petri dish. Three distinct degrees of initial injury (thin, cut, and burn) were reproducibly applied to randomly selected RGC axons (n=25) by altering the position, intensity (focus) and macropulse exposure of the incident laser beam. Axons which did not regenerate within ~200 minutes following fs laser axotomy were not included in calculations or statistics. Time-lapse images in Figure 2-9 (at t=0 min) show the characteristic differences in the degree of initial injury the axons received. Subsequent time-lapse images (Figure 2-9) illustrate the characteristic differences in degeneration, regeneration, and pathfinding abilities following each type of injury.

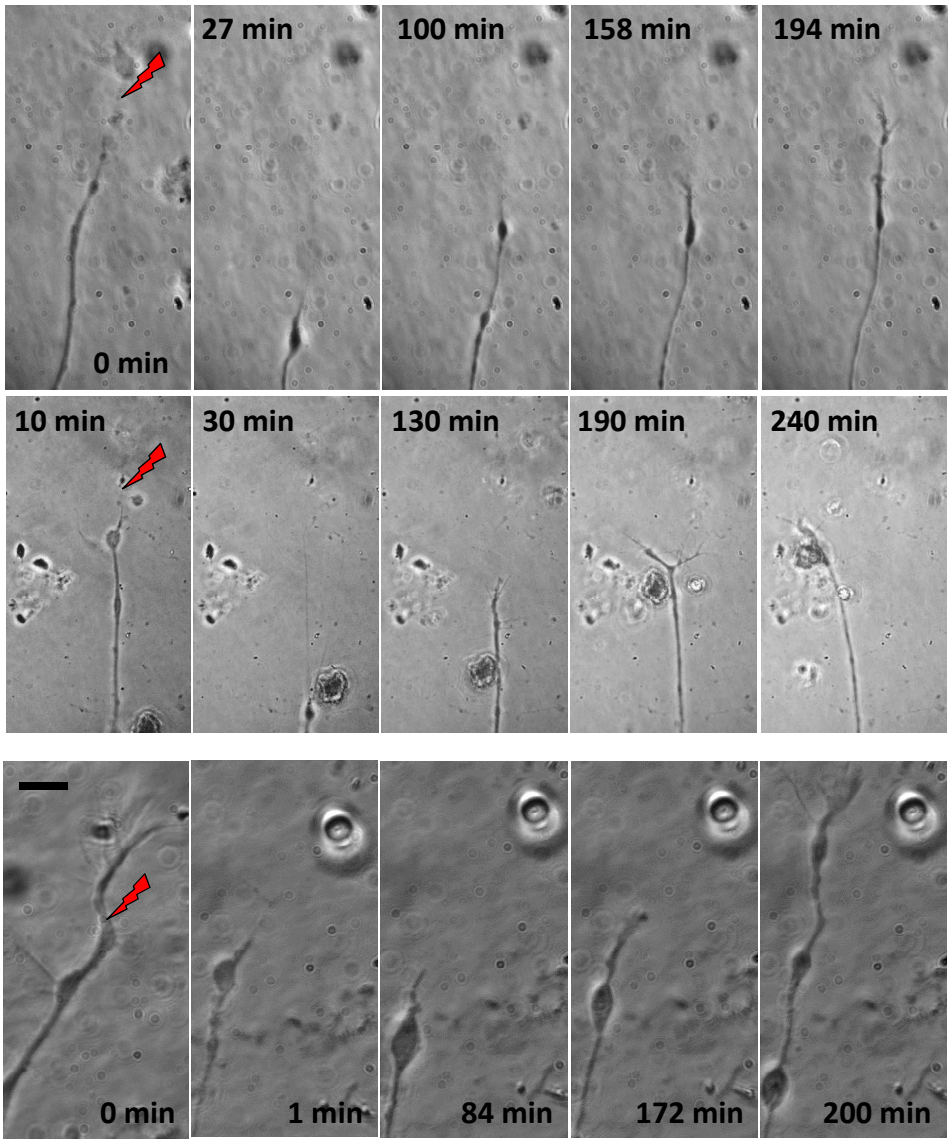

Figure 2-9 Time lapse images of characteristic axonal regeneration and pathfinding ability subsequent to (a) thin, (b) cut, and (c) burn injuries. Fs laser damage sites marked by red lightning bolt. Scale bars represent 6µm.

Degeneration rates were observed to increase with increasing degree of initial injury, while regeneration rates were observed to decrease with increasing degree of initial injury (Figure 2-10). Degeneration rates were 1.15, 0.83, and 3.73 μm/min for thin, cut, and burn injuries respectively. In the case of burn injuries, this increase in degeneration rate may be attributable to the formation of cavitation bubbles (Figure 2-9). This type of bubble formation may be residue of a shock wave, physically pushing the axon away from the damage site. Furthermore, a shock wave can disburse or destabilize local adhesion proteins and attachment site receptors, such as integrins. Integrins are known to mediate the attachment between axons and the extracellular matrix as well as axonal pathfinding during both developmental and regeneration stages. Integrins have also been implicated in axon fasciculation. The dispersion of these attachment and fasciculation mediating factors would lead to further detachment and disorientation of the damaged axon. Regeneration rates for thin, cut and burn experiments were found to be 0.40 ± 0.14, 0.47 ± 0.17, and 0.16 ± 0.11 μm/min.

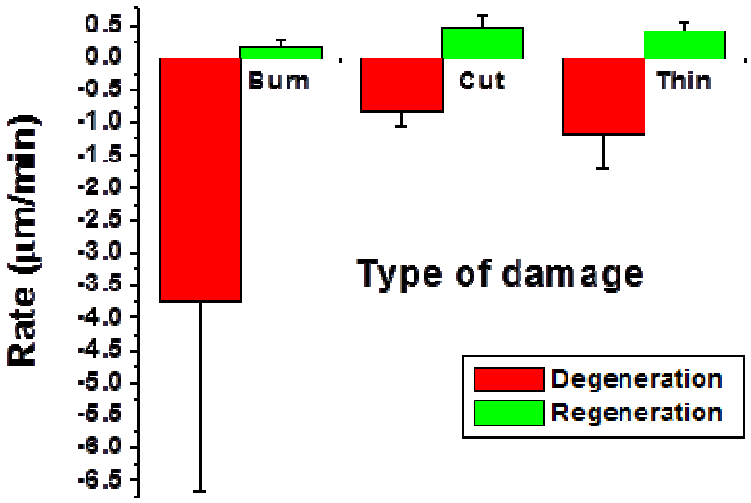

Figure 2-10 Degeneration and regeneration rates of primary RGC axons subsequent to burn, cut, and thin injuries.

The degeneration and regeneration paths were observed to differ from original outgrowth paths more significantly in the cases of cut and burn injuries, as compared to thinning. This has been quantitatively described in two ways; first, by calculating and comparing the average difference in directional growth cone orientation (relative angle) before injury and at the end of observation (Figure 2-11); secondly, by calculating the percentage of frames (images) in which the leading edge of the growth cone remained within ± 3µm of the original outgrowth path during both degeneration and regeneration (Figure 2-11). The average difference in directional growth cone orientation was found to be 15.07 ± 10.44, 20.23 ± 11.91, and 43.41 ± 5.61 degrees for thin, cut, and burn experiments

respectively. The percentage of frames in which the leading edge of the axon remained within ±3µm of the original outgrowth path was 85%, 68% and 59% for cut and burn experiments, respectively.

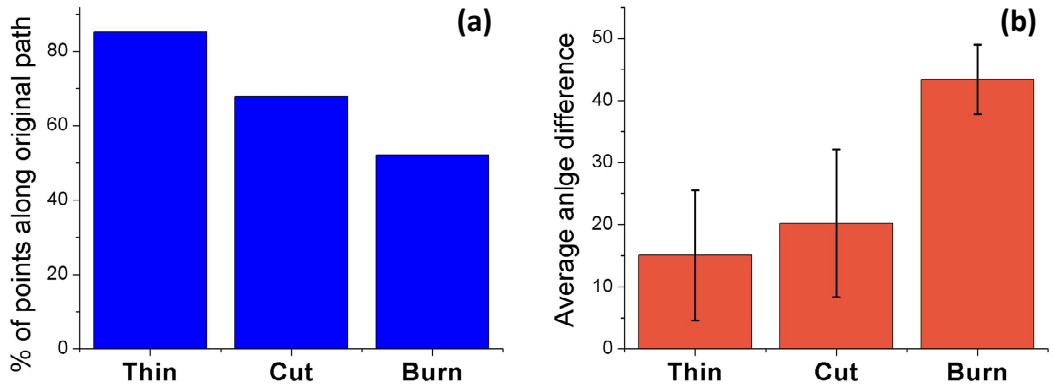

Figure 2-11 (a) Percentage of degeneration and regeneration points found within ±3µm of original path (prior to to injury). (b) Average angle difference between the initial and final orientation of the growth cone (prior to and subsequent to injury) for thin, cut,

Discussion

Understanding neuronal regeneration and pathfinding subsequent to injury is the primary step in developing therapies for brain stroke, trauma and spinal cord injuries. We have shown by fs laser axotomy (in vitro) that development and regeneration path differences are dependent on the severity of injury in the case of Goldfish retinal ganglion axons. Furthermore, this implies that degenerating axons may leave tracks for themselves to follow subsequent to injury and that these tracks result in a

high probability of pathfinding success unless ‘derailed’ by initial injury or subsequent chemical decomposition of the track.

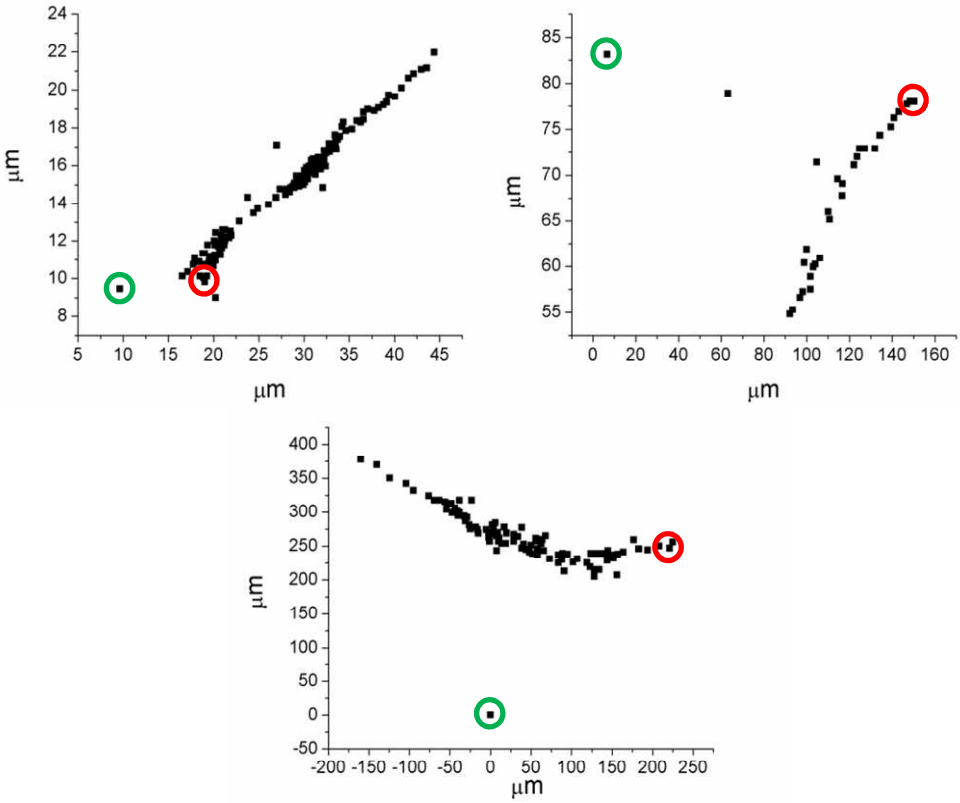

Figure 2-12 Characteristic time plots of leading-edge position of lamellipodia following fs laser induced (a) thin (b) cut, and (c) burn injury. Green circle indicates damage site (initial position) and red circle indicates final position of the lamellipodium’s leading edge.

Axons were shown to degenerate and regenerate different following varying degrees of initial injury. Varying degrees of initial injury produced significant differences in regeneration path as well as axon growth cone

orientation (points along original path and angle). Varying degrees of initial injury also produced varying rates of regeneration and degeneration, especially in the case of burn injuries. This may be due to integrin stability during regeneration growth cone pathfinding. Coupling of the cytoskeleton to the substratum is accomplished by specialized receptiors on the surface of the growth cone that recongnize and bind to specific molecules in the outside environment. These recpetors are indirectly linked to the actin cytoskeleton within the growth cone by cross-linking proteins. Receptors that provide this motility-enhancing function include integrins that recongnize extracellular matrix components like laminin, and cadherins. Along with integrins, N-cadherin has been shown to play an important role in axon growth and fasciculation. Cavitation bubble formation may have disbursed these stability and binding factors upon injury. Furthermore, while thin injury ultimately resulted in observed physical dissociation from the lamellipodium, there were initially tubular remnants observed along the path of degeneration. While the regenerating axon may have used these remnants as a mechanical ‘pre-laid track,’ it is also possible that chemical factors implicated in fasciculation (i.e. Nogo) may have remained present along with the remnants. Furthermore, cut and burn experiments may have resulted in the spillage of intracellular factors into the medium which could have affected the pathfinding ability of the regenerating axons. The

presence and concentration of these factors is, as of yet, unknown and further molecular biology experiments would need to be conducted to implicate or dismiss these factors in pathfinding subsequent to injury.

Chapter 3

Laser as an Axonal Guidance Cue

Introduction to Axon Growth and Guidance

Stochastic Axonal Outgrowth

An axon is the outgoing communication pathway of a neuron. It is a protrusion that extends outward, away from the cell body, with the purpose of creating a physically stable and functionally connected neural network in cooperation with other neurons. The common morphological analogy is to visualize the axon as your arm and hand. Your arm is the axon shaft, extending away from your body, containing an internal skeleton and circulatory system (cytoskeleton and microtubules), which serve as support structures for the skin (the plasma membrane), and transport pathways to your hand. Within the axon shaft, the cytoskeleton consists largely of parallel microtubules, bundled together, oriented with their 'positive' ends directed towards the growth cone. These bundled microtubules act as transportation tracks for the kinesin and other molecular motors, which actively carry membrane vesicles either retrograde (back toward the cell body), or anterograde (toward the growth cone).

You can think of your hand as the growth cone, which is a highly motile structure that is able to sense environmental cues and direct the

axon along paths that will result in a stable and functional neural network. The growth cone is tipped with finger-like protrusions, called filopodia. Filopodia are also highly motile sensing structures, which can react to the environment independently from the growth cone, and even independently of one another (86). As the growth cone crawls along within the developing or regenerating nervous system, it trails the axon shaft behind it. Thus, it is the growth cone that largely determines the final trajectory of an axon, although subsequent straightening or collateral branching can occur (your hand can only go where your arm can follow).

Growth cones undergo constant structural change. This morphological change is a result of the constant deconstruction and reconstruction of the internal actin network; a process which is sometimes referred to as the ‘actin treadmill.’ Unpolymerized g-actin (globular actin) diffuses outward into the peripheral regions of the growth cone and preferentially polymerizes near the cell membrane, where it becomes f-actin (filamentous actin). The polymerized actin network is then drawn toward the central region of the growth cone by myosin, where it undergoes depolymerization. It is this process, repeated over and again which is thought to generate traction between the axon membrane and a permissive substrate via adhesion molecules. When the actin-based tread gets a grip on the substratum, it can advance the leading edge of the

growth cone and draws it forward. An axon's growth is typically capricious, with periods of fast growth interrupted by periods of slow (or no) growth. The advancement behavior of the growth cone is modulated as it encounters stimuli in the environment. These changes in directional behavior (in vivo) often occur at what have been called "decision points," where growth cone chooses between alternate pathways (87).

An axon's advancement is not random, but highly biased by environmental guidance cues. These cues are primarily chemical in nature, but can also include force (fluid flow) and temperature gradients. Growth cones sense these environmental guidance cues and respond by growing selectively toward or away from them, depending on whether the guidance cue is attractive or repulsive. Calcium and cyclic nucleotides (cAMP and cGMP) have been highly implicated in this process, with the relative concentrations of these molecules within the growth cone effectively changing the polarization of the external guidance cue from attractive to repulsive or vice versa, along with the intracellular gradients of calcium ions. Furthermore, channels along the membrane can be chemically, mechanically, electrically, and thermally activated to allow for the influx of extracellular ions (ie calcium) into individual filopodia or localized regions of the growth cone. While axons in living organisms are known to have a broad distribution of growth directions and patterns, in

the absence of external asymmetric growth cues (either attractive or repellent), it has been shown, in vitro, that an axon's outgrowth will be more-or-less straight (88). In fact, once polymerized, the individual microtubule segments inside the axonal shaft have a Young's modulus "similar to Plexiglas and rigid plastics"(89), if they were uniform and isotropic.

The growth cone is also a highly polarized dynamical structure, and advances only at its leading edge. Its ability to make sharp turns (>90 degrees) is limited by this extreme polarization. Since there are often multiple guidance cues in the environment, often at very small gradients, integration and amplification of external signals are also fundamental functions of the growth cone. While peripheral nerves (axons) are known to regenerate subsequent to axotomy, mammalian CNS nerves do not regenerate in vivo. While this was once thought to be an intrinsic quality of CNS neurons, it has been shown that inhibitory environmental factors play a significant role in suppressing CNS nerve repair.

Laser-induced Repulsive Guidance of Primary Goldfish RGC Axons

Introduction

It is well known that axonal pathfinding (90, 91) is paramount to an organism's nervous system development (92, 93), and that, during this development, functional connections must be made across the entire

organism (94-96). Furthermore, in vivo nerve repair (e.g., following spinal cord injury (97)) requires not only the ability to regenerate damaged axons, but, most importantly, the ability to guide these regenerating axons along paths that will again result in functional connections. Basic studies in neuroscience and design of effective neuro-electronic interface devices (98) require the ability to construct in vitro neural circuitry (99). Therefore, the ability to effectively guide single axons is important to the understanding of basic, as well as clinical, problems. It has been shown that axonal growth rates and direction are primarily determined by environmental cues (100) which are ‘sensed’ by the axon’s filopodia. As discussed, these filopodia are finger-like growth cone extensions which sample the surroundings for attractive or repulsive growth and guidance cues, which may be mechanical, electrical, or chemical in nature. These cues can effectively induce or inhibit axonal growth (101) by affecting actin filament polymerization processes. If such gradients are asymmetrically positioned along the axonal growth axis, they result in growth cone turning and ultimately short-to-long-range axonal guidance. For example, activation of a filopodium’s calcium ion channels can result in an influx of extracellular calcium, which can lead to localized actin depolymerization, resulting in the arrestment of a filopodium’s growth, or even complete retraction into the axon’s lamellipodium (growth cone) (102). This has

been the basis for several axonal guidance (103) techniques introduced over the past two decades. It has been shown that chemical (104), topographical (105), electrical (106), and hybrid approaches such as electrochemical (107), optofluidic flow (108) and photo-chemical (109) methods can guide neuronal growth cones in vitro. However, these methods are either lacking in spatial and/or temporal specificity, and/or require the introduction of external factors. Therefore, the development of selective, minimally-invasive methods of axonal guidance is of considerable importance in the fields of neuroscience and neuroengineering.

To date, all purely optical methods (optical tweezers (110), asymmetric line tweezers (111), tapered optical fiber (112), and ultrafast laser microbeam (113, 114)) have been employed as an attractive axonal guidance cue. These methods use a focused laser beam operated in continuous wave (cw) or pulsed mode in order to utilize the intensity/force gradient or for microsurgery (108) (at the highest intensity region of the beam center). The guidance mechanisms in these cases rely on a tightly focused laser beam (high NA microscope objective with short working distance) impinging directly upon an individual growth cone. Here, we show that asymmetrical positioning of a laser beam in front of an advancing growth cone produces significant repulsive guidance. This

repulsive optical cue leads to highly efficient and long-range guidance of goldfish retinal ganglion cell (RGC) axons. We also theoretically explore the plausible mechanisms for the optical guidance effect and effectively rule out physical forcing or activation of stretch-sensitive ion channels. The presented method could allow efficient construction of *in vitro* neural circuitry for study of functional aspects of basic neuroscience and also paves the way for novel therapeutic strategies for controlled *in vivo* nerve regeneration.

Materials and Methods

Please see previous sections for detailed tissue extraction and cell culture methods.

The schematic of the imaging and microscopic manipulation platform for axonal navigation experiments is shown in Figure 2-4. Repulsive optical guidance of healthily advancing growth cones was achieved with a tunable Ti: Sapphire laser (MaiTai HP, Newport-SpectraPhysics) operated in mode-lock off condition to ensure cw-mode usage. The near-infrared laser beam was expanded and relayed via folding mirrors to the back-laser port of an inverted microscope (Ti-U Eclipse, Nikon). A mechanical shutter (Uniblitz) was used continuously throughout each experiment to pulse the laser beam (200 ms ON and 200 ms OFF) in order to avoid any possibility of continuous mechanical

forcing. A dichroic mirror was used to guide the beam to the back-aperture of a microscope objective (Nikon 1006, NA= 1.3). An IR cut-off filter was used in the imaging path for removing the reflected laser beam from the images collected by the EMCCD (Photometrics). For wavelength dependent experiments, the power of the laser beam was adjusted via the MaiTai control software and external polarizer so as to result in a sample-site beam power of 50-80 mW. In order to achieve repulsive optical guidance, the laser beam spot was asymmetrically positioned in the (forward) path of the advancing axons and left static for the duration of the experiment unless otherwise noted. All image sequences were collected and processed using ImageJ software (NIH). In order to determine the turning angle, ImageJ's angle tool was used, with the vertex for each measurement kept approximately 5 mm from the leading edge of the advancing growth cone. Growth rates and distances determined by tracing from a fixed arbitrary point along the axon shaft to the distal end of the advancing growth cone. Axons which did not advance beyond the static position of the laser spot during guidance trials were omitted from statistical comparison with negative controls.

Results

For optical guidance of axons, in vitro experiments were conducted on goldfish RGC axons emerging from retina explants in petridish. Figure

2-4 shows the schematic for our imaging and optical manipulation platform used in all axonal guidance experiments. The laser beam spot, acting as a repulsive cue, was asymmetrically positioned in front of randomly-selected, advancing axons. Unless otherwise indicated, the laser spot was not repositioned during the course of the experiment. The axons could be selectively turned either ‘‘right’’ or ‘‘left,’’ with turning direction determined by left/right asymmetric placement of the static laser spot. Figure 3-1 (a) shows the laser spot (average laser power: 50 mW, 25 Hz), placed in the right-forward position of an advancing growth cone. The axon was observed to turn left (away from the laser spot) by more than 40 degrees (Figure 3-1 a to b). Axons could also be turned to the right (Figure 3-1 c to d) as a consequence of placing the laser spot in the left-forward position with respect to the advancing growth cone. In all cases, the axonal shaft was found to eventually realign itself along this new growth cone direction. This may be attributed to the fact that the flexural rigidity (115) of microtubule bundles (2×10^{-23} Nm^2), located within axonal shafts, is high enough not to allow sharp turns (> 15 degrees) over relatively short periods of time (< 1 hr). Furthermore, the dynamics of actin-based motility prefer growth along relaxed, straight paths, as opposed to stressed turns. All phantom-spot (no laser) trials resulted in the growth cone passing through, or very near to, the phantom laser spot, with negligible growth

cone turning (5.6 ± 6.3 degrees, 20 min trials, n= 8). Comparison of axon migration paths subject to optical guidance and phantom laser spot trials using a one-tailed t-test yields a pvalue of 2.7E-5. The turns achieved by repulsive optical guidance are statistically significant.

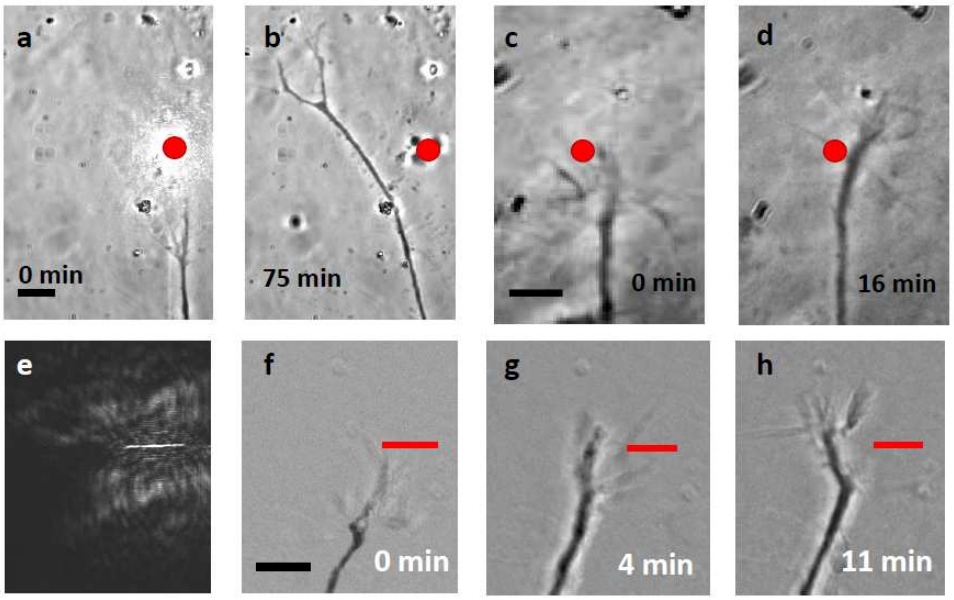

Figure 3-1 Optically controlled axonal guidance. Left-turning event before (a) and after (b). Right-turn before (c) and after (d). Static laser spot position is indicated by the red dot. Spatially-sculpted light for optical guidance: (e) line-spot profile, (f-h) Time-lapse images of axonal guidance using spatially-sculpted line beam profile (marked as red line). Scale bars represent 10 μm. [Figure 1 from (4)]

The efficiency of our optical guidance method is found to be 100% (n =21). For efficacy measurements, we define a complete axonal

guidance trial as an experiment during which the axon's growth cone ultimately extended beyond the static position of the laser spot. Axons which were not observed to advance beyond the position of the static laser spot were omitted from statistical analysis. We reiterate that no growth cones were found to successfully advance through the laser spot with the abovementioned laser parameters. It may be noted that the irradiation schedule in earlier cw laser based attractive-cue based guidance methods (scanning, defocused or spatially-sculpted optical tweezers) rely on the laser spot impinging on the growth cone itself. Here, in contrast to direct irradiation, the laser spot is placed asymmetrically ahead of the actively growing growth cone (Figure 3-1 (a-d)), and serves as a highly-effective repulsive cue.

Spatially Sculpted Axonal Guidance

In some cases (n= 2), during single spot-illumination based optical guidance, the leading asymmetric placement did not correlate to oppositely directed guidance due to initial growth cone retraction from the laser spot. Following retraction, the growth cone was observed to ‘‘feel out’’ all new available paths before again advancing with a defined direction, sometimes generating the unexpected turning direction. However, this effect could be corrected in the future by alternative beam profiles, multiple laser spots, or dynamic control of the laser spot. In order

to better define the guidance path, a line beam profile (Figure 3-1 (e)) was generated by a cylindrical lens, which could be rotated to define the orientation of the profile. Axonal guidance using the line beam profile is shown in Figure 3-1 (f to h) achieved using a 785 nm laser beam. Since the laser power is distributed over a relatively large spatial scale (5 mm), higher laser power (200 mW) was used for these experiments. It is worth noting that a spatial light modulator (SLM) can be used to define more complex paths for the migrating axons. With timesharing scanning laser beams, lower power levels can be used to create similar effects.

Kinetics of Laser-assisted Axon Turning

For determining the efficacy of optical beam in axonal guidance over a period of time, we tracked a length of the axonal shaft (starting from growth cone toward soma) and overlaid the tracks as illustrated in Figure 3-2 (a). Figure 3-2 (b) shows overlay of time-lapse images of axonal shaft turning toward left due to right-positioning of the laser spot. The kinetics of axonal left-turning angle is shown in Figure 3-2 (c). As shown, the turning process is faster during the initiation phase (5–10 min), which saturates after approximately 15 min. This behavior is quite similar to that observed during right-turning of axons. Figure 3-2 (d) shows a cumulative distribution plot for final growth cone turning angles. The majority (8 out of 10) of experiments resulted in growth cone turning angles equal or greater

to 42 degrees, while the remaining (2 out of 10) axons turned 22 degrees in response to laser spot. The cumulative distribution of turning in both left and right directions is shown in Figure 3-2 (d). Advancing growth cones were turned by an average of 51.2 ± 14.2 degrees from their initial paths by single laser spot based optical guidance. Prior to laser spot interaction, the observed growth rate was 0.74 ± 0.84 mm/min, well within the range observed in earlier studies (114, 116). After the growth cone had turned and was no longer interacting with the laser spot, the observed growth rate was measured to be 0.79 ± 0.98 mm/min, implying that the guidance event does not cause extensive or irreparable damage to the axon. Growth kinetics of a typical axon is shown in Figure 3-2 (c). This further implies that this purely optical guidance method is not a permanently damaging event and can be used for guidance and delivery of healthy axons. Additionally, the fact that axonal shafts realign themselves along the direction of turn indicate that the induced turn is a permanent event, though we believe that it would be reversible.

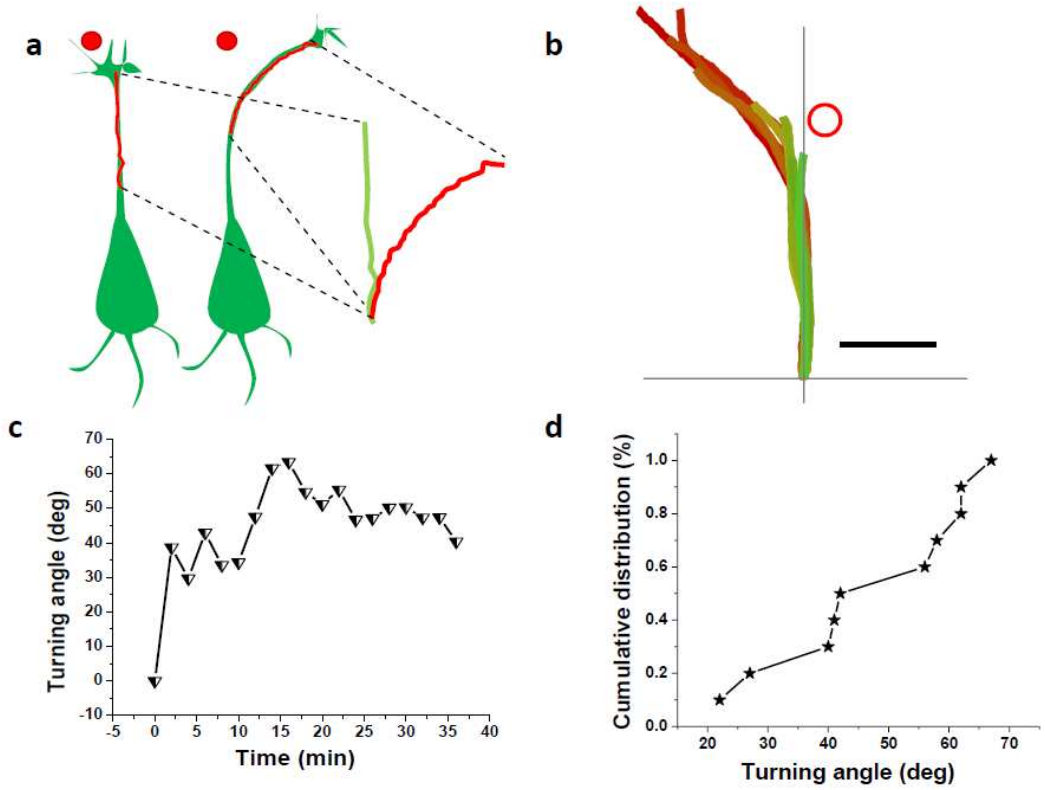

Figure 3-2 (a) Illustration of the method employed for determining efficacy of optical guidance. Laser spot position (red circle). (b) Overlay of time-lapse images of axonal shaft turning towards left. Laser spot position is indicated by red circle. Scale bar represents 5 μm. (c) Kinetics of axonal left-turning angle. (d) Cumulative percentage plots for the distribution of final axon turning angles. [Figure 2 from (4)]

Long Range Optical Guidance of Goldfish RGC Axons

Long-range (both angle and relative distance) axonal guidance could be realized by effecting multi-staged turns. By dynamically

repositioning the laser spot in front of an already deviated axonal growth cone path, multi-stage optical guidance events were observed to produce an overall turning angle of up to 120 degrees and total guidance distance of ~90 μm (Figure 3-3 a to c). Following 50 min of laser spot interaction (turning angle of 55degrees), the laser spot was repositioned, as shown in Figure 3-3 (b). Figure 3-3 (d) shows the kinetics of axon's turning-angle during this multi-stage axonal turning process. The growth rate was found to be low during the initial phase (10 min) of interaction, but was observed to increase after 20 min (once the growth cone had turned completely). Figure 3-3 (e) shows the correlation histogram for growth rates and turning angle rates at different time points. From this single multi-stage guidance experiment, no obvious correlation between growth and turning rates can be determined.

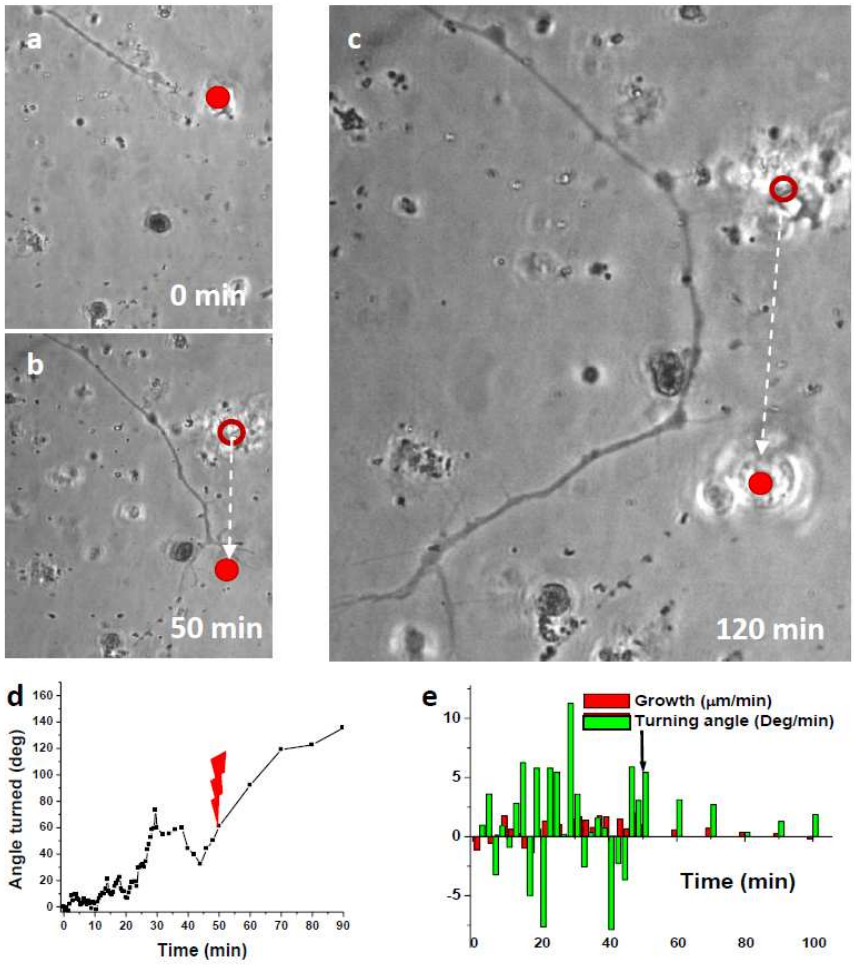

Figure 3-3 (a-c) Time-lapse images of temporally modulated optical guidance cue. Filled and hollow red circle indicates final and former laser spot position. (d) Kinetics of axonal turning during multi-stage axon turning. Lightning bolt indicates time at which laser spot was repositioned. (e) Correlation of outgrowth and turning. Black arrow indicates time at which laser spot was repositioned. [Figure 3 from (4)]

Proposed Mechanisms of Axonal Guidance

The mechanism of repulsive guidance of axon due to laser can be analyzed based on three plausible effects, namely photo-physical, photo-thermal effects (leading to indirect chemical changes) or direct photo-chemical changes which occur during filopodia-laser spot interaction. First, a laser microbeam of Gaussian (or similar) cross-sectional intensity profile is known to act as a force gradient, which attracts or pulls objects toward the center of the beam (117). Stretch-activated (or mechano-sensitive) ion channels are present in virtually all cells (118). They serve as a primary mechanical transducer, with the channel's state changing as an immediate effect of mechanical force pressure, or pull (119). Therefore, any sufficient mechanical force gradient could activate these mechanosensitive channels, resulting in an influx of calcium and other ions present in extracellular media. An influx of extracellular calcium is known (120) to lead to local depolymerization of axonal filopodia/growth cone and, ultimately, the arrestment of the filopodia's growth (or retraction into the growth cone). To evaluate the effect of radiation pressure forces (121) due to laser spot, simulation of the gradient force acting on single filopodia was carried out.

The filopodium (radius: a, length: l) in the instantaneous electric field of acts as a dielectric right-circular cylinder, whose dipole moment in MKS units is given by

$$\vec{p}(\vec{r},t) = 2\pi n_2^2 \varepsilon_0 a^2 l \left(\frac{m^2 - 1}{m^2 + 1} \right) \vec{E}(\vec{r},t) \tag{21}$$

where m = n1/n2 is the relative refractive index of the filopodium and

$$2\pi n_2^2 \varepsilon_0 a^2 l \left(\frac{m^2 - 1}{m^2 + 1} \right) \tag{22}$$

is the so-called polarizability of a right circular cylinder, assuming that the orientation of the electric field is perpendicular to the axial direction of the cylinder. There are no closed-form solutions for a dielectric right circular cylinder without this assumption, and the problem must either be solved numerically since circular cylinders are objects with uniaxially anisotropic polarizability.

The gradient force is due to the Lorentz force acting on the dipole, which is induced by the electromagnetic field. By using the electric dipole moment, an instantaneous gradient force can be described as

$$F_{grad}(r,t) = [\vec{p}(r,t) \cdot \nabla] \vec{E}(r,t) \tag{23}$$

Therefore,

$$\vec{F}_{grad}(\vec{r},t) = 2\pi n_2^2 \varepsilon_0 a^2 l \left(\frac{m^2-1}{m^2+1}\right)\frac{1}{2}\vec{E}^2(\vec{r},t) \tag{24}$$

The gradient force which the filopodium experiences in a steady state is the time-average version and is given by

$$\vec{F}_{grad} = \frac{\pi n_2 a^2 l}{c}\left(\frac{m^2-1}{m^2+1}\right)\nabla I(r) \tag{25}$$

By substitution, the component of the gradient force which acts along the axis of the cylinder is found to be

$$F_{grad,x}(r) = -\hat{x}\frac{\pi n_2 a^2 l}{c}\left(\frac{m^2-1}{m^2+1}\right)\left(\frac{4\tilde{x}/W_0}{1+(2\tilde{z})^2}\right) \tag{26}$$

Figure 3-4 shows the transverse force acting on a single filopdium for 50, 80, and 110 mW sample site power at 785 nm. Figure 3-5 shows transverse force distribution for 80 mW sample site power at 690, 785, and 1040 nm respectively.

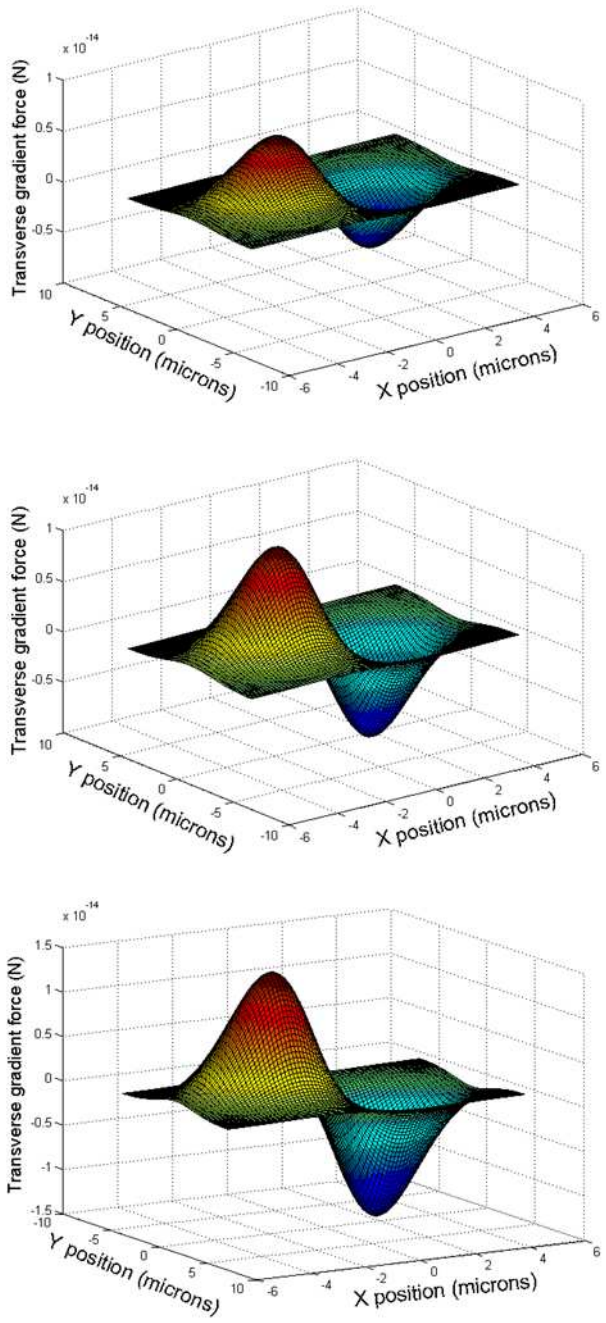

Figure 3-4 Transverse gradient force distribution due to a focused (1.3 NA) 785nm laser at 50, 80, and 110 mW sample site power.

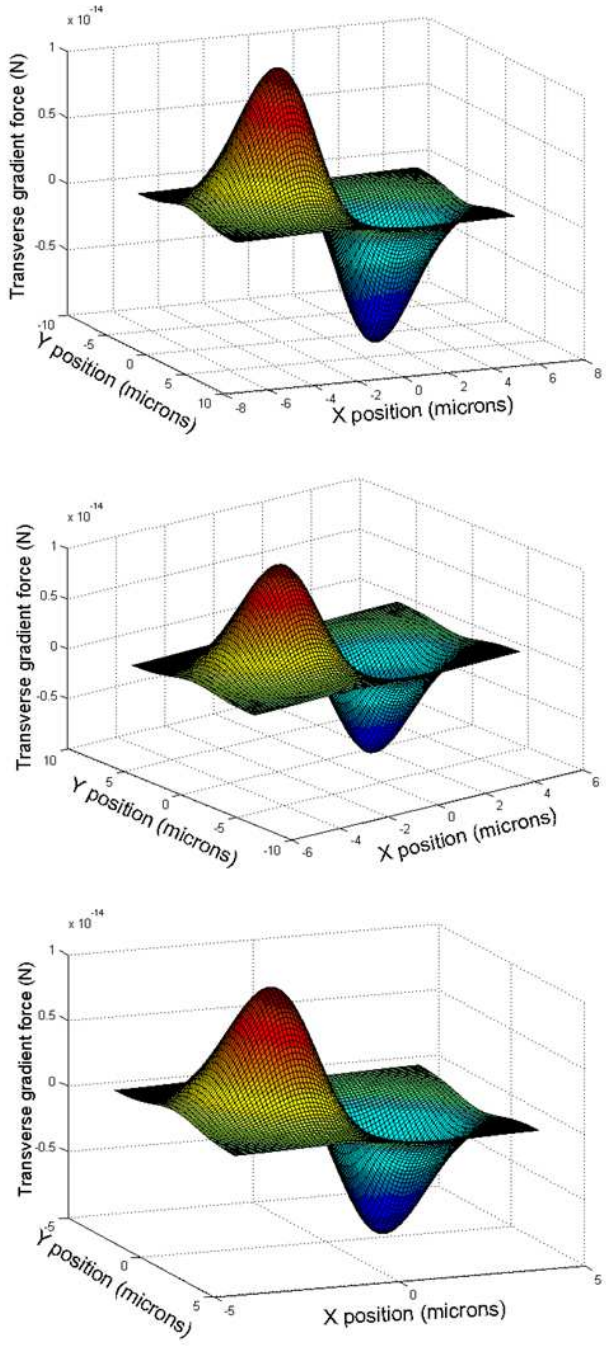

Figure 3-5 Transverse gradient force distribution due to a focused laser spot (1.3 NA) for 80 mW sample site power at 690, 785, and 1040 nm.

These forces are expected to vary with laser power and interaction volume (length) of the filopodium with the laser spot. However, beyond a certain threshold (30 mW), increase in laser power did not lead to any significant increase in turning angle or efficiency. Furthermore, axons would later be guided with weakly focused (20x, 0.5 NA) laser beams, which would result in substantially lower transverse gradient forces. Most importantly, we have observed repulsive guidance events with laser positioned as far as 20 μm from the growth cone's leading edge. Unless the laser spot was interacting with filopodia in a plane other than the imaging plane, we must accept that this field-effect acts at a distance. Therefore, the role of photo-physical forces in the repulsive optical guidance of axons can be neglected.

Laser-induced Repulsive Guidance of Primary E18 Rat Cortical Axons

As discussed in the previous section, the functional neural circuitry formation requires highly accurate axonal pathfinding during neural development or regeneration. The direction of axonal outgrowth is dictated by the detection and integration of competing guidance cues found in the surrounding environment. These guidance cues can be chemical, physical, electrical, or optical in nature (including any combination thereof). They are primarily detected by the axon's splayed distal end, called the growth cone, where the membrane expresses a wide variety of

dense, specialized receptors. When a guidance cue gradient is applied across the growth cone, membrane receptors closer to the source of the gradient will have a higher probability of activation, dependent in large part on the recruitment or modulation of secondary messenger concentrations. Over time, the axon's growth becomes polarized toward or away from the source of the gradient, depending on whether the guidance cue is attractive or repulsive.

One important secondary messenger is calcium (Ca^{2+}). Intracellular Ca^{2+} levels have long been known to play an important role in axonal growth and guidance (122), as well as being implicated in central nervous system neuronal migration (123, 124). Intracellular Ca^{2+} flux can be the result of internal Ca^{2+} stores being released from the cell's endoplasmic reticulum, or the result of extracellular Ca^{2+} influx, triggered by the opening of cation-permeable membrane channels, such as transient receptor potential (TRP) channels (125). Only a narrow range of global intracellular Ca^{2+} concentration is optimal for growth cone extension. Higher or lower intracellular concentrations slow growth cone extension, or even cause retraction and growth cone collapse. Therefore, whether a guidance cue is attractive or repulsive is largely dependent on the local intracellular Ca^{2+} gradient the guidance cue evokes. Under normal conditions, a steep intracellular Ca^{2+} gradient resulting from a

guidance cue gradient is likely to result in attraction, whereas a shallow intracellular calcium gradient is likely to result in repulsion (126, 127). Blocking Ca2+ influx by inhibiting the normal function of membrane cation channels or changing the extracellular calcium concentration baseline has been shown to abolish the guidance response (126). These modulations may also lead a ‘normally’ repulsive guidance cue to become an attractive one, or vice versa. As calcium is known to play significant roles in both outgrowth and guidance, there has been an enormous effort to determine the primary ways intracellular calcium concentrations are regulated by the cell. Many specific calcium ion channels are known, but there are also non-specific cation channels known to play important roles in the mediation of environmental cues by modulating cation (including calcium) levels.

Transient receptor potential vanilloid (TRPV) channels are a sub-family of TRP proteins, which form polymodal, non-selective cation channels on the membranes of specific cells. These channels are known to open in response to capsaicin, low pH, protons, various lipids, and, in some cases (TRPV1-4), heat. High expression levels of TRPV channels are found in sensory neurons, where they are primarily responsible for mammalian temperature sensation. However, TRPV1-4 are also expressed in the central nervous system, with TRPV1-3 being expressed

in the cortical regions of mammalian brains. TRPV1, arguably the most extensively studied among the TRPV subfamily, is often cited as having an activation temperature of 40-43 ℃ (128-133). Ho wever, several research groups have shown TRPV1 activation to occur at lower, more physiologically relevant temperatures (35-39 ℃) (1 34, 135). In recent years, the TRPV subfamily has been frequently implicated in axonal guidance events, either as the primary mechanism, or as a mediator for downstream molecular cues.

The ability to guide primary axons by purely optical means is an attractive prospect due to light's potential for high spatial and temporal selectivity, its absolute sterility, and for its low-level invasiveness at near infrared (NIR) frequencies. In 2002, this potential was realized by Ehrlicher et al. when they described a novel, purely-optical attractive guidance cue which exploited the optical forces due to a focused laser beam, asymmetrically impinging upon the leading edge of a PC12 neuronal growth cone (136). Since that time, there have been several variants of the attractive optical guidance cue, which include studies of various beam profiles (111, 137), wavelengths (138), tapered optical fibers (112), and the demonstration of the general method in three-dimensional environments (139). Studies of light as an indirect guidance cue have also been undertaken, where focused lasers have been used to induce

photolysis, asymmetrically releasing calcium (140) near the growth cone, and in which circularly polarized light has been used to trap and rotate birefringent particles, steering nearby growth cones by microfluidic flow (35).

Although direct optical guidance methods have been demonstrated for more than a decade, the proposed mechanisms by which light can directly influence the steering of axonal growth cones have never been fully understood or developed. These proposed mechanisms include optical forces acting on intracellular components such as globular actin monomers, optical forces orienting and stabilizing existing filopodia, and temperature rise. For the most part, temperature rise has been disregarded as a probable primary mechanism for attractive axonal guidance since the temperature increase due to culture medium, cellular membrane, and intracellular component absorption would be relatively small when using NIR light sources. Nevertheless, as we have previously reported, a focused NIR laser spot, asymmetrically positioned in front of advancing primary E18 rat cortical axons, has effectively served as a repulsive guidance cue. Since the laser spot is not directly impinging upon the growth cone, we must conclude that a laser-induced, diffusive field is responsible for the repulsive guidance effect.

Materials and Methods

Optical guidance experiments were performed using isolated cortical neurons from embryonic 18 day rat embryos. All procedures were conducted according to IACUC approved protocol. The cortical tissues were dissected, cleaned (meningeal layer), and enzymatically dissociated (0.125% trypsin in L-15 medium) for 20 min at 37℃. The dissociated cortical neurons (100,000/device) were seeded on Poly-D-lysine (0.01%, Sigma) precoated coverglass with Polydimethylsiloxane barrier (Sylgard 184, Dow corning), and the serum-free culture medium (Neurobasal, supplemented B-27 with BDNF and NT-3, 10 ng⁄ml) was changed every three days. A tunable NIR Ti: Sapphire laser (MaiTai HP, Newport-SpectraPhysics), operated in cw condition, was expanded and relayed via folding mirrors to the back laser port of an inverted microscope (Ti-U Eclipse, Nikon). A dichroic mirror was used to guide the beam to the back aperture of either a 20x (Ph1, 0.5 NA) or a 100X microscope objective (Ph3, 1.3 NA, Nikon). In the case of RCN experiments, no external shutter was used, as we had effectively ruled out direct mechanical forcing and if the effect was due to a temperature field, we wanted the temperature rise to reach its steady-state condition and not be in constant flux. An IR cutoff filter was used to remove the back-reflected laser beam from reaching the CCD (Photometrics). The power of the laser beam was adjusted so as to

result in a sample-site average beam power of 50-80 mW. The laser power at the sample plane was calculated by multiplying the transmission factor of the objective with the power measured at the back aperture of the microscope objective using a standard light power meter (PM 100D, Thorlabs). To achieve optical guidance, the beam was placed ~5 μm away from the axons' filopodia, asymmetrically positioned in the forward path of the advancing growth cone.

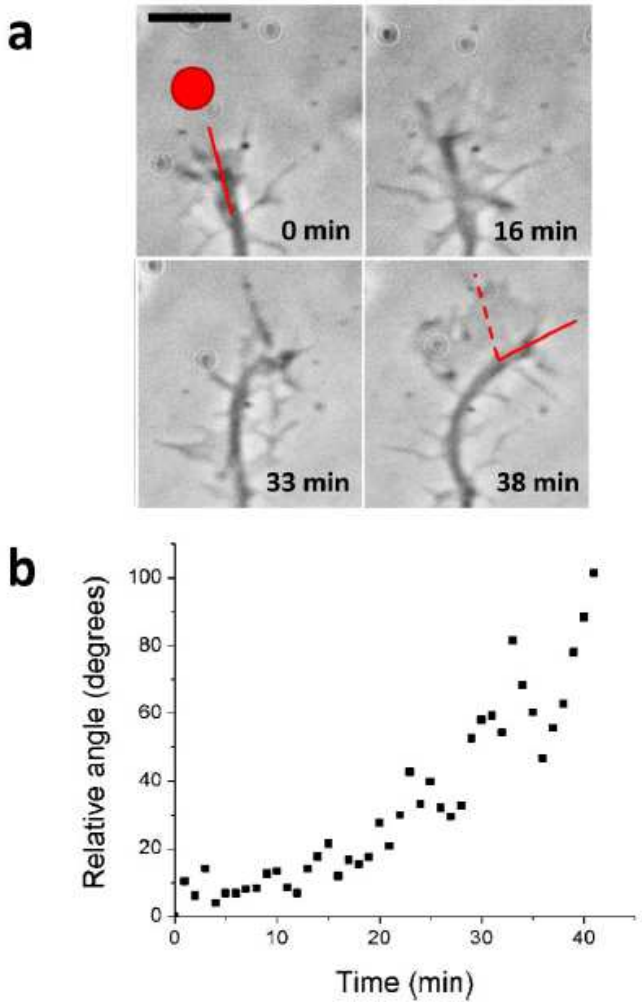

Figure 3-6 (a) Time-lapse images showing optical guidance of RCN axon. (b) Kinetics of turning angle as function of time during single guidance event. Scale bar: 10 μm. [Figure 2 from (1)]

Single stage trials

The laser-assisted navigation of rat cortical neurons (RCNs) is shown in Figure 3-6. The axonal terminal (growth cone) turned continuously toward the right from the initial growth cone direction (shown by vertical arrow) after switching on the laser beam. The image of a typical axon before and after the turn is shown in Figure 3-6. The laser spot position is marked by a red circle. The guidance efficacy of the laser-induced guidance cue was found to be 100% for the RCN axons while using 80 mW sample-site time-averaged laser power at 785 nm. In Figure 3-6 (a), we show the time-lapse images of an optically guided RCN axon when laser beam is applied at 0 min. The corresponding kinetics of turning angle is shown in Figure 3-6 (b). The kinetics of turning angle was found to be somewhat nonlinear in nature. As shown in the kinetics graph (Figure 3-6 (b)) the axonal terminal (growth cone) takes ~10 min before it starts to turn. This lag period can be attributed to the time required for the growth cone to become polarized in the new direction. In this particular case, the turning angle reached ~100° 40 min after application of the laser beam. The average turning angle for RCN was found to be 55.3 ± 12.7 degrees (n=4). The mechanism of such axonal guidance due to a cw NIR laser beam at a distance was proposed, at this point, to be photothermal in nature.

Since the laser spot does not overlap with the growth cone or filopodia, photomechanical effects or direct photochemical interaction of filopodia with laser spot can be ruled out as plausible mechanism for the observed repulsive guidance of the RCN axons. Pulling of filopodia directly by optical tweezers led to retraction of axons rather than guidance in all trials (n=12). In order to evaluate if there is any effect of the repulsive optical cue on growth, the relative length of the RCN axon was monitored as a function of time. The linear nature of the growth kinetics (after initial lag period of ~10 min) implies that RCN axonal growth is not inhibited by the optically induced turning process. The post-turning growth rates of RCN axons were recovered to the control values, as measured prior to optical guidance. In contrast, irradiation of RCN growth cones with an intense tweezers beam led to their damage and retraction in ~95% of cases (17 out of 18), failing to effectively guide them. While 785 nm data was presented here, the RCN axons were also found to be guided by a range of wavelengths in the NIR regime (700–1000 nm).

Since the estimated temperature rise of the cell medium is an order of magnitude different from 700 nm (<0.1℃) to 1000 nm (~1°C) at same laser power (80 mW), our findings suggest that axons can sense very low temperature rises (gradients) at a distance when applied asymmetrically to the growth cone, but no such effect is observed for an overall uniformly

distributed temperature rise. I will discuss later the threshold laser powers at specific wavelengths that result in turning events. Determination of threshold excitation intensities may enable the use of low power lasers and LEDs to be used for effective volumetric (3D) axonal guidance. In response to low power (0.5 mW) cw blue (473 nm) and green (532 nm) laser beams, the axons were observed to grow into the laser spot, and unlike NIR laser trials, the growth cones were often damaged (formation of blebs) and could not be effectively guided.

Loop formation and prevention

Self-avoidance (141, 142) is a key mechanism in synaptogenesis regulation, and allows neuronal processes to avoid self-fasciculation and loop formation. Remarkably, some self-avoiding neurons discriminate self from non-self and interact freely with other neurons of the same subtype, but not with itself. This is especially important during development (143, 144), when long-range projections span different regions of the nervous system. Axonal pathfinding within the brain as well as in the peripheral nervous system is also crucial for in vivo restoration of function subsequent to damage and regeneration. An inability of axons to find their correct paths leads to abnormalities within circuit formations, and thus leads to nervous system dysfunction. Such defects are believed to be primarily biochemical or genetic (145, 146) in origin, and are related to

birth defects such as autism (147), tuberous sclerosis complex (148) and retinal dysplasias (149). Furthermore, in chemically-treated retinas, axons have been shown to exhibit highly abnormal courses, including circular routes and hairpin loops. However, it is not known if a normal healthy axon would like to fasciculate over itself under the influence of external physical obstructions or physico-chemical cues. This scenario is highly physiological in many cases such as the narrow physical dimension of the exit point (blind spot) in retinas, where the optic nerve leaves the eye. Since earlier attempts have relied on confinement and guidance of axons by physical (150) channels or chemical cues (151), there has not been the required spatial and/or temporal resolution to allow formation of small loops in single axons. It is therefore unclear if a physical or chemical obstruction to a healthy, normal axon would just turn the axon away from its original path or if it can actually lead to self-fasciculation and loop-formation. Here, we have utilized a weakly-focused NIR laser beam to guide rat cortical axons in a highly effective manner, which allowed us to construct loops of varying radii and observe axonal self-fasciculation for the first time.

While the effectiveness of our optical guidance method at the currently reported parameters has been 100% for single-turn events (n = 7) of rat cortical axons, we wanted to see whether or not multi-staged

guidance events could repeatedly turn the growth cone and go one step beyond the successes achieved in the case of retinal ganglion cells, and construct a full axonal loop. However, we first wanted to examine whether or not such loops are randomly formed in a normal physiological in vitro environment from healthy neurons extracted from the cortical regions of wild-type rats. Though, to date, only genetic and biochemical alterations have been thought to result in aberrant axonal guidance and loop formation, to our surprise, we found random rat cortical neuron loop-formations in the culture platform, albeit at rare incidences (4 out of 102 axonal terminals inspected in 25 random fields of views). Such loops were found to have a radius of curvature ranging from 6 to 22 μm (Figure 3-11). This observation led us to conclude that without any physical obstruction, a small, but non-negligible percentage (3.9%) of axons may form such loops in normal in vitro conditions if they are unable to find a suitable connection site within 2-9 days. This activity may not necessarily imply an aberrant process, as it could be an effective way by which neurons regulate undesirable synapse formation and optimize their connectivity. However, in order to ascertain that a loop can be formed at any selected point in space and time, we selected random advancing axons (Figure 3-7 (a)).

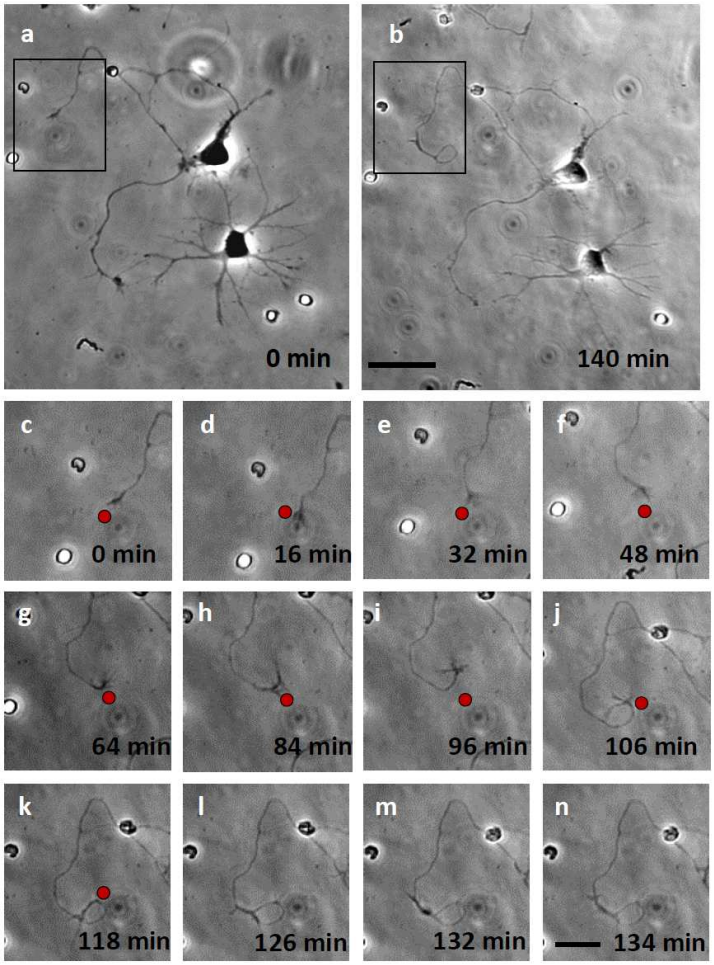

Figure 3-7 Laser-induced axon loop-fabrication and self-fasciculation. (a) Phase-contrast images (a) before and (b) after guidance. Black rectangle indicates guidance region of interest. Scale bar: 50 µm. (c-k) Time-lapse images of optically-fabricated axonal loop (laser spot shown as red circle). (l-n) Self-fasciculation of the axon. Scale bar: 20 µm.

Figure 3-7 (b) (region of interest marked by rectangle) shows an optically-guided O-loop, which was fabricated from a primary rat cortical

neuron. In Figure 3-7 (c to k), we show time-lapse zoomed images demonstrating construction of the optically-fabricated axonal loop by a dynamically-repositioned laser spot (marked by red circle, 60 mW, 785 nm).

Formation of the loop (Figure 3-7) demonstrates the unprecedented ability of this repulsive optical cue method to achieve full-circle guidance without any topographical boundaries, which should enable in situ formation of complex neuronal circuitry. Interestingly, the radius of curvature of the loop formed by this method can be seen to be ~5 µm roughly the same radius as the smallest radius of curvature found in naturally occurring loops (Figure 3-8 (A)). After optically-guided loop formation (Figure 3-7 (k)), though we hypothesized that the GC would advance across the original axonal shaft, the optically-guided rat cortical axon continued to grow along itself, with self-fasciculation observed over long distances and time (Figure 3-7 (i-n)). This leads us to believe that the self-avoidance hypothesis may not be universal for all types of axons and specific neurons may use it to their advantage for forming fascicles with themselves, thus down-regulating synaptogenesis.

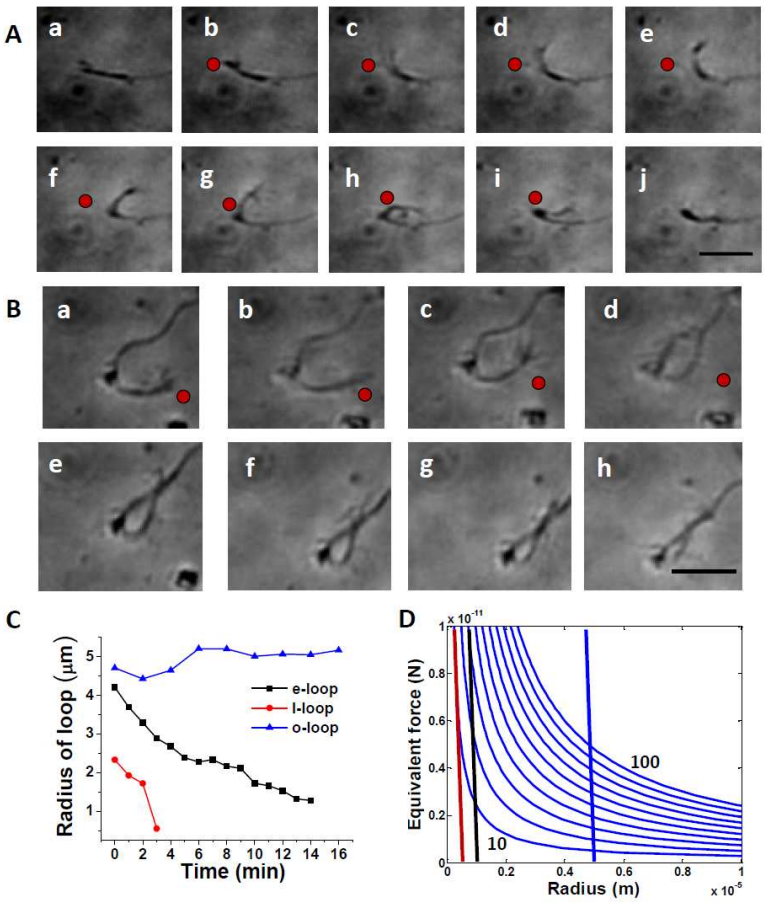

Figure 3-8 Laser- assisted fabrication of loops of varying radii. (A) “I-loop” formation (a-j, 3 min frames). Scale bar: 10 µm. (B) “e-loop” (a-d, 4 min frames). (e-h) Self-fasciculation and decrease in radius of fabricated loop. Scale bar: 10 µm. Red circles denote laser spot positions. (C) Kinetics of loop diameter for 3 trials. (D) Radius vs equivalent force for axons with different number of microtubules (10-100 in steps of 10). Vertical lines indicate three achieved radii of axonal loops.

In order to evaluate if the turning angle kinetics are modulated by repeated guidance events, we carried out analysis of turning rates for seven consecutive guidance events. Figure 3-9 (a) shows turning angle kinetics of laser-guided rat cortical axon achieved consecutively using a weakly-focused laser beam by a 20X microscope objective. No unidirectional trend between turning rate and sequence number was observed implying that the axon did not lose its ability to turn in response to the repeated repulsive light-cue. Though, for the example shown in Figure 3-9 (a), it appears that the last trial led to the highest turning rate, it is rather random and not the case for all trials. A cumulative plot for the distribution of laser-guided axonal turning angles is shown in Figure 3-9 (b). It may be noted that in case of axonal stretching, the formation of small bends in an axonal shaft leads to degeneration. For determining the effect of multiple guidance events (during loop formation) on health of axon, net axonal growth as a function of time during optical guidance is measured and shown in Figure 3-9 (c). The growth rate (slope of Figure 3-9 (c)) during the (2 hr) multi-stage turning by spatio-temporally modulated laser beam is found to be linear. Remarkably, formation of small axonal loops did not hinder the GC in its growth, as one would have expected due to strain on the intra-cellular microtubule bundles. The instantaneous growth rate (Figure 3-9 (d)) depicts the dynamic nature of

the small-time scale fluctuations in the axonal growth rate, which is expected due to axons' well-documented stochastic growth behavior. In order to evaluate if spatially-sculpted laser beams can be used to guide axons via repulsive-cue over a relatively large distance, a line profile (10 μm) was created by use of a cylindrical lens in the laser beam (200 mW) path. Figure 3-9 (e) shows the time-lapse (3 min) images of axonal guidance using the line spot (marked as red line). The axon was found to migrate with the same avoidance mechanism as shown for circularly-symmetric spot irradiation.

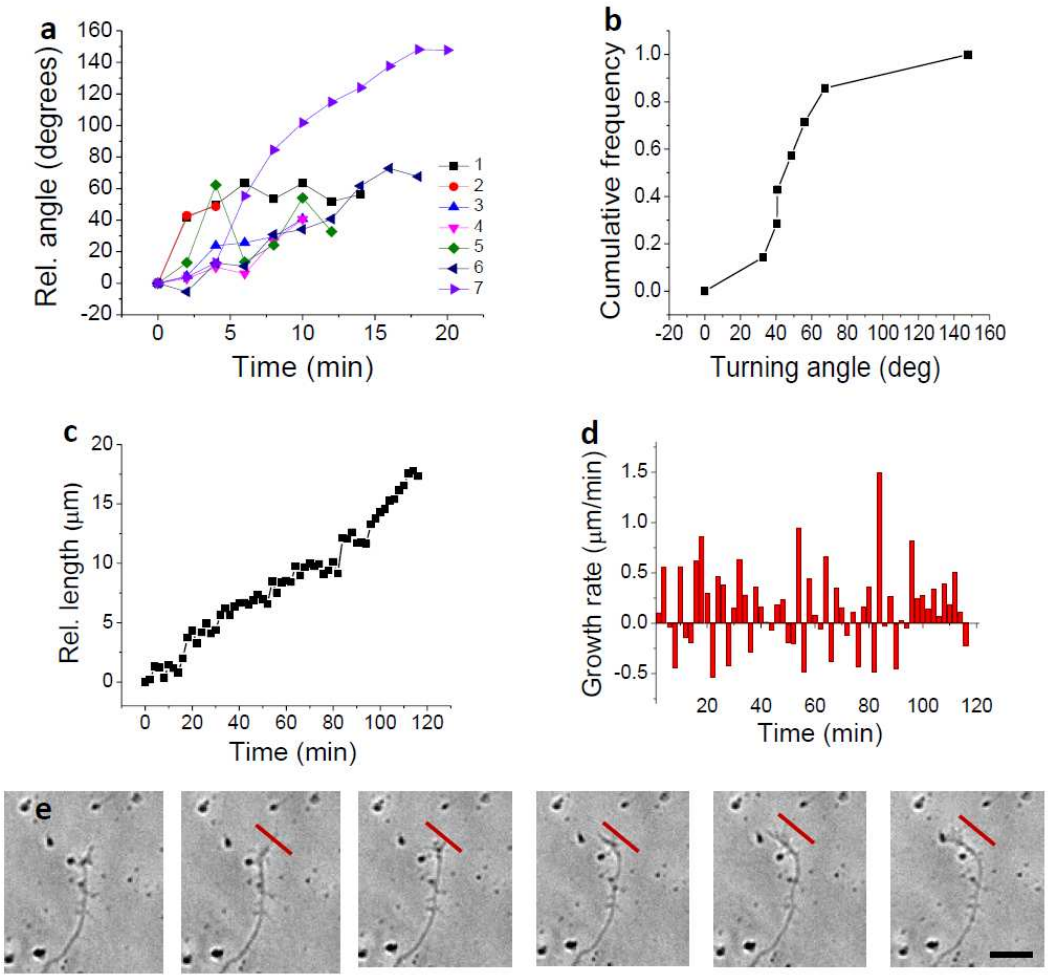

Figure 3-9 (a) Turning angle kinetics of laser-guided rat cortical axon using 20X microscope objective. (b) Cumulative plots for the distribution of laser-guided axonal turning angles. (c) Kinetics of net axonal growth during optical guidance. (d) Growth rate during multi-stage turning by spatio-temporally modulated laser beam. (e) Time-lapse (3 min) images of axonal guidance using spatially-sculpted line beam profile (marked as red line). Scale bar: 10 µm.

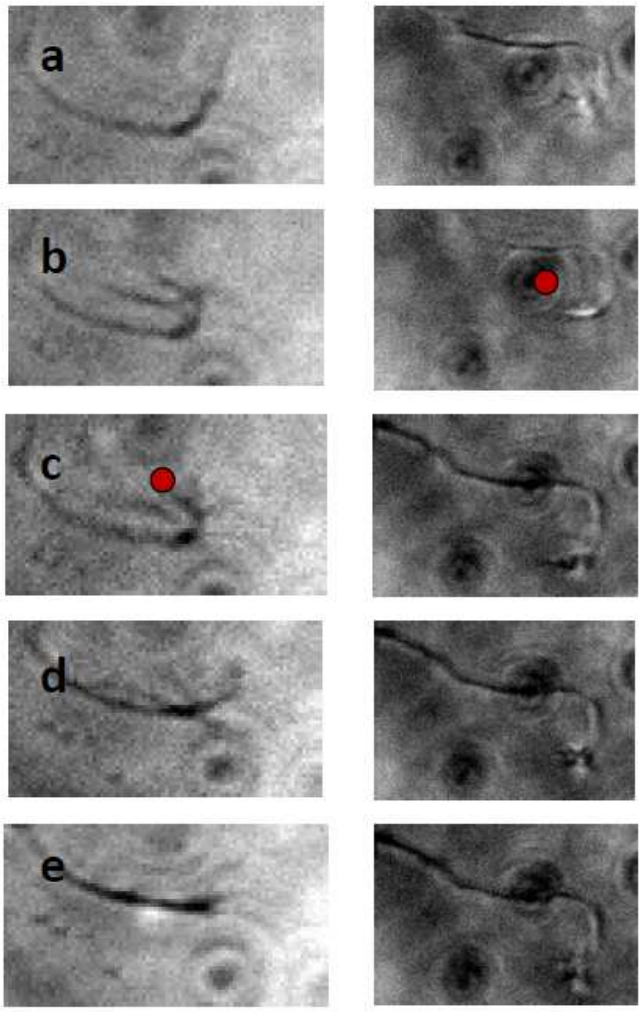

Figure 3-10 (A & B) Time-lapse images of inhibition of loop formation in rat cortical neuron realized by optically-induced repulsive cue. Laser spot is marked by red circle.

Next, we examined if axonal-loops can be formed with smaller radii of curvature using the repulsive-light cue and if self-fasciculation of cortical axon is modulated by such sharp turning processes. In Figure 3-8, we show time-lapse images (a-j) of laser-assisted fabrication of an axonal

loop having radius of curvature <0.5 µm (measurement limited by resolution of the 20X microscope objective). Figure 3-8 (A) shows the process of l-loop fabrication in optically-guided rat cortical axon using spatio-temporally varying laser spots. Though the self-fasciculated axon did not advance at a rate as before, such an I-loop constructed by laser based, repulsive-guidance method raises fundamental physical questions. Namely, what is the smallest radius of curvature that the axon can be bent without irreparably damaging it? The laser assisted repulsive guidance cue could be used to fabricate loops of different radius of curvature intermediary to that shown in Figure 3-7(~5 µm) and Figure 3-8 (< 1 µm). Figure 3-8 (a-d) shows time-lapse (4 min) phase-contrast images of an e-loop under construction. This loop being elliptic has two radii of curvatures (minor: ~4 µm). In this case also, self-fasciculation of the optically-guided axon was observed (Figure 3-8, e-h). Upon switching off the laser beam, the already-fasciculated axon advanced oppositely along the original axonal shaft (as in Figure 3-7). However, in this case, the radius of curvature of the optically-fabricated loop decreased (unlike Figure 3-7) to ~1.25 µm as shown in Figure 3-8 (e-h). Figure 3-8 (C) shows kinetics of change in loop diameter as function of time for the different cases (radii) of loop (Figure 3-7 vs Figure 3-8 A & B). While the larger axonal loop (radius

of approximately 5 μm) was found to be stable, stability of smaller loops were found to decrease as the loop radius decreased.

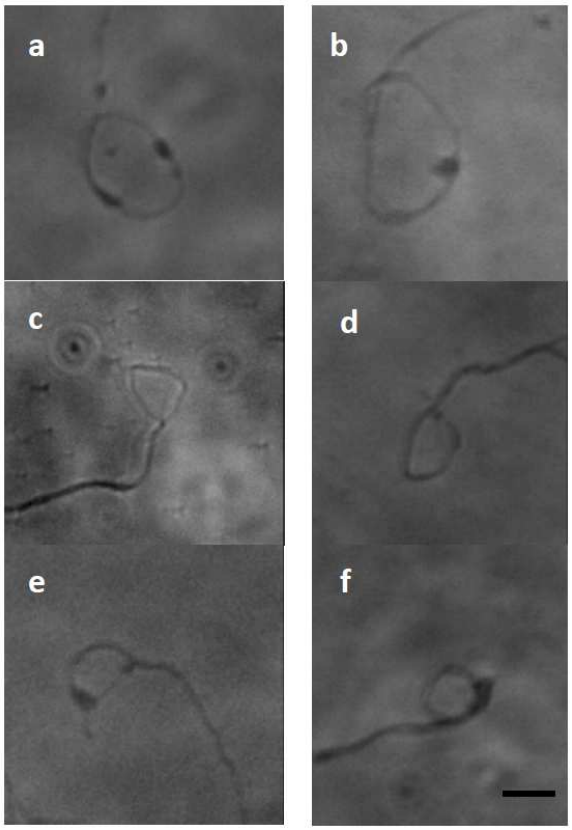

Figure 3-11 Random loop-formation by rat cortical neurons in culture platform (6 out of ~ 400 axonal terminals inspected in 50 fields of views). Scale bar: 10 μm.

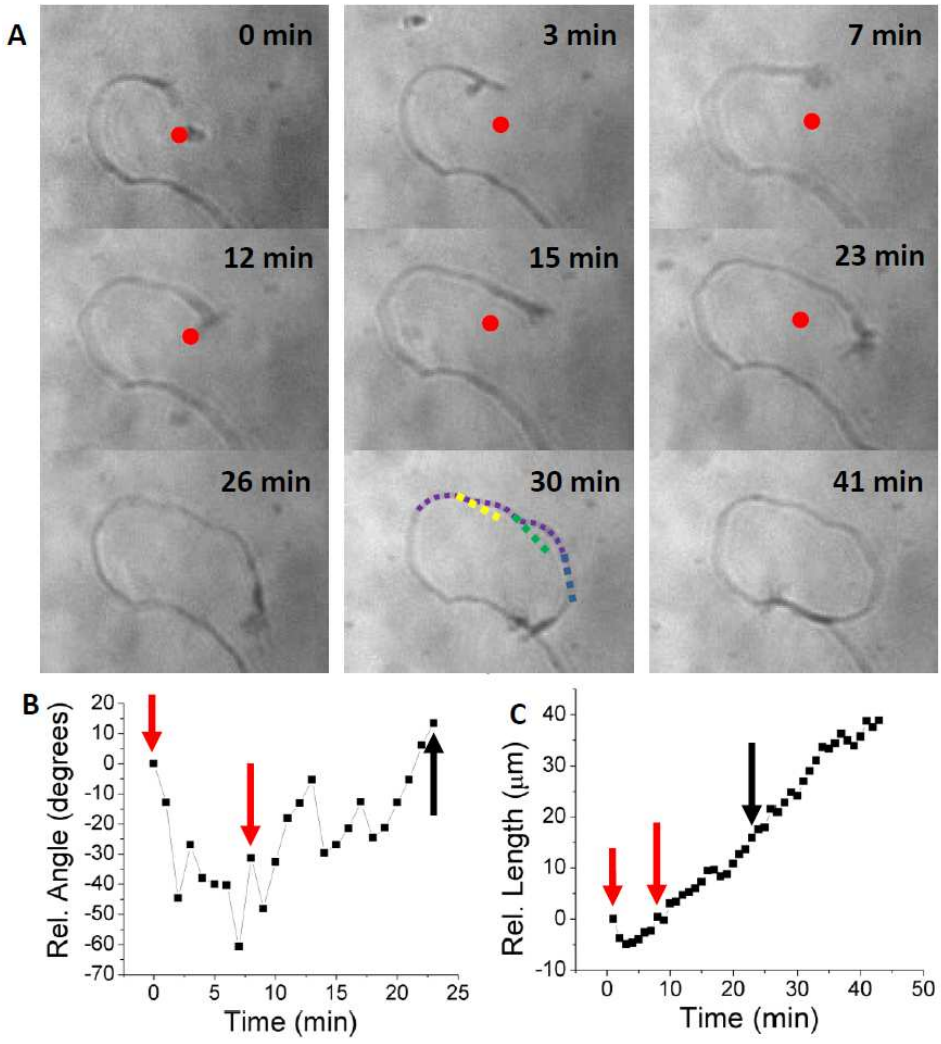

Figure 3-12 Laser-assisted axonal loop prevention. (a) Time-lapse series of multi-stage loop prevention (laser spot as red circle). (b) Dynamics of relative angle turned due to initial (short red arrow) and secondary (long red arrow) optical guidance. Laser off is denoted by a black arrow. (c) Dynamics of relative length during loop prevention due to initial (short red arrow) and secondary (long red arrow) optical guidance.

These results demonstrate that it is not only possible to facilitate loop formation with small radii of curvature, but it is also possible to prospectively prevent naturally occurring loop formation in vitro. We prefer to say prospectively because it is not possible for us to say that the axons selected for loop prevention were going to form loops with absolute certainty, given our present level of understanding. However, we can say that the selected axons' trajectories prior to application of the optical guidance cue put them on direct course for loop formation. Figure 3-12 A shows an advancing axon (0 min), which is observed to be on course for loop formation. The application of the NIR optical guidance cue (location marked by red circle) resulted in repulsive guidance (upwards turn, 7 min). After advancing beyond the static position of the laser spot, the axon again made a downward turn (12 min) towards itself and the laser spot was repositioned again into the axon's path. The axon again turned upward and continued to advance at near constant rate (Figure 3-12 (a), 15 min). The laser was not repositioned further to see whether the axon would continue to turn towards itself. Indeed it did, and eventually formed a complete loop and was observed to fasciculate along itself at a still-constant rate (Figure 3-12 (b)). Complete dynamics of the relative angle turned and relative length as a function of time are shown in Figure 3-12 (b and c). Although this is a single trial, it implies two things: that the axon

may be programmed (at some point in its lifetime) to form a loop and engage in self-fasciculation, regardless of the presence of transient cues which direct it away from itself. The results also imply that the transduced force provided by the optical guidance cue is greater than whatever force is causing the axon to engage in loop formation (whether it is programmed or not). Further single-stage axon loop prevention trials were also conducted, and resulted in prospective loop prevention three out of four times (Figure 3-10 A and B).

Investigations of Laser-induced Repulsive Guidance Mechanism (The Temperature Field Hypothesis)

By asymmetrically positioning a weakly focused laser microbeam in the path of an advancing axon, we have demonstrated that the beam acts as a repulsive guidance cue for primary E18 rat cortical axons. Since this effect does not require that the laser directly impinge upon the advancing growth cone, we have hypothesized that this powerful at-a-distance effect is the product of a temperature field, produced by laser light absorption in the surrounding medium. This hypothesis implies the activation of temperature sensitive membrane receptors, such as TRPV1 - a polymodal non-specific cation channel – and therefore an intracellular ion gradient.

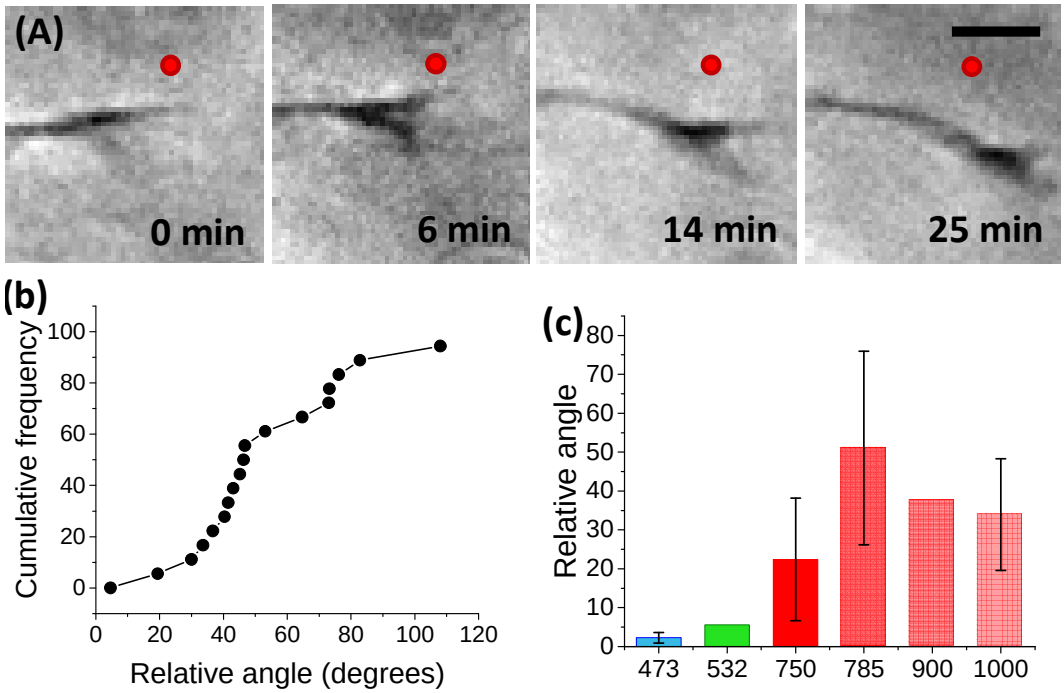

Figure 1: (A) Time lapse series of primary RCN axon responding to weakly focused (0.5 NA) laser spot (80 mW at 785 nm). (b) Cumulative frequency of relative turning angle for single guidance event (0.5 as well as 1.3 NA). (c) Wavelength dependence.

Fluorescence calcium imaging confirmed intracellular calcium increases in axonal growth cones as well as neuron cell bodies due to the presence of the laser beam. The level of calcium rise was found to be distance dependent. TRPV1 silencing experiments were also conducted, in which cortical neurons were incubated with SB-366791, a well-established TRPV1 antagonist. Further guidance experiments were conducted in which the extracellular calcium was depleted. In both cases,

the repulsive guidance effect was significantly reduced. Additionally, in order to remove the possibility of secondary or extraneous effects due to light's interaction with the cells or substrate, direct heating devices were fabricated and tested on primary RCN cultures. Significant repulsive guidance events were observed for 83% of advancing axons during direct heating experiments. These results conclusively demonstrate that shallow temperature gradients, on the scale of 0.5 ℃ acros s the width of the growth cone, are sufficient to modulate mammalian cortical axon steering, and result in repulsive axonal guidance. Here, we quantitatively test the hypothesis that laser-induced temperature fields are capable of significant repulsive guidance of E18 rat cortical axons. Additionally, we have fabricated titanium electrode heating devices, and directly tested whether shallow temperature gradients, on the scale of 0.5 ℃ across the growth cone, are sufficient to induce repulsive axonal guidance.

Calcium Fluorescence Imaging

1 mM stock Fluo-3 AM was mixed with warm (37 ℃) NB M to a 2 or 5 μM final concentration. The cell culture medium was then replaced with Fluo-3/NBM solution and allowed to incubate for 15 minutes at 37 ℃. Cells were washed for five minutes with fresh, warm NBM. After washing, NBM medium was replaced by warm Low-fluorescent Hibernate E medium (BrainBits) for imaging. A high pressure mercury lamp (Nikon)

served as the excitation source, which passed through a mechanically controlled filter wheel (on/off) and then a blue/green excitation/emission filter cube before being coupled to the back aperture of the microscope objective (100x, 1.3 NA), as seen in Figure 2-4. Images were collected by an EMCCD (Cascade, Photometrics) and processed/analyzed with ImageJ (NIH) software. Stacked time-lapse image sequences were analyzed by the ImageJ ROI Manager, which measured the selected regions integrated intensity. All regions of interest used in the analysis of a single experimental image sequences were of equal size.

Fluorescence experiments were first conducted on RCN growth cones. Figure 5(A) shows a time-lapse series in which a clear global increase in the fluorescence of the growth cone can be observed following application of laser guidance cue. Figure 5(c) shows the dynamical global influx of intracellular calcium. However, we were unable to detect asymmetric fluorescence increases in the growth cones when the laser was applied. Furthermore, growth cones treated with Fluo-3 AM, even at this relatively low concentration (2-5 μM) and incubation period (15 min), were not advancing, even after extended periods of time (60 min). Since the expression of temperature sensitive ion channels is not restricted to the growth cone, we also performed fluorescence calcium influx imaging on RCN cell bodies. Figure 5(B) shows a clear increase in global

fluorescence for Cell 1, nearest to the laser spot. Figure 5(d) shows the dynamical increase of the fluorescence intensity for all cells within the field of view. As one would expect, less substantial fluorescence increases (none in some cases) were observed with greater separation from the focused laser spot. Figure 5(e) shows the fractional percentage difference (ΔF/F %) for three trials conducted on RCN cell bodies (n=11), collected into different separation domains. There is a clear increase in ΔF/F for cells in the nearest separation domain, whereas cell bodies in the farthest domains are nearer to their respective baselines. As a reminder, laser-induced temperature field simulations (Figure 2(c-d)) illustrate that the temperature is expected to decay to the baseline value within 50-60 μm from the center of the laser spot. Although we were unable to detect asymmetric calcium influx, the significant global fluourescence increase following application of laser at-a-distance indicates that temperature sensitive calcium channels are activated. Additionally, we found one neuron in vitro which was exhibiting spontaneous calcium spikes (Figure 3-14). When the laser spot was applied nearby, the calcium spiking rate increased (Figure 3-15). When the laser source was turned off, the spiking rate decreased nearer to the baseline rate. Although this is only a single trial, it may be that the steady state temperature field is sufficient to

increase firing rates in vitro, similar to other studies reporting such results for temperature rams using perfusive solution.

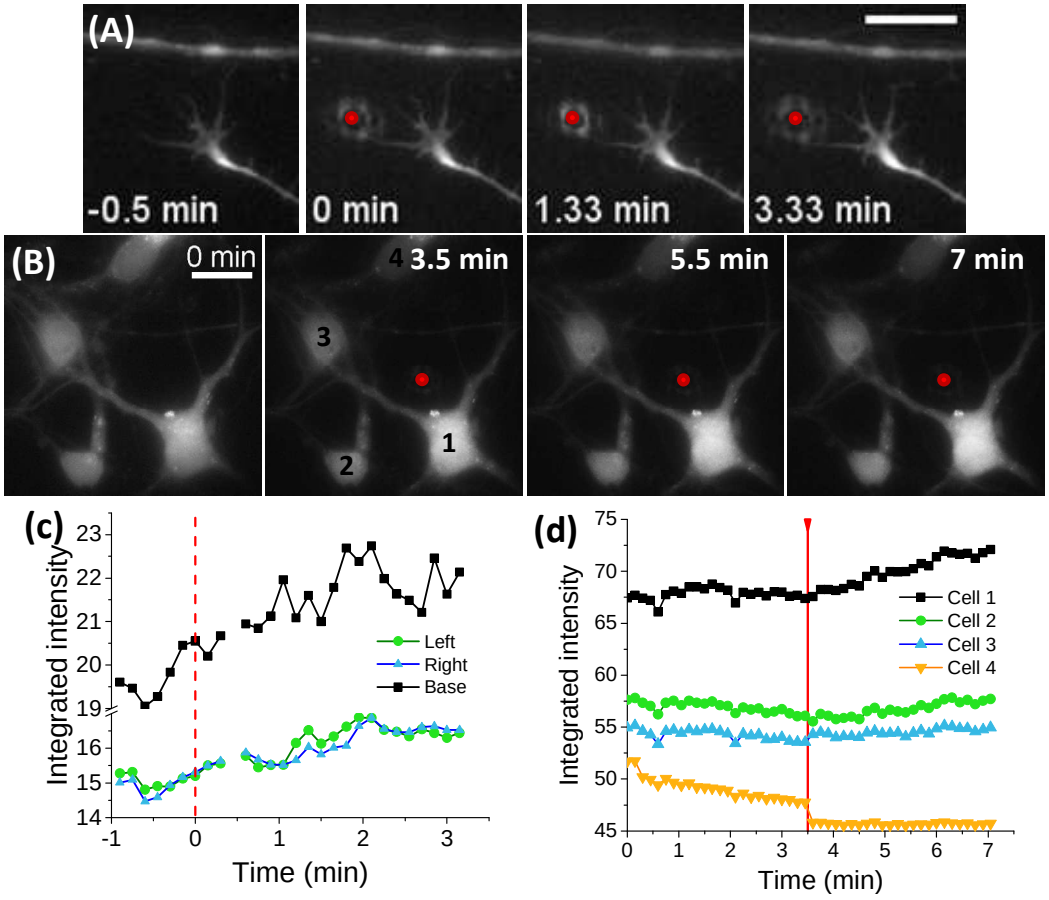

Figure 5: (A) Epifluorescence time-lapse images of RCN growth cone (5 μM Fluo-3 AM) exposed to 1064 nm (10 mW) focused (1.3 NA) laser spot at a distance. (B) Epifluorescence time-lapse images of RCN cell bodies. (c) Fluorescence dynamics of RCN growth cone (left, right, and central base). (d) Fluorescence dynamics of 4 RCN cell bodies. Laser on denoted by red line.

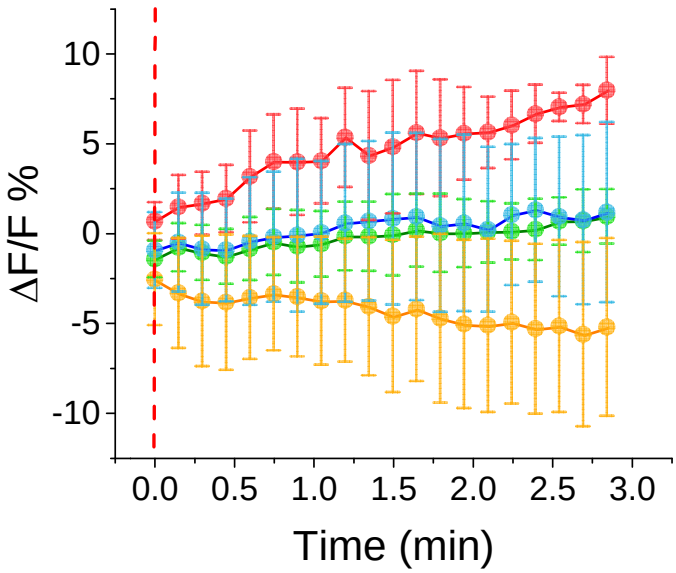

Figure 3-13 Average change in fluorescence for the nearest (red), middle (green, blue) and farthest (orange) removed cells.

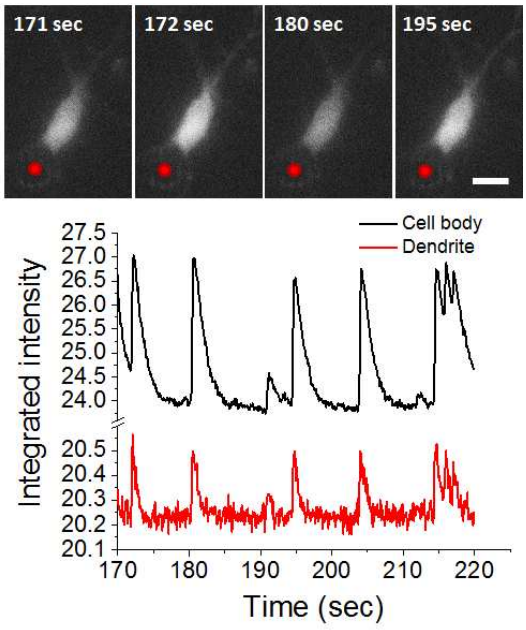

Figure 3-14 Calcium spiking events during the application of 10 mW laser at 1000 nm (red circle)

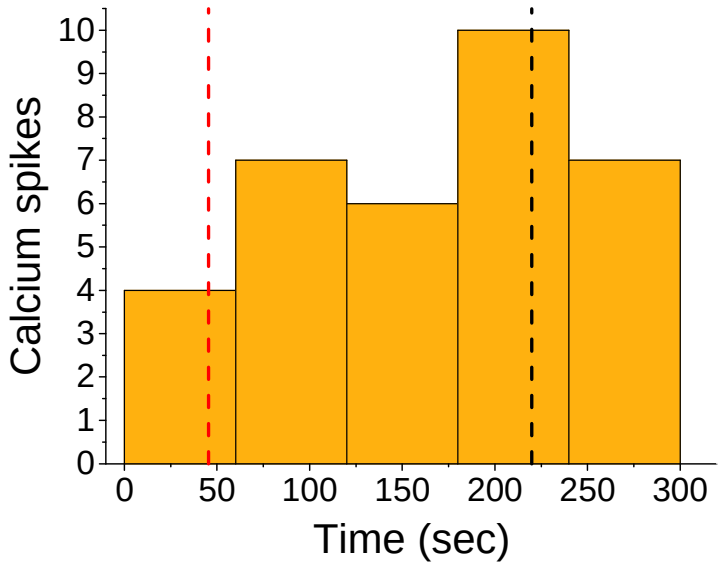

Figure 3-15 Calcium spikes per minute. Dashed red line indicates laser on and black dashed line indicates laser off

Calcium-free (Depletion) Experiments

Experiments were also performed after replacing the normal cell culture medium with calcium-free medium. The repulsive guidance effect was significantly reduced in trials conducted with calcium-free medium, resulting in an average turning angle of -4.9 ± 9.2 degrees (n=7). This surprisingly, but strongly, implies that the guidance mechanism is mediated by calcium influx.

TRPV1 channel blocked (silencing) experiments

In order to determine whether TRPV1 channels were primarily responsible for the intracellular calcium gradient and, therefore, the

guidance effect, silencing experiments were conducted using positive control parameters in the presence of 10 μM SB-366791, a well-established TRPV1 antagonist (20-23). Cells were allowed to incubate with the channel antagonist for 1 hr at 37 ℃ prior to experiments.

Silencing experiments resulted in a dramatic decrease in the axonal guidance response to the laser guidance cue (n=17). Of the 17 trials, 14 axons were observed to grow beyond the static position of the laser spot with an average turning angle of -3.5 ± 20.2 degrees. Many of the TRPV1 treated axons interacted directly with the laser spot, even growing directly through the laser spot in several instances (n=2), as seen in Figure 3-16. Figure 3-16 shows one such instance of guidance in the presence of SB-366791, in which the axon grows straight, very near to the laser spot. Since the axon is not effectively guided away from the laser spot, it suffers from prolonged irradiation and eventually the axon shaft buckles, and the axon retracts. Furthermore, several growth cones appeared to become optically trapped following laser interaction, echoing the results of attractive laser-based guidance experiments.

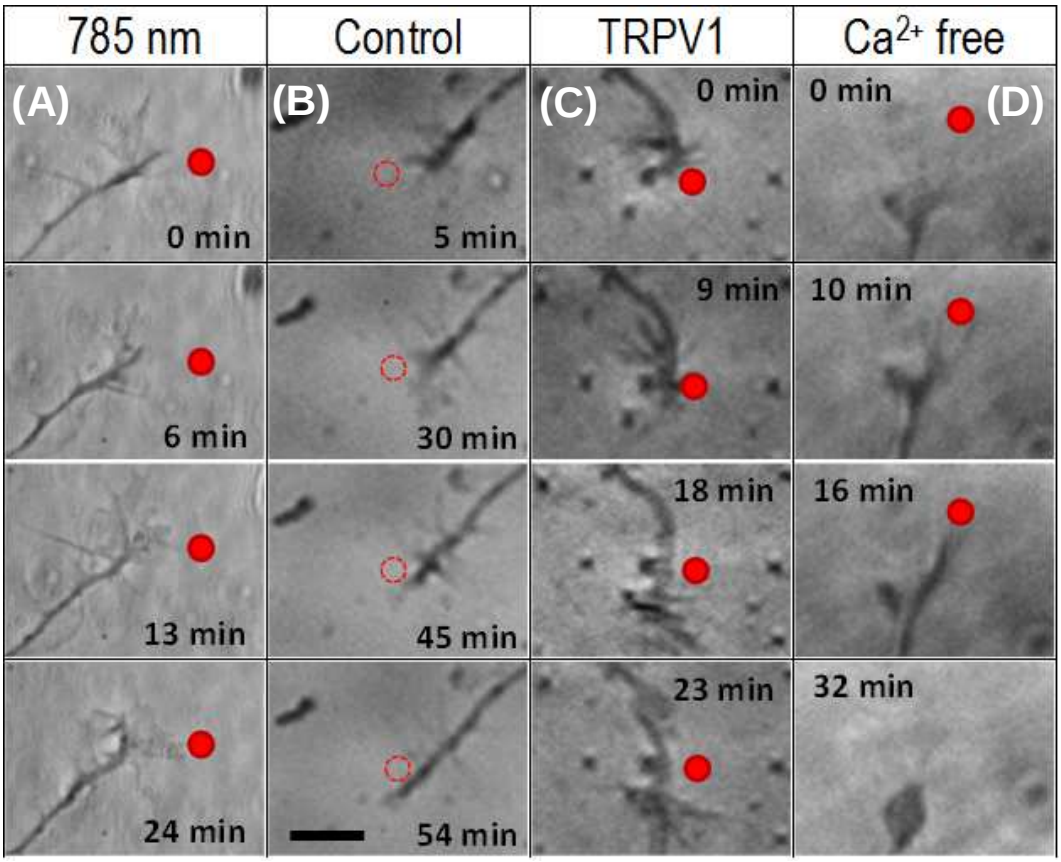

Figure 3-16 Guidance trial outcomes for (A) positive control (785 nm, 100x, 1.3 NA MO), (B) negative control (no laser, 20x, 0.5 NA MO), (C) TRPV1 (10 μM SB-366791, 20x, 0.5 NA MO), and calcium-free (20x, 0.5 NA MO) experiments

The statistical significance of the positive control was tested against the negative control, silencing, and depletion experimental data groups. A one-way ANOVA F-test, performed in Origin 9.1, identified the population means as significantly different (Prob>F = 9.4 x 10-10). Individual two-tailed t-tests were then performed between the positive control and other

groups (equal variances not assumed), identifying the positive control as statistically significant (e.g. P = 9.7 x 10-5 when compared with negative control).

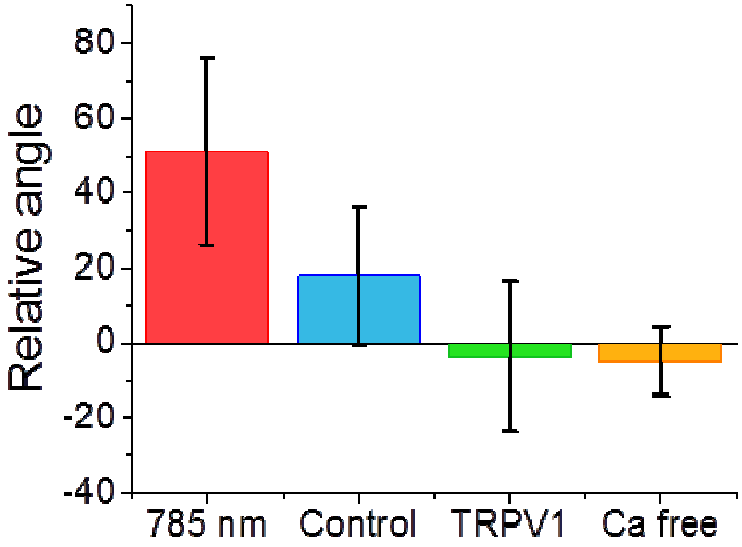

Figure 3-17 Mean relative angle turned and standard deviation for positive control (785 nm), negative control (Control), antagonist (TRPV1), and calcium-free (Ca free) experiments.

Simulations of laser-induced temperature rise due to absorption of light by culture medium

Finite element simulations were carried out to determine the magnitude and distribution of the temperature field due to a focused laser spot. The temporal- and spatial-dependent temperature rise will be given by the standard heat diffusion equation:

$$\rho c\left(\frac{\partial T}{\partial t}\right)=\frac{k}{r^2}\frac{\partial}{\partial r}\left(r^2\frac{\partial T}{\partial r}\right)+q(r,t) \tag{27}$$

where the source term, q(r,t) is proportional to the z-dependent intensity (I_o(r,t)) of a focused, Gaussian laser beam multiplied by the linear absorption of the cell culture medium (water), α.

$$q(r,t)=\alpha I_0(r,t) \tag{28}$$

I_o(r,t) is related to the measured laser power at the sample site (P) and the radial distance from the laser spot center:

$$I_0(r,t)=\frac{2P}{\pi w^2(z)}\exp\left[-\frac{2a^2(r,t)}{w^2(z)}\right] \tag{29}$$

where w(z) is typically the z-dependent beam waist diameter, with z measured from the laser focal plane. In this study, we have reduced the problem to two-dimensions, assuming the laser spot is focused at the interface between the glass and cell culture medium domains, and neglecting medium absorption at higher z values. In that case

$$w(z)=w_0=\frac{1.22\lambda}{NA} \tag{30}$$

The resulting second order differential equation can be solved in Matlab using the inbuilt PDE toolbox. Dirichlet boundary conditions were imposed at the geometrical limits of the cell culture medium domain (circular, 1 mm diameter). The triangular mesh was initialized and refined

by the PDE toolbox to have mesh growth of 1.3 from the center of the source term.

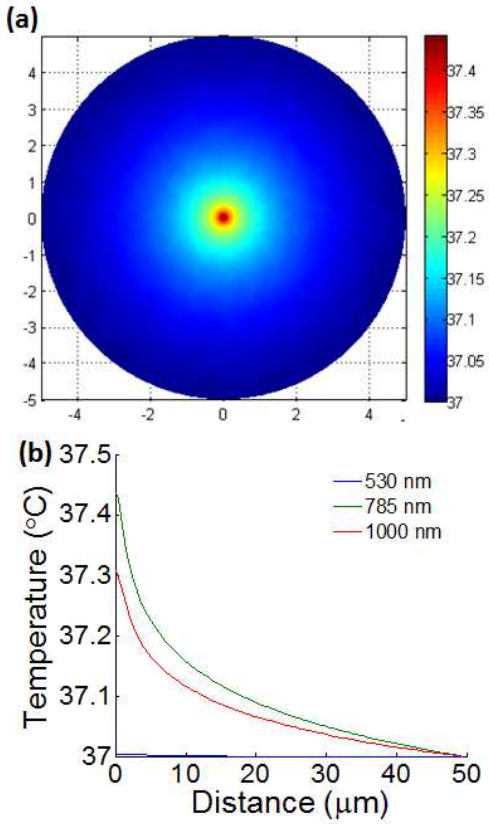

Figure 3-18 (c) Temperature field contour plot for weakly focused (0.5 NA) laser beam (785 nm, 80 mW). (d) Radial line plot of temperature field at 785 nm (80 mW, green), 1000 nm (10 mW, red), and 532 nm (10 mW, blue).

We have assumed that all the energy absorbed by the medium goes towards heating and, as in other simulations, we neglect the higher order absorption of culture medium proteins, pH indicators (phenol red),

and the direct absorption of scattered light by cells or cellular components. The absorption of 785 nm light by the glass coverslip is assumed to be negligible compared to that of the cell culture medium ($\alpha < 0.01$).

Furthermore, we have directly measured the temperature rise using an infrared camera. Although the spatial resolution of this camera (40 μm) was insufficient to determine a temperature gradient due to the laser spot, we were able to determine the total temperature rise within our region of interest (Figure 3-19). Figure 3-19 shows two trials of applying focused laser spot within our region of interest versus the negative control (no laser). Both trials show a temperature increase of approximately 0.5 degrees and saturation of temperature rise within 180 seconds.

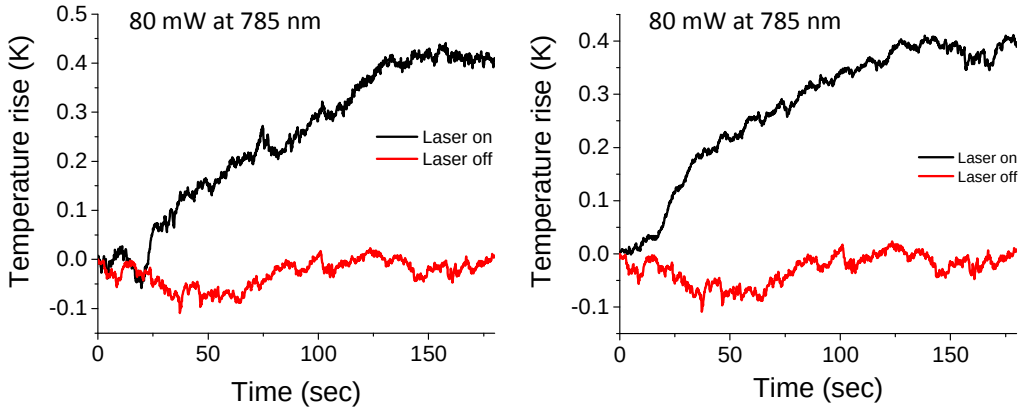

Figure 3-19 Temerpature rise due to focused (1.25 NA, 100x) laser spot and 80 mW as measured by infrared camera.

Simulating temperature-dependent TRPV1 opening probability

The probability that a protein changes its conformational state is relatable to the Gibb's free energy difference between the two states (open and closed), and is therefore necessarily a function of temperature.

$$P_o(T) = \frac{1}{1+\exp\left(\frac{\Delta G}{RT}\right)} \tag{31}$$

The temperature dependence of the Gibb's free energy difference can be expressed by the well-known thermodynamic equality

$$\Delta G(T) = \Delta H(T) - T\Delta S(T) - zFV \tag{32}$$

where ΔH is the temperature dependent enthalpy change, ΔS is the temperature dependent entropy change, z is the gating charge, F is Faraday's constant, and V is the transmembrane potential. The expressions for enthalpy and entropy are also temperature dependent functions, which are related to the specific heat capacity changes (ΔC_p) with temperature while at constant pressure.

$$\Delta H(T) = \left(\Delta H_0 - \Delta C_p T_R\right) + \Delta C_p T \tag{33}$$

$$\Delta S(T) = \left(\Delta S_0 - \Delta C_p \ln(T_R)\right) + \Delta C_p \ln(T) \tag{34}$$

where ΔH_o and ΔS_o are the enthalpy and entropy values at the reference temperature (T_R). These values, along with ΔC_p are experimentally determined values, and have been taken, in our case, from previous experimental findings. Since there is some discrepancy in

experimental determinations of ΔC_p in the physiological range of temperatures, we have plotted the temperature dependent opening probability for ΔC_p spanning the range of reported values (8-20 kJ mol^{-1} K^{-1}). Simulations were carried out in Matlab 209A using standard interpolation for Equation 6.

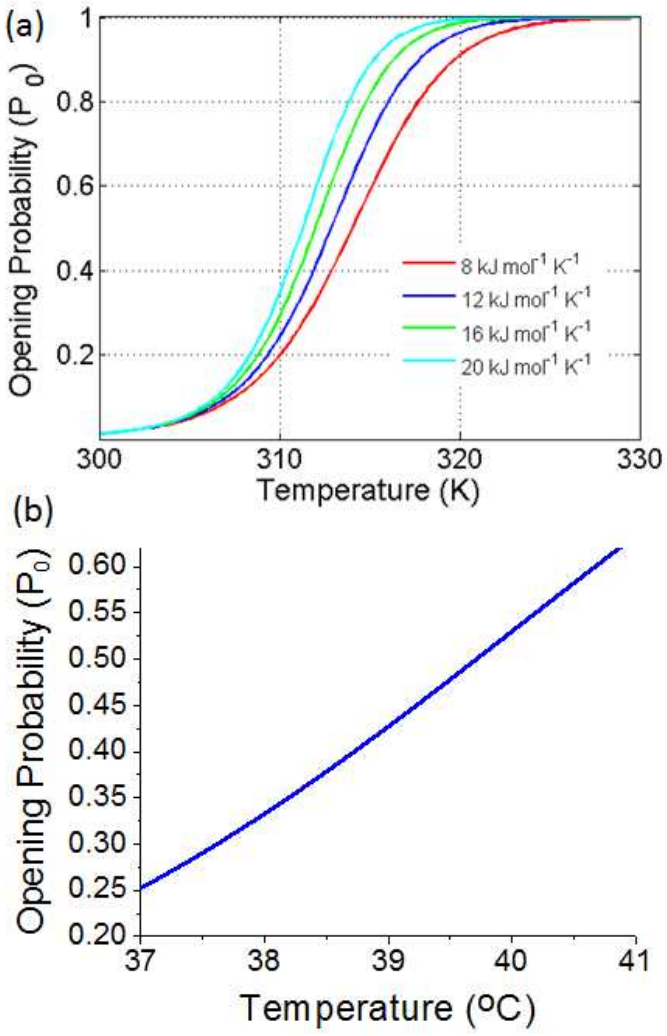

Figure 3-20 (a) TRPV1 channel temperature-dependent opening probability for specific heat variances (ΔC) of 8 (red), 12 (blue), 16 (green), and 20 (turquoise) kJ mol^{-1} K^{-1}. (b) Experimentally relevant zoomed region of TRVP1 temperature-dependent opening probability.

Direct Heating Experiments

Materials and Methods

Microheater devices were fabricated, calibrated, and effects simulated by Dr. Ankur Jain and Vivek Vishwakarma. The following methods section reflects their input and expertise, which is necessary to include for the basis of understanding and experimental design.

Microheater devices were fabricated in a class 100 cleanroom facility. Devices are comprised of a thin metal (titanium) heating line connected to four electrode pads on standard glass slides. Titanium is used as the microheater material due to its well-known biocompatibility, as well as its high electrical resistivity, which is ideal in order to generate large temperature increases.In addition, titanium has a large temperature coefficient of resistivity (TCR), which makes it an ideal material for simultaneous use as a temperature sensor.

Glass slides are ultra-cleaned prior to microfabrication using a piranha solution (3H2SO4:H2O2), followed by cleaning steps in acetone, methanol and DI water. Photolithography is then carried out in an OAI manual front/backside contact mask aligner. Deposition of 0.2 μm titanium is carried out in an AJA ATC ORION evaporator. Finally, lift-off in acetone results in the definition of metal features on the substrate. The fabricated microheating element is 1.8 cm long and 40-60 μm wide.

Calibration of the heating device is carried out prior to its use as a temperature sensor based on resistance thermometry. The calibration process involves measurement of the electrical resistance of the microheater line as a function of temperature. The microfabricated device is mounted on an Instec HCS622V thermal stage capable of precise temperature control. The resistance of the microheater line is measured as a function of temperature, by passing a small electric current from a Keithley 2612A source meter, and measuring voltage across the microheater line using a Keithley 2100 voltmeter. The test current is chosen to be small enough to not cause significant self-heating, and yet provide measurable voltage. Micro-heater resistance is measured to be a linear function of temperature, as expected. The simultaneous measurement of resistance and current during heating experiments can be used to precisely determine the temperature of the microheater line in real time.

Finite element simulations are also carried out to determine the nature and magnitude of temperature gradient around the heater line. The temperature distribution in the microheater device is governed by the energy conservation equation given by

$$k\frac{\partial^2 T}{\partial x^2}+k\frac{\partial^2 T}{\partial y^2}+k\frac{\partial^2 T}{\partial z^2}=\rho C_p\frac{\partial T}{\partial t} \quad (35)$$

where T is the temperature increase relative to the ambient temperature.

Equation (35) is solved using a finite-element simulation code with a mesh containing at least 300,000 nodes, in order to ensure grid independence of results. Joule heating due to electric current passing through the microheater line is modeled, and natural convection is assumed on the top of the microheater device. The entire device is assumed to be at 37 ℃ prior to application of the heating current.

Figure 3-21(a) shows the steady state temperature distribution around the heater line upon passing a electric current through the heater, indicating that the heater is 1 ℃ hotter than the ambient. The temperature rise of the heater can be modulated by changing the heating current. Figure 3-21 (b) plots the steady-state temperature as a function of distance away from the heater, indicating a sharp temperature gradient in the vicinity of the heater. This temperature profile decays away to the ambient temperature as distance from the heater increases. The evolution of the temperature distribution with time, starting from the application of the electric current, reaches steady-state conditions within 150 ms.

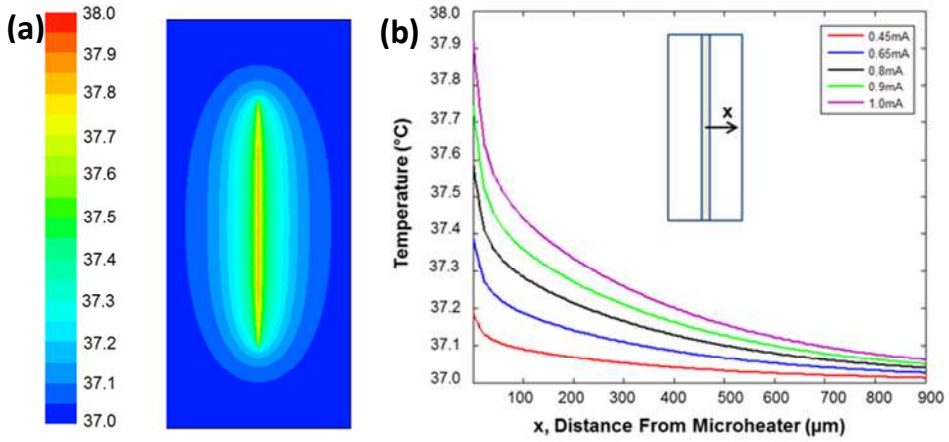

Figure 3-21 (a) Temperature field contour plot of temperature rise due to 1 mA current. (b) Horizontal line profile of steady-state temperature field during direct heating experiment. x=0 corresponds to electrode-medium (water) interface.

A temperature rise of only a few ℃ is required for experiments to investigate the behavior of cortical neurons in a temperature field. The appropriate electric current required for a specific temperature rise is determined by measuring the microheater resistance upon passage of the electric current, and using the calibration plots to determine the microheater temperature. It is estimated that based on the accuracy of calibration, and the least count of the sourcemeter, the accuracy of temperature measurement of the microheater line during experiment is approximately 0.1 ℃. A Keithley 2612A source meter is used during experiments to send the heating current through the microheater, while a

Keithley 2100 voltmeter is used to monitor the electrical resistance, and hence the temperature of the microheater line.

Results

In order to rule out all other possible secondary or extraneous effects due to light's interaction with the cells or substrate, direct heating devices were fabricated and tested on primary rat cortical neuron cultures (illustrated in Figure 3-22 (a)). A 1 mA current was passed through a 60 μm diameter titanium electrode affixed to a glass slide. This current corresponds to a 1 ℃ temperature rise (37 to 38 ℃) at the electrode-medium boundary (Figure 3-21) and decays sharply to the baseline temperature (~37.05 ℃) within 1 mm. All experiment al results (n=12) are from axons found to be growing within the first field of view removed from the titanium electrode (~200 μm in either direction). Temperature fields due to direct heating experiments are calculated to reach the steady state condition within ~150 ms.

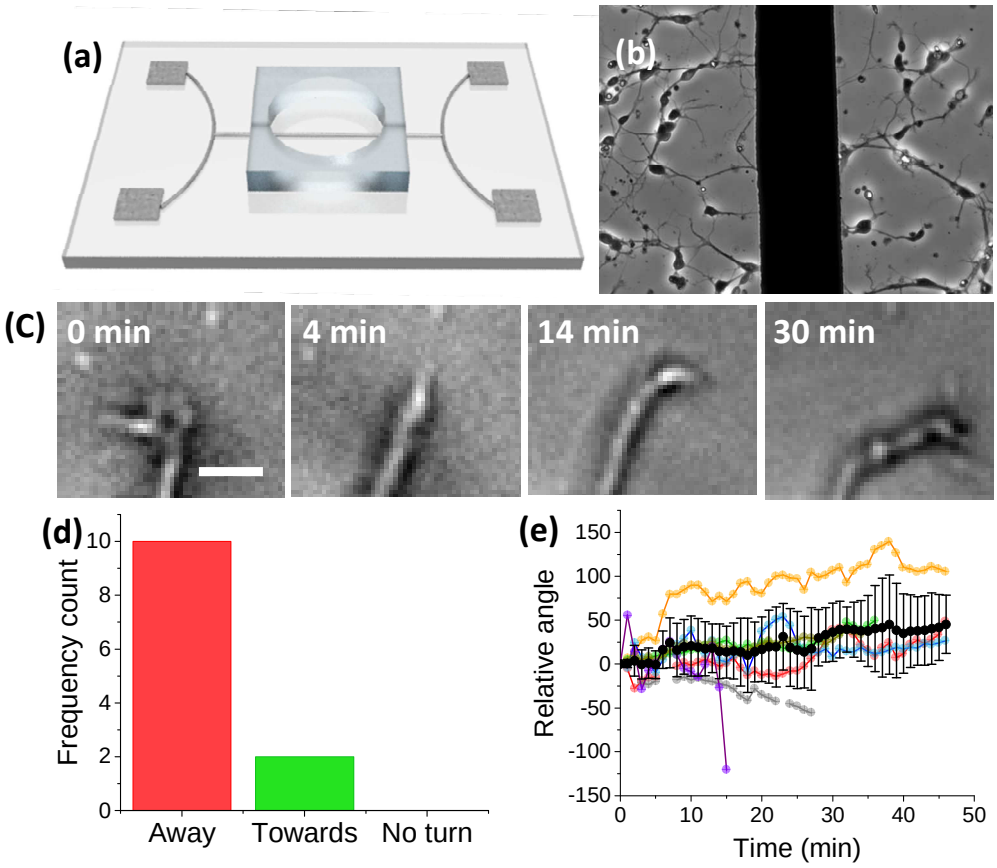

Figure 3-22 (a) Illustration of titanium electrode microheating device (not to scale). (b) Phase contrast image of 60 μm heating element (black bar) and cultured RCNs. (C) Time-lapse images (20x, Ph1) of guidance due to electrode-based 1 ℃ increase at interface (l(left of the field of view). (d) Frequency count turns away, towards or no turn (< 10 degrees). (e) Relative angle vs. time for advancing axons (n=12) during direct heating experiments with mean and standard deviation at each time point (black circles and error bars).

83% of advancing axons were found to ultimately turned away from the titanium electrode within 1 hr (Figure 3-22 (d)). Figure 3-22 (C) shows a time-lapse series of images demonstrating the repulsive guidance effect induced by the 1 ℃ temperature rise, initiated at t = 0 min (electrode is out of frame: left). Figure 3-22 (e) shows the dynamical orientation of all observed advancing growth cones, along with the average and standard deviation with time (black circles with error bars). A steady increase in the relative turning angle is clear, with the average repulsive guidance angle reaching 45.3 ± 33.3. These experiments independently confirm the temperature field hypothesis (in the absence of laser light). Although direct heating effects are believed to be the primary means of repulsive axonal guidance, further evaluation of the electric field effects due to the heating device current may be warranted, as steady-state DC fields have been shown to induce guidance of primary axons. However, the alternating electric field of laser-induced repulsive axonal guidance is expected to be negligible. And since it is alternating, no sustained directional effect is anticipated due to the residual electric field.

Discussion

To conclude, we have demonstrated a simple, yet novel and highly effective optical method for neuronal guidance. This method was found to be highly efficient for guiding primary RCN as well as retinal ganglion cell

axons. This noncontact method permits multiple and sequential operations to be performed on the axonal growth cone, resulting in high angled turns in the case of RGC axons, and the formation of axonal loops in the case of RCNs. Therefore, it seems likely that this method can be extended for formation of neuronal networks in vitro by spatiotemporal control of the laser beam. This can be achieved by use of scanning laser beams or sculpting the laser spots by diffractive optical elements, SLMs, and even standard digital light projectors. Being able to form in vitro neuronal circuitry with high fidelity by the noninvasive photonic-guidance method described here will allow us to probe the functions of basic building blocks of the neuronal network. This can be augmented by ultrafast NIR laser scissors (152, 153) for nanosurgery of undesired connections. Further, in combination with optical stimulation and imaging tools (24), this will enable all-optical testing of computational nature of the neuronal circuit. Since this NIR light-based method does not require a tightly focused laser beam, the use of fiber optic delivery of the laser-induced guidance cue could allow in-depth guidance and manipulation of neural circuitry. This would likely require that the optical fibers to be tapered, either mechanically or chemically, in order to generate a sufficient temperature gradient across the width of the neuronal growth cone. Further, combined with mechanical placement of cells using and optical tweezers, and with the NIR laser

allowing sensitization of neurons by transfection of opsin-encoding genes (154), and also for two-photon optogenetic stimulation and optical imaging (155), rapid progress can be made in the all-optical control of neuronal circuit formation and activity as well as mapping functional networks of brain.

It may be noted that current intervention strategies for spinal cord injury (SCI) do not ensure robust axonal outgrowth, specifically corticospinal tract (CST), past the distal glial scar. The optical repulsive cue provides a unique opportunity for rerouting the regenerating CST axons toward spared axonal tracks across the glial scar in-vivo. Use of such optical non-contact and non-invasive methods will significantly impact on development of innovative SCI treatments. The optimization of effective laser profiles, as well as the integration of automated laser/stage systems should allow for dynamical control of axonal growth paths.

Both laser- and titanium electrode-based guidance experiments resulted in significant axon repulsion. Silencing TRPV1 channels with SB-366791 and (separately) depleting the extracellular calcium independently abolished the repulsive axon guidance response, confirming the temperature field hypothesis. We have successfully demonstrated that steady-state (transiently sustained) shallow temperature gradients, on the scale of 0.1 ℃ across the width of the growth cone , can cause repulsive

guidance in primary mammalian cortical axons. This is a surprising and profound finding for several reasons.

Although the TRPV1 activation threshold temperature is commonly reported to be between 40-43 ℃ (131, 156-158), sev eral researchers have demonstrated that inward currents due to TRVP1 activation begin at lower, more physiologically relevant temperatures (134, 135). In a report by Sharif-Naeini et al.(159), ~2 min temperature ramps from 31 and 36 to 38 ℃ were applied to vasopressin neurons (known to express TRPV1 channels) via heated solution perfusion. Inward current responses and significant firing rate differences were observed compared to PVZ neurons, which do not express TRPV1 channels, and TRPV1-silenced experiments (1 μM SB-366791). Additionally, TRPV1 and TRPV3 channels are known to coexpress and heteromultimerize (TRPV channels as cellular sensors) in the mammalian cerebral cortex. Our silencing of TRPV1 channels may, therefore, be non-selectively modulating TRPV3 channels, which are known to be activated at lower, physiological temperatures (35-39 ℃); or by activating a TRPV1/T RPV3 hybrid channel. Additionally, it has been shown that thermal fluctuations can drive or reduce the force of actin polymerization, effecting lamellipodia protrusion/extension.

More powerful and complex temperature gradients can now be produced, following the same microfabrication strategies employed here. The resulting guidance responses could shed light on whether temperature gradients on the scale of those measured during embryonic development might affect neurogenesis or early neural development. They might also elucidate new therapeutic strategies for guided nerve regeneration or selective re-innervation. It is definitely worth nothing that sustained, or even pulsed, shallow temperature fields may not be an ideal candidate for regenerative or therapeutic applications due to reports that repeated stimulation of cells by activation of TRPV1 channels may lead to apoptosis.

Although guidance experiments conducted with calcium-free medium seemed to abolish the guidance response, it is necessary to address the fact that changing the baseline extracellular calcium levels may significantly effect the outgrowth and potential guidance of primary axons in ways not connected to this particular guidance cue. It is the opinion of this author that calcium-free or depleted guidance experiments, in and of themselves, are not useful in analyzing the repulsive cue guidance efficacy. As discussed, altering the shape of the intracellular calcium ion distribution is tantamount to creating an entirely different cue, possibly attractive when it was repulsive or vice versa.

It would be easy to mistakenly conclude that our findings are contradictory to those reported in attractive, laser-based optical guidance studies. We believe that they are, in fact, complimentary. Apart from optical forces stabilizing actin filaments and/or microtubules, the shape of the intracellular calcium gradient is known to be largely responsible for the determination of whether a guidance cue is attractive or repulsive. Experiments in which the laser is focused directly on the growth cone are reasonably expected to induce steeper intracellular calcium gradients. Decreased separation between the sample and laser spot will only increase the temperature and temperature gradient across the growth cone, increasing the opening probability of temperature sensitive membrane channels. Additionally, forces due to direct impingement of the laser spot on the growth cone may be activating stretch-sensitive calcium ion channels. The resulting calcium influx sum may bring local intracellular calcium concentrations into the optimal “attractive” range.

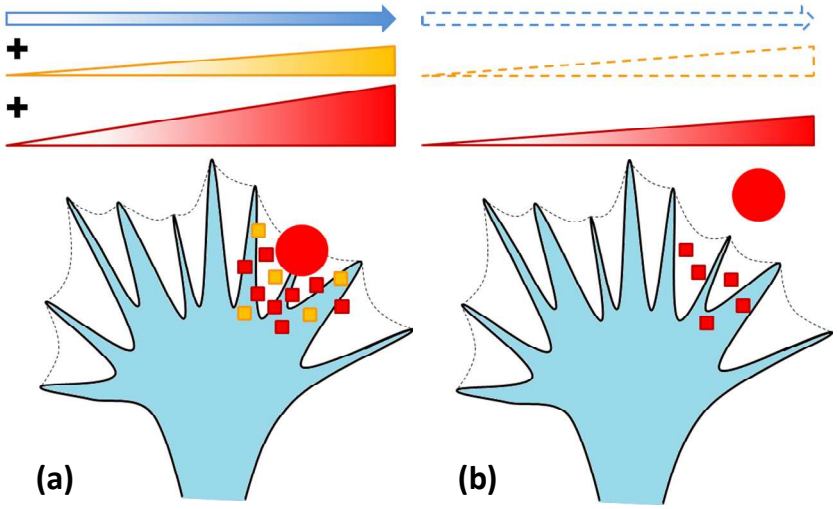

Figure 3-23 Illustration of the additive mechanistic contributions for attractive and repulsive laser-based axonal guidance. Blue arrow indicates direct optical stabilization. Orange gradient indicates activation of mechanosensitive calcium ion channels. Red gradient indicates activation of temperature-sensitive calcium ion channels. Red and orange rectangles represent accumulating intracellular calcium ions.

We propose a quantitative analysis of inward currents due to both attractive and repulsive laser-based guidance methods via electrophysiological recordings. Temperature- and stretch-activated channel silencing experiments (TRPV3 as well as TRPV1) could also be conducted to determine whether optical force-stabilization of filopodia and microtubules alone is sufficient to evoke attractive laser-based guidance.

References

1. Black B, Mondal A, Kim Y, Mohanty SK. Neuronal beacon. Opt Lett. 2013 Jul 1;38(13):2174-6.

2. Black BJ, Mohanty SK. Fiber-optic spanner. Opt Lett. 2012 Dec 15;37(24):5030-2.

3. Black BJ, Luo D, Mohanty SK. Fiber-optic rotation of micro-scale structures enabled microfluidic actuation and self-scanning two-photon excitation. Appl Phys Lett. 2012;101(22).

4. Black BJ, Gu L, Mohanty SK. Highly effective photonic cue for repulsive axonal guidance. PLoS One. 2014 Apr 9;9(4):e86292.

5. Haghshenas-Jaryani M, Black B, Ghaffari S, Drake J, Bowling A, Mohanty S. Dynamics of microscopic objects in optical tweezers: Experimental determination of underdamped regime and numerical simulation using multiscale analysis. Nonlinear Dyn. 2014 04/01;76(2):1013-30.

6. Oraevsky AA, Da Silva LB, Rubenchik AM, Feit MD, Glinsky ME, Perry MD, et al. Plasma mediated ablation of biological tissues with nanosecond-to-femtosecond laser pulses: Relative role of linear and nonlinear absorption. Selected Topics in Quantum Electronics, IEEE Journal of. 1996;2(4):801-9.

7. Ashkin A. History of optical trapping and manipulation of small-neutral particle, atoms, and molecules. Selected Topics in Quantum Electronics, IEEE Journal of. 2000;6(6):841-56.

8. Burns MM, Fournier J, Golovchenko JA. Optical binding. Phys Rev Lett. 1989 09/18;63(12):1233-6.

9. McGloin D. Optical tweezers: 20 years on. Philos Trans A Math Phys Eng Sci. 2006 Dec 15;364(1849):3521-37.

10. Grzegorczyk TM, Kemp BA, Kong JA. Passive guiding and sorting of small particles with optical binding forces. Opt Lett. 2006 Nov 15;31(22):3378-80.

11. Van Thourhout D, Roels J. Optomechanical device actuation through the optical gradient force. Nat Photon. 2010;4(4):211-7.

12. Swartzlander GA, Peterson TJ, Artusio-Glimpse AB, Raisanen AD. Stable optical lift. Nat Photon. 2011;5(1):48-51.

13. Baigl D. Photo-actuation of liquids for light-driven microfluidics: State of the art and perspectives. Lab Chip. 2012 Oct 7;12(19):3637-53.

14. Mohanty S. Optically-actuated translational and rotational motion at the microscale for microfluidic manipulation and characterization. Lab Chip. 2012;12(19):3624-36.

15. Ashkin A, Dziedzic JM, Bjorkholm JE, Chu S. Observation of a single-beam gradient force optical trap for dielectric particles. Opt Lett. 1986 May;11(5):288-90.

16. Galajda P, Ormos P. Complex micromachines produced and driven by light. Appl. Phys. Lett. 2001;78(2):249-51.

17. Mohanty SK, Uppal A, Gupta PK. Self-rotation of red blood cells in optical tweezers: Prospects for high throughput malaria diagnosis. Biotechnol. Lett. 2004;26(12):971-4.

18. Dasgupta R, Mohanty SK, Gupta PK. Controlled rotation of biological microscopic objects using optical line tweezers. Biotechnology Letters. 2003;25(19):1625-8.

19. Friese MEJ, Nieminen TA, Heckenberg NR, Rubinsztein-Dunlop H. Optical alignment and spinning of laser-trapped microscopic particles. Nature. 1998;394(6691):348-50.

20. He H, Friese MEJ, Heckenberg NR, Rubinsztein-Dunlop H. Direct observation of transfer of angular momentum to absorptive particles from a laser beam with a phase singularity. Phys. Rev. Lett. 1995;75(5):826-9.

21. Padgett M, Bowman R. Tweezers with a twist. Nat Photon. 2011;5(6):343-8.

22. Bingelyte V, Leach J, Courtial J, Padgett MJ. Optically controlled three-dimensional rotation of microscopic objects. Appl. Phys. Lett. 2003;82(5):829-31.

23. Constable A, Kim J, Mervis J, Zarinetchi F, Prentiss M. Demonstration of a fiber-optical light-force trap. Opt. Lett. 1993;18(21):1867-9.

24. Mohanty SK, Mohanty KS, Berns MW. Manipulation of mammalian cells using a single-fiber optical microbeam. J Biomed Opt. 2008 Sep-Oct;13(5):054049.

25. Kreysing MK, Kießling T, Fritsch A, Dietrich C, Guck JR, Käs JA. The optical cell rotator. Opt. Express. 2008;16(21):16984-92.

26. Abedin KS, Kerbage C, Fernandez-Nieves A, Weitz DA. Optical manipulation and rotation of liquid crystal drops using high-index fiber-optic tweezers. Appl. Phys. Lett. 2007;91(9):091119,091119-3.

27. Cardenas N, Yu L, Mohanty SK. Probing orientation and rotation of red blood cells in optical tweezers by digital holographic microscopy. Optical Diagnostics and Sensing XI: Toward Point-of-Care Diagnostics; and Design and Performance Validation of Phantoms Used in Conjunction with Optical Measurement of Tissue III. 2011;7906:790613-9.

28. Kolb T, Albert S, Haug M, Whyte G. Dynamically reconfigurable fibre optical spanner. Lab Chip. 2014 Mar 21;14(6):1186-90.

29. Reynolds O. An experimental investigation of the circumstances which determine whether the motion of water shall be direct or sinuous, and of the law of resistance in parallel channels. Proceedings of the Royal Society of London. 1883;35:84-99.

30. Mishra YN, Ingle N, Mohanty SK. Trapping and two-photon fluorescence excitation of microscopic objects using ultrafast single-fiber optical tweezers. Journal of Biomedical Optics. 2011 Oct;16(10):105003.

31. Terray A, Oakey J, Marr DWM. Microfluidic control using colloidal devices. Science. 2002 June 7, 2002;296(5574):1841-4.

32. Ladavac K, Grier D. Microoptomechanical pumps assembled and driven by holographic optical vortex arrays. Opt. Express. 2004;12(6):1144-9.

33. Pedaci F, Huang Z, van Oene M, Barland S, Dekker NH. Excitable particles in an optical torque wrench. Nat Phys. 2011;7(3):259-64.

34. Wang Y, Botvinick EL, Zhao Y, Berns MW, Usami S, Tsien RY, et al. Visualizing the mechanical activation of src. Nature. 2005;434(7036):1040-5.

35. Wu T, Nieminen TA, Mohanty S, Miotke J, Meyer RL, Rubinsztein-Dunlop H, et al. A photon-driven micromotor can direct nerve fibre growth. Nat Photon. 2012;6(1):62-7.

36. Noack J, Vogel A. Laser-induced plasma formation in water at nanosecond to femtosecond time scales: Calculation of thresholds, absorption coefficients, and energy density. Quantum Electronics, IEEE Journal of. 1999;35(8):1156-67.

37. Vogel A, Noack J, HÃ¼ttman G, Paltauf G. Mechanisms of femtosecond laser nanosurgery of cells and tissues. Applied Physics B. 2005 12/01;81(8):1015-47.

38. Kohli V, Elezzabi AY. Laser surgery of zebrafish (danio rerio) embryos using femtosecond laser pulses: Optimal parameters for exogenous material delivery, and the laser's effect on short- and long-term development. BMC Biotechnol. 2008 Jan 29;8:7,6750-8-7.

39. Supatto W, Debarre D, Moulia B, Brouzes E, Martin JL, Farge E, et al. In vivo modulation of morphogenetic movements in drosophila embryos with femtosecond laser pulses. Proc Natl Acad Sci U S A. 2005 Jan 25;102(4):1047-52.

40. Chris B Schaffer and André Brodeur and,Eric Mazur. Laser-induced breakdown and damage in bulk transparent materials induced by tightly focused femtosecond laser pulses. Measurement Science and Technology. 2001;12(11):1784.

41. Stockert JC, Juarranz A, Villanueva A, Canete M. Photodynamic damage to HeLa cell microtubules induced by thiazine dyes. Cancer Chemoth Pharm. 1996 Nov-Dec;39(1-2):167-9.

42. Jackson SL, Heath IB. The dynamic behavior of cytoplasmic F-actin in growing hyphae. Protoplasma. 1993;173(1-2):23-34.

43. Sanders MC, Wang YL. Exogenous nucleation sites fail to induce detectable polymerization of actin in living cells. J Cell Biol. 1990 Feb;110(2):359-65.

44. Hapala I. Breaking the barrier: Methods for reversible permeabilization of cellular membranes. Critical reviews in biotechnology. 1997;17(2):105-22.

45. Gresch O, Engel FB, Nesic D, Tran TT, England HM, Hickman ES, et al. New non-viral method for gene transfer into primary cells. Methods. 2004 Jun;33(2):151-63.

46. Heiser WC. Gene delivery to mammalian cells. Totowa, N.J.: Humana Press; 2004.

47. Thomas CE, Ehrhardt A, Kay MA. Progress and problems with the use of viral vectors for gene therapy. Nat Rev Genet. 2003 May;4(5):346-58.

48. Tan Y, Sun D, Huang W. Mechanical modeling of red blood cells during optical stretching. Journal of biomechanical engineering. 2010 Apr;132(4):044504.

49. Cardenas N, Yu LF, Mohanty SK. Stretching of red blood cells by optical tweezers quantified by digital holographic microscopy. Proc Spie. 2011;7897.

50. Soughayer JS, Krasieva T, Jacobson SC, Ramsey JM, Tromberg BJ, Allbritton NL. Characterization of cellular optoporation with distance. Anal Chem. 2000 Mar 15;72(6):1342-7.

51. Vogel A, Linz N, Freidank S, Paltauf G. Femtosecond-laser-induced nanocavitation in water: Implications for optical breakdown threshold and cell surgery. Physical review letters. 2008 Jan 25;100(3):038102.

52. Schaffer C, Nishimura N, Glezer E, Kim A, Mazur E. Dynamics of femtosecond laser-induced breakdown in water from femtoseconds to microseconds. Optics express. 2002 Feb 11;10(3):196-203.

53. Kodama T, Hamblin MR, Doukas AG. Cytoplasmic molecular delivery with shock waves. Faseb J. 2000 May 11;14(8):A1473-.

54. Kodama T, Doukas AG, Hamblin MR. Shock wave-mediated molecular delivery into cells. Bba-Mol Cell Res. 2002 Jan 30;1542(1-3):186-94.

55. Schneckenburger H, Hendinger A, Sailer R, Strauss WSL, Schmitt M. Laser-assisted optoporation of single cells. J Biomed Opt. 2002 Jul;7(3):410-6.

56. Palumbo G, Caruso M, Crescenzi E, Tecce MF, Roberti G, Colasanti A. Targeted gene transfer in eucaryotic cells by dye-assisted laser optoporation. J Photoch Photobio B. 1996 Oct;36(1):41-6.

57. Mohanty SK, Sharma M, Gupta PK. Laser-assisted microinjection into targeted animal cells. Biotechnol Lett. 2003 Jun;25(11):895-9.

58. Baumgart J, Bintig W, Ngezahayo A, Willenbrock S, Murua Escobar H, Ertmer W, et al. Quantified femtosecond laser based opto-perforation of living GFSHR-17 and MTH53 a cells. Optics express. 2008 Mar 3;16(5):3021-31.

59. Davis AA, Farrar MJ, Nishimura N, Jin MM, Schaffer CB. Optoporation and genetic manipulation of cells using femtosecond laser pulses. Biophysical journal. 2013 Aug 20;105(4):862-71.

60. Cooper JA. Effects of cytochalasin and phalloidin on actin. The Journal of cell biology. 1987 Oct;105(4):1473-8.

61. Tien AC, Backus S, Kapteyn H, Murnane M, Mourou G. Short-pulse laser damage in transparent materials as a function of pulse duration. Phys Rev Lett. 1999 May 10;82(19):3883-6.

62. Gordienko VM, Mikheev PM, Syrtsov VS. Nonmonotonic behavior of the absorption of the tightly focused femtosecond radiation of a cr :

Forsterite laser in a dielectric due to an increase in the number of photons involved in the process. Jetp Lett+. 2005;82(4):228-31.

63. Born M, Wolf E. Principles of optics : Electromagnetic theory of propagation, interference and diffraction of light. 7th expanded ed. Cambridge ; New York: Cambridge University Press; 1999.

64. Gruzelier JH. Syndromes of schizophrenia and schizotypy, hemispheric imbalance and sex differences: Implications for developmental psychopathology. Int J Psychophysiol. 1994 Dec;18(3):167-78.

65. Sherwin BB. Can estrogen keep you smart? evidence from clinical studies. J Psychiatry Neurosci. 1999 Sep;24(4):315-21.

66. Hall ED, Pazara KE, Linseman KL. Sex differences in postischemic neuronal necrosis in gerbils. J Cereb Blood Flow Metab. 1991 Mar;11(2):292-8.

67. Roof RL, Hall ED. Gender differences in acute CNS trauma and stroke: Neuroprotective effects of estrogen and progesterone. J Neurotrauma. 2000 May;17(5):367-88.

68. Roof RL, Hall ED. Estrogen-related gender difference in survival rate and cortical blood flow after impact-acceleration head injury in rats. J Neurotrauma. 2000 Dec;17(12):1155-69.

69. O'Connor Ca, Cernak I, Vink R. Both estrogen and progesterone attenuate edema formation following diffuse traumatic brain injury in rats. Brain Res. 2005 11;1062(1-2):171-4.

70. Murphy SJ, McCullough LD, Smith JM. Stroke in the female: Role of biological sex and estrogen. ILAR J. 2004;45(2):147-59.

71. Niewada M, Kobayashi A, Sandercock PA, Kaminski B, Czlonkowska A, International Stroke Trial Collaborative Group. Influence of gender on baseline features and clinical outcomes among 17,370 patients with confirmed ischaemic stroke in the international stroke trial. Neuroepidemiology. 2005;24(3):123-8.

72. Wilson ME, Liu Y, Wise PM. Estradiol enhances akt activation in cortical explant cultures following neuronal injury. Brain Res Mol Brain Res. 2002 Jun 15;102(1-2):48-54.

73. Wilson ME, Dubal DB, Wise PM. Estradiol protects against injury-induced cell death in cortical explant cultures: A role for estrogen receptors. Brain Res. 2000 Aug 11;873(2):235-42.

74. Sortino MA, Chisari M, Merlo S, Vancheri C, Caruso M, Nicoletti F, et al. Glia mediates the neuroprotective action of estradiol on beta-amyloid-induced neuronal death. Endocrinology. 2004 Nov;145(11):5080-6.

75. Tripanichkul W, Sripanichkulchai K, Finkelstein DI. Estrogen down-regulates glial activation in male mice following 1-methyl-4-phenyl-1,2,3,6-tetrahydropyridine intoxication. Brain Res. 2006 Apr 21;1084(1):28-37.

76. Nakazawa T, Takahashi H, Shimura M. Estrogen has a neuroprotective effect on axotomized RGCs through ERK signal transduction pathway. Brain Res. 2006 06;1093(1):141-9.

77. BESSIS M, TER-POGOSSIAN MM. Micropuncture of cells by means of a laser beam. Ann N Y Acad Sci. 1965 May 28;122:689-94.

78. Berns MW, Olson RS, Rounds DE. In vitro production of chromosomal lesions with an argon laser microbeam. Nature. 1969 Jan 4;221(5175):74-5.

79. Amy RL, Storb R. Selective mitochondrial damage by a ruby laser microbeam: An electron microscopic study. Science. 1965 Nov 5;150(3697):756-8.

80. Difato F, Tsushima H, Pesce M, Guiggiani A, Benfenati F, Blau A, et al. Axonal regeneration of cultured mouse hippocampal neurons studied by an optical nano-surgery system.

81. Yanik MF, Cinar H, Cinar HN, Chisholm AD, Jin Y, Ben-Yakar A. Neurosurgery: Functional regeneration after laser axotomy. Nature. 2004 Dec 16;432(7019):822.

82. Schumacher M, Weill-Engerer S, Liere P, Robert F, Franklin RJ, Garcia-Segura LM, et al. Steroid hormones and neurosteroids in normal

and pathological aging of the nervous system. Prog Neurobiol. 2003 Sep;71(1):3-29.

83. Pawluski JL, Brummelte S, Barha CK, Crozier TM, Galea LA. Effects of steroid hormones on neurogenesis in the hippocampus of the adult female rodent during the estrous cycle, pregnancy, lactation and aging. Front Neuroendocrinol. 2009 Aug;30(3):343-57.

84. Strom JO, Theodorsson A, Theodorsson E. Mechanisms of estrogens' dose-dependent neuroprotective and neurodamaging effects in experimental models of cerebral ischemia. Int J Mol Sci. 2011;12(3):1533-62.

85. Wilson ME, Dubal DB, Wise PM. Estradiol protects against injury-induced cell death in cortical explant cultures: A role for estrogen receptors. Brain Res. 2000 08;873(2):235-42.

86. Davenport RW, Dou P, Mills LR, Kater SB. Distinct calcium signaling within neuronal growth cones and filopodia. J Neurobiol. 1996 Sep;31(1):1-15.

87. Hutson LD, Chien CB. Pathfinding and error correction by retinal axons: The role of astray/robo2. Neuron. 2002 Jan 17;33(2):205-17.

88. Katz MJ. How straight do axons grow? The Journal of neuroscience : the official journal of the Society for Neuroscience. 1985 03;5(3):589-95.

89. Gittes F, Mickey B, Nettleton J, Howard J. Flexural rigidity of microtubules and actin filaments measured from thermal fluctuations in shape. J Cell Biol. 1993 02;120(4):923-34.

90. Mueller BK. Growth cone guidance: First steps towards a deeper understanding. Annu Rev Neurosci. 1999;22:351-88.

91. Lowery LA, Van Vactor D. The trip of the tip: Understanding the growth cone machinery. Nat Rev Mol Cell Bio. 2009 May;10(5):332-43.

92. Chedotal A, Richards LJ. Wiring the brain: The biology of neuronal guidance. Csh Perspect Biol. 2010 Jun;2(6).

93. Pittman AJ, Law MY, Chien CB. Pathfinding in a large vertebrate axon tract: Isotypic interactions guide retinotectal axons at multiple choice points. Development. 2008 Sep 1;135(17):2865-71.

94. Erskine L, Herrera E. The retinal ganglion cell axon's journey: Insights into molecular mechanisms of axon guidance. Dev Biol. 2007 Aug 1;308(1):1-14.

95. Harrelson AL. Molecular mechanisms of axon guidance in the developing insect nervous-system. J Exp Zool. 1992 Mar 1;261(3):310-21.

96. Inatani M. Molecular mechanisms of optic axon guidance. Naturwissenschaften. 2005 Dec;92(12):549-61.

97. Fawcett J. Repair of spinal cord injuries: Where are we, where are we going? Spinal Cord. 2002 Dec;40(12):615-23.

98. Zeck G, Fromherz P. Noninvasive neuroelectronic interfacing with synaptically connected snail neurons immobilized on a semiconductor chip. P Natl Acad Sci USA. 2001 Aug 28;98(18):10457-62.

99. Fromherz P. Three levels of neuroelectronic interfacing - silicon chips with ion channels, nerve cells, and brain tissue. Ann Ny Acad Sci. 2006;1093:143-60.

100. Mai J, Fok L, Gao HF, Zhang X, Poo MM. Axon initiation and growth cone turning on bound protein gradients. J Neurosci. 2009 Jun 10;29(23):7450-8.

101. Yu TW, Bargmann CI. Dynamic regulation of axon guidance. Nat Neurosci. 2001 Nov;4:1169-76.

102. Borisy GG, Svitkina TM. Actin machinery: Pushing the envelope. Curr Opin Cell Biol. 2000 Feb;12(1):104-12.

103. Dickson BJ. Molecular mechanisms of axon guidance. Science. 2002 Dec 6;298(5600):1959-64.

104. Ming GL, Wong ST, Henley J, Yuan XB, Song HJ, Spitzer NC, et al. Adaptation in the chemotactic guidance of nerve growth cones. Nature. 2002 May 23;417(6887):411-8.

105. Hoffman-Kim D, Mitchel JA, Bellamkonda RV. Topography, cell response, and nerve regeneration. Annu Rev Biomed Eng. 2010;12:203-31.

106. Patel N, Poo MM. Orientation of neurite growth by extracellular electric-fields. J Neurosci. 1982;2(4):483-96.

107. Blau A, Weinl C, Mack J, Kienle S, Jung G, Ziegler C. Promotion of neural cell adhesion by electrochemically generated and functionalized polymer films. J Neurosci Meth. 2001 Nov 15;112(1):65-73.

108. Wu T, Mohanty S, Gomez-Godinez V, Shi LDZ, Liaw LH, Miotke J, et al. Neuronal growth cones respond to laser-induced axonal damage. J R Soc Interface. 2012 Mar 7;9(68):535-47.

109. Luo Y, Shoichet MS. A photolabile hydrogel for guided three-dimensional cell growth and migration. Nat Mater. 2004 Apr;3(4):249-53.

110. Ehrlicher A, Betz T, Stuhrmann B, Koch D, Milner V, Raizen MG, et al. Guiding neuronal growth with light. P Natl Acad Sci USA. 2002 Dec 10;99(25):16024-8.

111. Mohanty SK, Sharma M, Panicker MM, Gupta PK. Controlled induction, enhancement, and guidance of neuronal growth cones by use of line optical tweezers. Opt Lett. 2005 Oct 1;30(19):2596-8.

112. Jesse F, Miao Z, Zhao L, Chen Y, Lv YY. Optical fiber light source directs neurite growth. Biomedical optics express. 2013 04;4(4):614-8.

113. Mathew M, Amat-Roldan I, Andres R, Santos SICO, Artigas D, Soriano E, et al. Signalling effect of NIR pulsed lasers on axonal growth. J Neurosci Meth. 2010 Feb 15;186(2):196-201.

114. Wu T, Nieminen TA, Mohanty S, Miotke J, Meyer RL, Rubinsztein-Dunlop H, et al. A photon-driven micromotor can direct nerve fibre growth. Nat Photonics. 2012 Jan;6(1):62-7.

115. Gittes F, Mickey B, Nettleton J, Howard J. Flexural rigidity of microtubules and actin filaments measured from thermal fluctuations in shape. J Cell Biol. 1993 02;120(4):923-34.

116. Bernhardt R. Axonal pathfinding during the regeneration of the goldfish optic pathway. J Comp Neurol. 1989 06;284(1):119-34.

117. Ashkin A, Dziedzic JM, Bjorkholm JE, Chu S. Observation of a single-beam gradient force optical trap for dielectric particles. Opt Lett. 1986 May;11(5):288-90.

118. Sachs F. Stretch-activated ion channels: What are they? Physiology. 2010 Feb;25(1):50-6.

119. Sachs F. Mechanical transduction by membrane ion channels - a mini review. Mol Cell Biochem. 1991 May 29;104(1-2):57-60.

120. Gomez TM, Spitzer NC. Regulation of growth cone behavior by calcium: New dynamics to earlier perspectives. J Neurobiol. 2000 08;44(2):174-83.

121. Harada Y. Radiation forces on a dielectric sphere in the rayleigh scattering regime. . 1996;124:529-41.

122. Ian B. The role of calcium activity in cortical axon growth and guidance. . 2009.

123. Komuro H, Rakic P. Orchestration of neuronal migration by activity of ion channels, neurotransmitter receptors, and intracellular Ca2+ fluctuations. J Neurobiol. 1998 Oct;37(1):110-30.

124. Komuro H, Kumada T. Ca2+ transients control CNS neuronal migration. Cell Calcium. 2005 May;37(5):387-93.

125. Henle SJ, Wang G, Liang E, Wu M, Poo M, Henley JR. Asymmetric PI(3,4,5)P3 and akt signaling mediates chemotaxis of axonal growth cones. The Journal of neuroscience : the official journal of the Society for Neuroscience. 2011 05;31(19):7016-27.

126. Hong K, Nishiyama M, Henley J, Tessier-Lavigne M, Poo M. Calcium signalling in the guidance of nerve growth by netrin-1. Nature. 2000 01;403(6765):93-8.

127. Zheng JQ. Turning of nerve growth cones induced by localized increases in intracellular calcium ions. Nature. 2000 01;403(6765):89-93.

128. Hayes P, Meadows HJ, Gunthorpe MJ, Harries MH, Duckworth DM, Cairns W, et al. Cloning and functional expression of a human orthologue of rat vanilloid receptor-1. Pain. 2000 11/1;88(2):205-15.

129. Clapham DE, Runnels LW, StrÃ¼bing C, Medical HH. The trp ion channel family. . 2001;2.

130. Benham CD, Gunthorpe MJ, Davis JB. TRPV channels as temperature sensors. Cell Calcium. 2003 0;33(5–6):479-87.

131. Zheng J. Molecular mechanism of TRP channels. Compr Physiol. 2013 Jan;3(1):221-42.

132. Cesare P, Moriondo A, Vellani V, McNaughton PA. Ion channels gated by heat. Proceedings of the National Academy of Sciences. 1999 July 06;96(14):7658-63.

133. Kaneko Y, Szallasi A. TRP channels as therapeutic targets. Curr Top Med Chem. 2013;13(3):241-3.

134. Voets T, Droogmans G, Wissenbach U, Janssens A, Flockerzi V, Nilius B. The principle of temperature-dependent gating in cold- and heat-sensitive TRP channels. Nature. 2004 Aug 12;430(7001):748-54.

135. Davis JB, Gray J, Gunthorpe MJ, Hatcher JP, Davey PT, Overend P, et al. Vanilloid receptor-1 is essential for inflammatory thermal hyperalgesia. Nature. 2000 May 11;405(6783):183-7.

136. Ehrlicher a, Betz T, Stuhrmann B, Koch D, Milner V, Raizen MG, et al. Guiding neuronal growth with light. Proc Natl Acad Sci U S A. 2002 12;99(25):16024-8.

137. Carnegie DJ, Stevenson DJ, Mazilu M, Gunn-Moore F, Dholakia K. Guided neuronal growth using optical line traps. Optics express. 2008 07;16(14):10507-17.

138. Stevenson DJ, Lake TK, Agate B, Dholakia K. Optically guided neuronal growth at near infra- red wavelengths. . 2006;14(21):2137-44.

139. Graves CE, McAllister RG, Rosoff WJ, Urbach JS. Optical neuronal guidance in three-dimensional matrices. J Neurosci Methods. 2009 05;179(2):278-83.

140. Zheng JQ. Turning of nerve growth cones induced by localized increases in intracellular calcium ions. Nature. 2000 01;403(6765):89-93.

141. Matthews BJ, Kim ME, Flanagan JJ, Hattori D, Clemens JC, Zipursky SL, et al. Dendrite self-avoidance is controlled by dscam. Cell. 2007 May 4;129(3):593-604.

142. Smith CJ, Watson JD, VanHovene MK, Colon-Ramos DA, Miller DM. Netrin (UNC-6) mediates dendritic self-avoidance. Nat Neurosci. 2012 May;15(5):731-7.

143. Fuerst PG, Koizumi A, Masland RH, Burgess RW. Self-avoidance mediated by DSCAM in the developing mammalian retina. Int J Dev Neurosci. 2008 Dec;26(8):832-.

144. Jhaveri S, Erzurumlu RS, Schneider GE. The optic tract in embryonic hamsters: Fasciculation, defasciculation, and other rearrangements of retinal axons. Visual Neurosci. 1996 Mar-Apr;13(2):359-74.

145. Favero CB, Henshaw RN, Grimsley-Myers CM, Shrestha A, Beier DR, Dwyer ND. Mutation of the BiP/GRP78 gene causes axon outgrowth and fasciculation defects in the thalamocortical connections of the mammalian forebrain. J Comp Neurol. 2013 Feb 15;521(3):677-96.

146. Baum PD, Garriga G. Neuronal migrations and axon fasciculation are disrupted in ina-1 integrin mutants. Neuron. 1997 Jul;19(1):51-62.

147. Minshew NJ, Williams DL. The new neurobiology of autism: Cortex, connectivity, and neuronal organization. Arch Neurol. 2007 Jul;64(7):945-50.

148. Choi YJ, Di Nardo A, Kramvis I, Meikle L, Kwiatkowski DJ, Sahin M, et al. Tuberous sclerosis complex proteins control axon formation. Genes Dev. 2008 Sep 15;22(18):2485-95.

149. Weiner JA, Koo SJ, Nicolas S, Fraboulet S, Pfaff SL, Pourquie O, et al. Axon fasciculation defects and retinal dysplasias in mice lacking the

immunoglobulin superfamily adhesion molecule BEN/ALCAM/SC1. Mol Cell Neurosci. 2004 Sep;27(1):59-69.

150. Hoffman-Kim D, Mitchel JA, Bellamkonda RV. Topography, cell response, and nerve regeneration. Annu Rev Biomed Eng. 2010;12:203-31.

151. Ming GL, Wong ST, Henley J, Yuan XB, Song HJ, Spitzer NC, et al. Adaptation in the chemotactic guidance of nerve growth cones. Nature. 2002 May 23;417(6887):411-8.

152. Wu T, Mohanty S, Gomez-Godinez V, Shi LZ, Liaw L, Miotke J, et al. Neuronal growth cones respond to laser-induced axonal damage. Journal of the Royal Society, Interface / the Royal Society. 2012 03;9(68):535-47.

153. Kim YT, Karthikeyan K, Chirvi S, Dave DP. Neuro-optical microfluidic platform to study injury and regeneration of single axons. Lab Chip. 2009 Sep 7;9(17):2576-81.

154. Gu L, Mohanty SK. Targeted microinjection into cells and retina using optoporation. J Biomed Opt. 2011 Dec;16(12).

155. Choudhury N, Zhang Z, Zhao F, Gu L, Mohanty S. Label-free optical detection of optogenetic activation of cells using phase-sensitive fourier domain optical coherence tomography. . 2012 2012-11-16;1(1):0.

156. Hayes P, Meadows HJ, Gunthorpe MJ, Harries MH, Duckworth DM, Cairns W, et al. Cloning and functional expression of a human orthologue of rat vanilloid receptor-1. Pain. 2000 11;88(2):205-15.

157. Clapham DE, Runnels LW, StrÃ¼bing C, Medical HH. The trp ion channel family. . 2001;2.

158. Benham CD, Gunthorpe MJ, Davis JB. TRPV channels as temperature sensors. . 2003;33:479-87.

159. Sharif-Naeini R, Ciura S, Bourque CW. TRPV1 gene required for thermosensory transduction and anticipatory secretion from vasopressin neurons during hyperthermia. Neuron. 2008 Apr 24;58(2):179-85.

Biographical Information

Bryan Black earned his B.S. in Physics from the University of North Carolina at Wilmington in the May of 2010. During his time at UNCW he was awarded merit scholarships, Dean's list honors all four semesters of residence, and the Marvin K. Moss award for studies in the field of science. Bryan graduated from UNCW in the spring of 2010, and was admitted to the department of physics at the University of Texas at Arlington in the fall of 2010. Bryan earned his Master of Science degree in Physics in the fall of 2012, and will complete his Ph D degree requirements in May, 2014. Following graduation, Bryan plans to work as a postdoctoral researcher in the field of biomedical optics, studying fundamental topics in neuroscience.